Search for the production of a single excited b quark in the Wt final state with a single lepton in pp collisions at $\sqrt{s} = 13\,\text{TeV}$ with the ATLAS detector

Dissertation

zur Erlangung des akademischen Grades
Doctor rerum naturalium
(Dr. rer. nat.)
im Fach Physik

eingereicht an der
Mathematisch-Naturwissenschaftlichen Fakultät
Institut für Physik
Humboldt-Universität zu Berlin

von
Herrn Dennis Sperlich

Präsident der Humboldt-Universität zu Berlin:
Prof. Dr.-Ing. Dr. Sabine Kunst

Dekan der Mathematisch-Naturwissenschaftlichen Fakultät:
Prof. Dr. Elmar Kulke

Tag der Disputation: 10.12.2020

Abstract

A search for an excited b quark, b^*, in events containing a top quark and a W boson is investigated. These b^* are predicted to have some anomalous couplings to Standard Model bosons aiding the production in high energy proton-proton collisions. The search is aiming for events, where one of the two W bosons decays into an electron or muon, while the other decays hadronically. With only one neutrino, the event can be kinematically fully reconstructed. This enables the use of the mass of the b^* as the discriminant variable.

The data source under investigation is the data taken by the ATLAS detector at the LHC accelerator in the years 2015 and 2016 at a center-of-mass energy of $\sqrt{s} = 13\,\text{TeV}$. The combined dataset corresponds to an integrated luminosity of $\mathcal{L}_{int} = 36.1\,\text{fb}^{-1}$. The analysis targets high mass excited b^* quarks, where the products of the hadronically decaying W are contained within a large-radius jet.

No significant excess over the expected background is observed and upper limits on the cross-section times branching ratio and coupling limits are derived. Assuming unit coupling, b^* decaying into Wt are excluded up to $m_{b^*,\text{obs}} = 2.5\,\text{TeV}$, with an expected exclusion limit of $m_{b^*,\text{exp}} = 2.4\,\text{TeV}$.

Zusammenfassung

In dieser Dissertation wird eine Suche nach einem angeregten b Quark, b^*, durchgeführt. Für diese b^* wird eine anomale Kopplung an Bosonen aus dem Standard Modell vorhergesagt. Diese Kopplung führt zu der Produktion in hochenergetischen Proton-Proton Kollisionen. In der Suche zielen wir auf Ereignisse, bei denen eines der zwei W Bosonen in ein Elektron oder Muon zerfällt und das andere in ein Hadronenpaar. Da es nur ein Neutrino in diesem Prozess gibt, kann das ganze Ereigniss kinematisch rekonstruiert werden. Damit ist es möglich, die Masse des b^* als diskriminierende Variable zu verwenden.

Als Datenquelle dienen die Daten, die der ATLAS Detektor in den Jahren 2015 und 2016 bei Proton-Proton Kollisionen mit einer Schwerpunksenergie von $\sqrt{s} = 13\,\text{TeV}$ aufgezeichnet hat. Dabei entspricht diese Datenmenge einer integrierten Luminosität von $\mathcal{L}_{int} = 36.1\,\text{fb}^{-1}$. Da die Analyse auf hochmassige b^* abziehlt, kann man davon ausgehen, dass das Hadronenpaar aus dem W Zerfall in einen Jet mit großen Radius passt.

Es wurde kein signifikanter Überschuss über den Untergrund gefunden. Damit können nur obere Ausschlussgrenzen bezüglich der Wirkungsquerschnitte in dem entsprechenden Zerfallskanal abgeleitet werden. Unter Annahme von einer Kopplungskonstanten von 1, sind Zerfälle von $b^* \to Wt$ bis zu einer Masse $m_{b^*,\text{obs}} = 2.5\,\text{TeV}$ ausgeschlossen, wobei erwartet wurde, dass die Ausschlussmasse bei $m_{b^*,\text{exp}} = 2.4\,\text{TeV}$ liegen würde.

Contents

Chapter 1

Introduction

The Large Hadron Collider (LHC) is designed to be a discovery machine. Since it's start in 2009, physicists use the experiments at LHC to collect data to search for new phenomena. So far the major discovery of the LHC, was the Higgs boson in 2012 [27, 55], which was predicted in the Standard Model. In addition to the discovery of the Higgs boson, many measurements on Standard Model processes are done, validating precision predictions of the Standard Model. In these measurements no significant deviation from the Standard Model could be found. In conjunction with these precision measurements, direct searches for new phenomena were and are executed in many directions of new theory models. This is an interesting process, as even though the Standard Model is confirmed in so many ways now, there are still some open questions. For example, we don't understand why the Higgs boson mass of about 125 GeV [20] is so much lower than the Planck mass, a problem known as naturalness or hierarchy problem. These questions are addressed by various theories proposing models beyond the Standard Model, which predict new phenomena at the TeV scale. Many of these models contain new particles, some of which are at the TeV mass scale. They can also introduce new couplings to known bosons and fermions.

This thesis investigates a model where the quarks are predicted to be composite particles. If they are, they would have excited states, which would decay into Standard Model quarks. The particle of interest for this thesis is an excited quark with a charge of $\pm\frac{1}{3}$, so like an excited b quark. With a new anomalous coupling to Standard Model bosons, like the gluon or W, it could be efficiently produced in proton-proton collisions. As it is suspected to be at the TeV scale, it could decay into Wt, where the t would successively decay into Wb. With these two W bosons, we can build an analysis which requires exactly one of them to decay into a lepton (electron or muon) and the other into quarks. If the excited b quark is very heavy, the two W bosons and the b quark have transverse momenta high enough, that the decay products of each W are very close to each other. In this case, the hadronically decaying W

can end up in a single large-radius jet. The neutrino, from the leptonically decaying W, is the only neutrino in the event, and thus the full kinematics can be reconstructed. With the full kinematics at hand, the mass of the excited b quark can be reconstructed as well.

The search for this excited quark is performed on the proton-proton collision data recorded with ATLAS in 2015 and 2016, where the center-of-mass energy was $\sqrt{s} = 13\,\text{TeV}$ and an integrated luminosity[1] of $\mathcal{L}_{int} = 36.1\,\text{fb}^{-1}$ was recorded. Similar searches where already done on $\sqrt{s} = 8\,\text{TeV}$ data at ATLAS [29] and CMS [65].

1.1 Work on upgrade of the ATLAS inner detector

In addition to the search outlined above, I worked on research and development for the ITk Strip [40] detector, which replaces the current inner tracking detector in the long shutdown 3 of the LHC. In this process, I was involved in the prototyping of modules for this dectector using three different generations of readout architectures. This involvement got me to the point, where I'm now the designer of the powerboards for the end-cap modules.

My work on the upgrade prototypes also resulted in several publications, like on the test results of different prototype stages [46, 50, 85, 68, 69, 60] as well as testbeam results of sensor properties and module performance [86, 51, 80, 79, 78, 77]. But due to time constraints, this thesis does not contain a coherent description of the upgrade related work.

[1] Luminosity is the ratio of interaction rate and the interaction cross section of this process σ: $\mathcal{L} = \frac{1}{\sigma}\frac{\mathrm{d}N}{\mathrm{d}t}$. Usually the luminosity will be used in this thesis in the integrated form $\mathcal{L}_{int} = \int \mathcal{L}\mathrm{d}t$. This is usefull, as this describes the expected number of interactions of a process with a given cross section.

Chapter 2

ATLAS Detector

2.1 LHC and ATLAS

The ATLAS detector[24] is one of several measurement instruments installed at the Large Hadron Collider (LHC)[58]. The LHC is currently the largest and most powerful particle accelerator on earth. It is located at the European Organization for Nuclear Research (french: Conseil Européen pour la Recherche Nucléaire, CERN) at the border between France and Switzerland, in a tunnel about 100 m below surface and has a circumference of about 27 km. The LHC accelerates two proton beams in opposite directions to up to 6.5 TeV each. They are collided in four points, where the experiments ATLAS, ALICE, CMS and LHCb are located. To bend the proton beam around the ring, 1232 main dipole magnets are used in conjunction with 392 focusing quadrupole magnets as well as several sextupole and octupole magnets for further beam corrections. The acceleration is done in 16 RF cavities.

The proton beam is not generated within LHC itself but rather pre-accelerated protons with 450 GeV proton energy are injected into the LHC. These protons are provided by a chain of accelerators at CERN:

1. Linear Accelerator 2 (LINAC2, 50 MeV proton energy)
2. Proton Synchrotron Booster (PSB, 1.4 GeV proton energy)
3. Proton Synchrotron (PS, 25 GeV proton energy)
4. Super Proton Synchrotron (SPS, 450 GeV proton energy)

2.1.1 The ATLAS detector

The center of the ATLAS detector, shown in figure 2.2, is located at one of the four collision points of LHC in which two proton beams are brought into

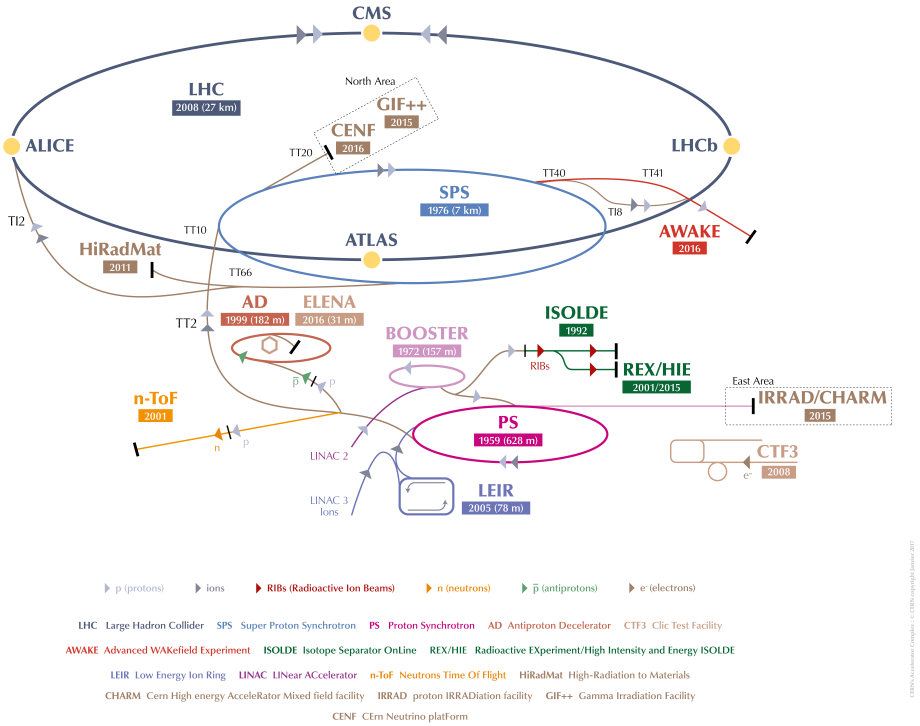

Figure 2.1: CERN accelerator complex including LHC and the necessary pre-accelerator chain: LINAC2, PSB, PS, SPS. The image also shows the ATLAS experiment, as well as the other experiments at CERN utilizing the same accelerator infrastructure.[73]

collision. Sometimes these collisions of protons with center-of-mass energies of 13 TeV produce new particles. These or their decay products can be detected with the ATLAS detector to analyze the fundamental interaction between the particles. To detect and identify different particles, the detector is built in layers with different functions around the interaction point. The inner detector is a tracking detector[1], measuring three-dimensional trajectories[2] of charged particles in a magnetic field. Around the tracking detector are calorimeters[3]

[1]A tracker in the context of this thesis is a detector or multiple detectors which are used to obtain spacepoints of the flight path of charged particles. They are usually in a magnetic field, so that the track of spacepoints follows a curve which can be used to measure the momentum component perpendicular to the magnetic field.

[2]We usually use two coordinate systems, either cylindrical or spherical. For both, the origin is in the interaction point. In the cylindrical coordinate system, the beam direction corresponds to the z axis. The direction perpendicular to the beam is then the r coordinate and ϕ the angle around the beam axis. In the spherical case, the ϕ angle stays the same and the second angle θ is towards the beam axis.

[3]A calorimeter in the context of this thesis is a detector or multiple detecotrs which are used to measure the energy of a particle or a collection of particles close by. This is done by stopping the particles and measureing the absorbed energy.

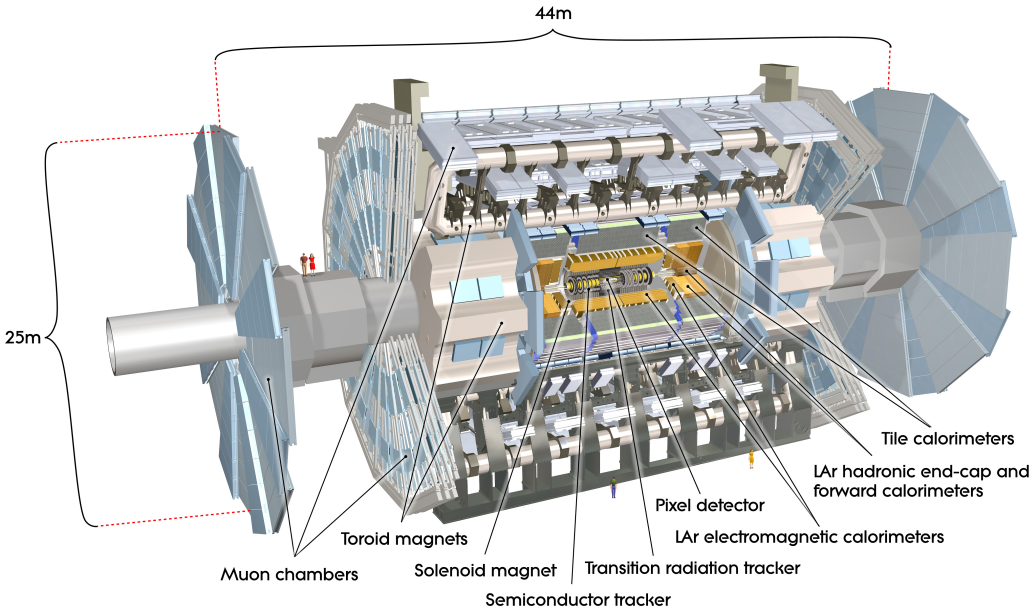

Figure 2.2: 3D rendering of the ATLAS detector, cut open to allow view of the internal layers.[24]

to stop electromagnetically and hadronically interacting particles and measure their energy. Due to the high amount of material in the calorimeters, only neutrinos and muons are able to penetrate and reach the muon tracking detector in a second magnetic field. As neutrinos are not electrically charged, they are not detected by this tracker.

2.1.1.1 Inner detector

In figure 2.3, the three main components of the inner detector are shown. The most central part, between radii of 33.25 mm and 122.5 mm, is a pixel detector with four layers. The most inner layer is the Insertable B Layer (IBL) with 50 µm × 250 µm pixel size. The three other pixel layers are made from pixels with 50 µm × 400 µm size.[81, 23]

Outside of the pixel layers, between radii 299 mm and 514 mm, is the SemiConductor Tracker (SCT), which is made from silicon strip modules, made from four sensors each. The sensors are pairwise wirebonded together to get an effective strip length of 12 cm at 80 µm pitch. These pairs of sensors are glued back-to-back with a stereo angle of 40 mrad. At some locations in the end cap, only two back-to-back sensors create a module.[89, 31]

At radii between 554 mm and 1082 mm from the beam, a Transition Radiation Tracker (TRT) is installed. This is a gaseous straw detector, 7 m

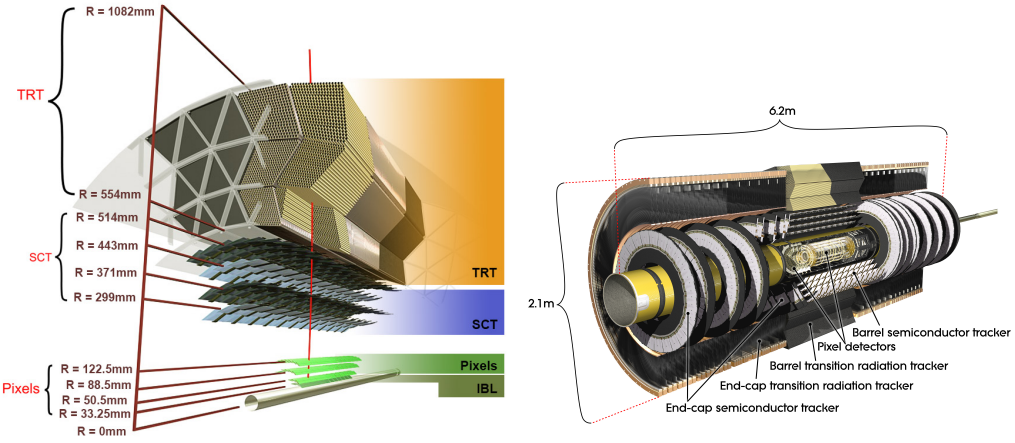

(a) (b)

Figure 2.3: (a) 3D rendering of a radial view on the ATLAS inner detector barrel in [81] and (b) a cut open view of the full inner detector in [23]

long with a 1.44 m long barrel. The straws are 4.4 mm in diameter and placed parallel to the beam pipe in the barrel and perpendicular to the beam pipe in the end caps. The transition radiation is produced by a polypropylene-polyethylene fiber mat with a density of $0.06\,\mathrm{g/cm^3}$ filling the space between the straws in the barrel. In the end cap, the radiators are stacks of 15 µm polypropylene film spaced by a polyamide fabric. The stacks are between 6 and 37 layers thick and are placed between each layer of straws. A mixture with 70% Xe, 27% CO_2, 3% O_2 or 70% Ar, 30% CO_2 is used as active gas. The Ar based mixture is used in areas which have higher leak rates. Charged particles are expected to hit between 20 and 36 straws and are reconstructed with 30 µm − 50 µm resolution in the pseudorapidity range up to $|\eta| < 2^4$. [91, 90, 92, 71]

The whole inner detector is immersed in a 2 T axial magnetic field produced by a superconducting solenoid magnet. Combining all 3 components of the inner detector, charged particle transverse momentum measurements are performed with a precision of $\frac{\sigma_{p_T}}{p_T} \sim 0.5\% p_T \oplus 1\%$. Vertex reconstruction is possible in pseudorapidity range up to $|\eta| < 2.5$.

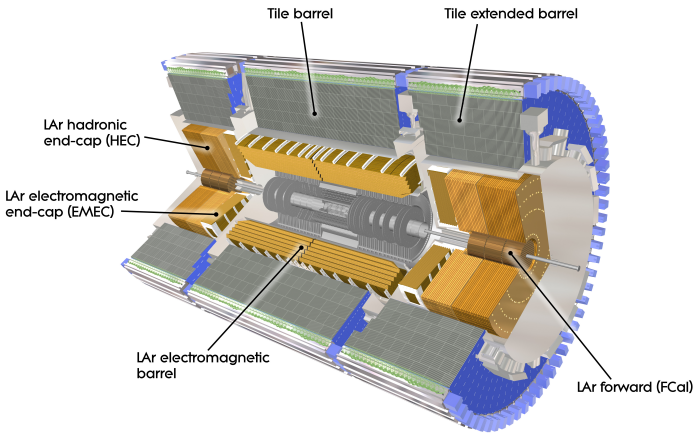

(a)

Figure 2.4: 3D rendering of a cut open view of the full calorimeter system [25]

2.1.1.2 Calorimeter

In figure 2.4, the calorimeter system of the ATLAS detector is shown. A cryostat is necessary in the inner part. It houses the superconducting solenoid magnet for the inner detector and a liquid-argon based calorimeter. The outer part is a steel / plastic scintillator based calorimeter.

The first part of the calorimeter system is the pre-sampler. It is just outside of the solenoid magnet. The pre-sampler uses 11 mm active thickness of liquid-argon, which measures the pre-shower before the calorimeter, created by the material of the inner detector, the cryostat walls and the solenoid magnet. [37]

Around the pre-sampler and up to $|\eta| < 1.3$ is the barrel electromagnetic calorimeter. It is a lead – liquid-argon sampling calorimeter with accordeon-shaped absorbers and electrodes. The calorimeter has a radiation length between 22 and $33\,X_0$[5]. $1.5\,X_0$ are already in front of the calorimeter due to the tracker and services. 32 modules, with 3424 readout cells each, are building the barrel electromagnetic calorimeter and result in a granularity of

[4]Pseudorapidity η is defined as $\eta = -\ln\left(\tan\frac{\theta}{2}\right)$ where θ is the polar angle measured from the beam axis. It is derived from the rapidity $y = \ln\left(\frac{E+p_z c}{E-p_z c}\right)$ which is invariant under boosts parrallel to the z axis. For $p_z c \gg mc^2$ rapidity and pseudorapidity are very similar $y \simeq \eta$, but pseudorapidity is simpler to calculate from Detector measurements.

[5]X_0 is the radiation length and a characteristic number of materials. It describes the energy loss of particles flying through and electromagnetically interacting with it. High energy electrons reduce their energy to $\frac{1}{e}$ for each X_0 they pass through. It is also the length scale at which electromagnetic cascades are produced.

$|\Delta\eta|= 0.025, |\Delta\phi|= \frac{2\pi}{64}$ and three segments along the path of particles from the interaction point. The design dynamic range is 30 MeV to 3 TeV [96]. The absorber plates are made of 1.13 mm and 1.53 mm lead, cladded with epoxy impregnated fiberglass mats and stainless steel plates. In between are electrodes made out of three layers of patterned copper separated by polyimide. The outer two copper layers are at high voltage where as the inner layer is capacitively coupled to the outer layers and used to read out the signal. Honeycomb spacers are used in the accordeon structure to allow liquid-argon in between the lead layers with the electrodes centered in the gap. [64]

To extend the coverage of electromagnetic calorimetry to the more forward region, the ElectroMagnetic End-cap Calorimeter (EMEC) is used. It extends between $1.375 < |\eta| < 3.2$, The barrel cryostat wall and inner detector services sit in the region $1.5 < |\eta| < 1.8$ and limit the calorimeter efficiency in this region. This is somewhat mitigated by a pre-sampler, similar to the barrel pre-sampler. The η granularity ranges between $\frac{0.025}{8}$ and 0.1 and the ϕ granularity between $\frac{2\pi}{256}$ and $\frac{2\pi}{64}$. The fundamental design is similar to the barrel. It also uses a lead absorber in stainless steel and fiberglass laminate in an accordeon structure. But in contrast to the barrel calorimeter, the drift gap of liquid-argon is a function of radius and varies between 0.9 mm to 3.1 mm due to the different orientation.[64]

Outside of the EMEC is the Hadronic End-cap Calorimeter (HEC). With its coverage of $1.5 < |\eta| < 3.2$, all jets[6] reaching the HEC have to pass through EMEC before. In order to contain jets from up to 14 TeV collisions, $12\,\lambda$[7] nuclear interaction lengths are required and EMEC has already about two. HEC utilizes copper as absorbing material and an 8.5 mm argon gap separated into four segments with four independent high-voltage feeds for reliability. The readout is only at the inner electrode of each gap and capacitively coupled and segmented. The design energy resolution is $\frac{\sigma(E)}{E} = \frac{50\%}{\sqrt{E[\mathrm{GeV}]}} \oplus 3\%$ with a segmentation of $|\Delta\eta| \times |\Delta\phi| = 0.1 \times \frac{2\pi}{64}$ for $|\eta| < 2.5$ and $0.2 \times \frac{2\pi}{32}$ for larger pseudorapidities. Along the path of the showers, the calorimeter is providing four segments. In contrast to the other liquid-argon calorimeters, the pre-amplification and summation happens in the cold volume using GaAs pre-amplifiers. The HEC is able to detect muons and measure their radiative energy loss.[61]

Inside the HEC is the forward calorimeter (FCal). It is a liquid-argon sampling calorimeter made from electrode tubes and rods with a 0.269 mm to

[6] A jet is a collection of particles or energy deposits in a detector which are close together. They usually contain the collection of hadronization and decay products of quarks or gluons, as well as showering products from interaction with material of these products.

[7] λ is the nuclear interaction length, which is the mean distance between inelastic nuclear interactions.

0.508 mm liquid-argon gap in between. They are made out of copper (inner module) or a tungsten alloy (outer two modules) in a hexagonal pattern. The coverage is $3.1 < |\eta| < 4.9$ and the segmentation is $|\Delta\eta| \times |\Delta\phi| = 0.1 \times 0.1$ close to the interaction point and $|\Delta\eta| \times |\Delta\phi| = 0.2 \times 0.2$ at the outer layers. Jet Energy resolution is $\frac{\Delta E_T}{E_T} < 10\%$ for $E_T > 25\,\text{GeV}$, which requires $\frac{\Delta E}{E} < 7\%$ for the calorimeter cells. An angular resolution for jets of $\frac{\Delta\theta}{\theta} < 7\%$ for energies above 250 GeV is required. The dynamic range is from electronic noise up to 7 TeV. Due to its location in the high η region, roughly 7 TeV of energy are deposited every bunch crossing in each of the two FCal at design luminosity of $\mathcal{L} = 1 \times 10^{34}\,\text{cm}^{-2}\text{s}^{-1}$. Both FCal detectors are split up into three modules. The first module has an electromagnetic radiation length of $28\,X_0$ and a nuclear interaction length of $2.7\,\lambda$. The other two modules have $3.7\,\lambda$ and $3.6\,\lambda$ respectively, resulting in $10\,\lambda$ for the FCal. Behind the FCal is additional brass shielding for the muon system. [38]

Outside of the cryostat is the Tile Calorimeter. It is behind the electromagnetic calorimeters which already contributes about two nuclear interaction lengths. It is built as a sampling calorimeter using plastic scintillators in low-carbon steel absorbers and covers $|\eta| < 1.7$. It is divided into the long barrel ($|\eta| < 1$) and two extended barrels ($0.8 < |\eta| < 1.8$). The segmentation is in 64 wedge-shaped modules placed in ϕ around the detector. This results in a granularity of $|\Delta\phi| \sim 0.1$. The mdoules are segmented into three layers along the shower direction with nuclear interaction lengths of 1.5, 4.1 and $1.8\,\lambda$ for the barrel and 1.5, 2.6 and $3.3\,\lambda$ for the extended barrel respectively. For the first two layers, the $|\Delta\eta|$ segmentation is 0.1 and for the third layer 0.2. Each of these so divided cells is connected via wavelength shifting fibers to two photomultiplier tubes and thus two readout channels. The design energy resolution is $\frac{\sigma(E)}{E} = \frac{50\%}{\sqrt{E[\text{GeV}]}}$ with a desired energy scale uncertainty of 3% and a linearity of 2% up to 4 TeV. For good E_T^{miss} measurement, high hermiticity and small dead fraction are required.[25]

2.1.1.3 Muon system

Outside of the calorimeters is the muon system. Due to the high mass and hermiticity of the other detectors, the only electrically charged particles that are able to completely traverse the calorimters are muons. They are detected in gas based detectors, which are located in a magnetic field created by a big superconducting toroid magnet in the barrel and two smaller toroid magnets in the end-caps. The high magnetic field combined with the large size results in a bending power between 3 Tm and 6 Tm.

To cover the pseudorapidity range up to $|\eta| < 2.6$ most efficiently, the detector is divided into barrel chambers, which are rectangular and arranged cylindrically around the beam pipe, and two trapezoidal end-caps orthogonal

to the beam pipe.

Four chamber technologies are employed: Monitored Drift Tube (MDT), Cathode Strip Chambers (CSC), Resistive Plate Chambers (RPC) and Thin Gap (multi-wire proportional) Chambers (TGC). MDT and CSC are used for precision measurements, where as RPCs are used in the barrel trigger system and TGC in the end cap trigger system. [97, 47]

Monitored Drift Tubes: The ATLAS muon system contains 1150 MDT chambers with 354 384 tubes distributed between barrel and end-cap. The aluminium tubes are 29.97 mm in diameter with a gold plated tungsten – rhenium 50 µm wire in the center and an argon – CO_2 (93% : 7%) gas mixture [97]. With a maximal tube length of 3.8 m, an optical deformation monitoring system needs to be used. The chambers provide track position resolution of 40 µm [47].

Cathode Strip Chambers: The second precision tracking system in the ATLAS muon system are Cathode Strip Chambers. They are used in the forward region $2.0 < |\eta| < 2.7$. There are two different sizes of chambers in use. Together they provide the inner most layer in each end cap. Depending on the chamber size, the wire spacing is 5.567 mm or 5.308 mm in η and 12.922 mm or 21.004 mm in ϕ respectively. This wire density is higher than in the MDT, which allows for higher track densities. An argon – CO_2 (80% : 20%) mixture is used as detection medium. [97]

Resistive Plate Chambers: In order to trigger on muons, three layers of resistive plate chambers are used in the barrel part ($|\eta| < 1.0$) of the muon system. This detector uses resistive plates made out of 1.8 mm thick plastic laminates with 2 mm of active gas in between. The gas mixture is $C_2H_2F_2/i-C_4H_{10}/SF_6$ (94.7% : 5% : 0.3%). [97]

Thin Gap Chambers: The second trigger system for muons are thin gap chambers in the end cap. They are made in trapezoidal shape with typical dimensions of 1.3 m (long base) × 1.3 m (height). The active volume contains a CO_2 - $n-pentane$ (55% : 45%) gas with 50 µm diameter wires at 2900 V between two 1.6 mm FR4 plates. The gas facing side of the FR4 plates is graphite coated, while the outside has copper strips perpendicular to the wires. The wires inside the gas are spaced with 1.8 mm pitch and have 1.4 mm distance to each FR4 side. All the wires and the perpendicular strips are connected to amplifier-shaper-discriminator readout channels [88].

Chapter 3

Theoretical Fundamentals

3.1 Standard Model

In particle physics, there is an established model, the Standard Model, describing three of the four known fundamental forces: electromagnetic, weak and strong force together with the fundamental particles. The classification of these particles is done by their coupling to the three forces.

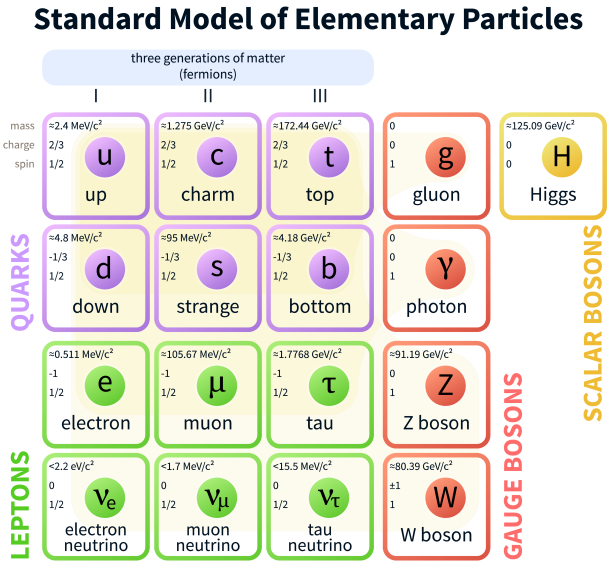

Figure 3.1: Particles of the Standard Model.[72]

In figure 3.1, the particles in the Standard Model are shown. Quarks and leptons, in the first three columns, form the group called fermions, because these have a spin $\frac{1}{2}$. The other group of particles are the bosons, which have a spin of 0 or 1. The vector bosons photon, W, Z and gluon have spin 1 and are the carrier of the three forces: the photon of the electromagnetic force,

W and Z of the weak force and the gluon of the strong force. The W boson also has an electric charge and thus couples electromagnetically as well as under the weak force. The gluon interacts under the strong force. The photon and gluon are massless, whereas the W and Z have a mass of 80.39 GeV and 91.19 GeV respectively. The fifth boson is the higgs particle, has spin 0 and couples to the masses of the quarks, charged leptons and W and Z boson.

Starting from the top left are the quarks, named: down, up, strange, charm, bottom and top. Their characterizing property is the interaction under the strong force due to their color charge. They also interact under the weak and electromagnetic force with an electric charge of either $\pm 2/3\,\mathrm{e}$ (up, charm and top) or $\mp 1/3\,\mathrm{e}$ (down, strange, bottom). The lower charge sign corresponds to their anti-particle. The mass of all six quarks ranges from 2.4 MeV (up quark) to 172.44 GeV (top).

The next row of three particles are the electrically charged leptons: electron, muon and tau. They do not interact under the strong interaction but under the weak and electromagnetic interaction. The electric charges are $\pm 1\,\mathrm{e}$ and the masses are also different and range from 511 keV (electron) to 1.7786 GeV (tau). As with the quarks, the mass is used to sort the particles in the figure.

The bottom row of three particles are the electrically neutral leptons, called neutrinos. They do not interact under the strong or electromagnetic force and thus only interact under the weak force. Due to their association to a charged lepton in weak interactions, they are named electron neutrino, muon neutrino and tau neutrino. Due to the small neutrino massess and weak interaction compared to the other particles, the exact masses are not yet measured and only upper limits can be quoted.

In addition to these 12 particles, there are also the anti-particle versions of all particles. Their only difference is the inversion of all charges: electric, color and weak charge.

3.1.1 Mathematical description

The Standard Model is, mathematically formulated, a quantum field theory. It has internal symmetries of the unitary group $SU(3)_C \times SU(2)_L \times U(1)_Y$ and is renormalizable and mathematically self-consistent.

The whole Standard Model can be expressed in a single Lagrangian 3.1. Due to its length, it is shown split up in functional parts. This section follows the Appendix on the Standard Model in [95].

$$\mathcal{L}_{\text{total}} = \mathcal{L}_c + \mathcal{L}_w + \mathcal{L}_f + \mathcal{L}_{fH} + \mathcal{L}_{fc} + \mathcal{L}_{FPc} + \mathcal{L}_{FPw} \tag{3.1}$$

The different parts of the full Lagrangian are:

- $\mathcal{L}_c$: color part, describing the strong interactions
- $\mathcal{L}_w$: weak part, describing the weak interactions
- $\mathcal{L}_f$: fermion part, describing the interaction of the fermions with the weak force
- $\mathcal{L}_{fH}$: fermion-higgs part, describing the interactions of fermions with the higgs system
- $\mathcal{L}_{fc}$: fermion-color part, describing the interaction of fermions with the strong force
- $\mathcal{L}_{FPc}$: Faddeev-Popov ghost color part, describing the necessary ghost interactions in the strong force
- $\mathcal{L}_{FPw}$: Faddeev-Popov ghost weak part, describing the necessary ghost interaction in the weak force

Strong interactions The strong interaction of gluons with gluons is described by the Lagrangian:

$$\mathcal{L}_c = -\frac{1}{2}\partial_\nu g^a_\mu \partial_\nu g^a_\mu - g_s f^{abc}\partial_\mu g^a_\nu g^b_\mu g^c_\nu - \frac{1}{4}g_s^2 f^{abc} f^{ade} g^b_\mu g^c_\nu g^d_\mu g^e_\nu \tag{3.2}$$

The indices a, b, c, d, e take all values 1..8 and correspond to the eight gluons g^a_μ. ∂_ν is the partial derivative with respect to the ν component of the 4-vector $\partial_\nu = \frac{\partial}{\partial x^\nu}$. g_s is the strong coupling constant and f^{abc} are the structure constants, anti-symmetric in all three indices.

Weak interactions The weak interactions of the $W^\pm, Z^0$ and H bosons interacting with each other are described in the Lagrangian:

$$\begin{aligned}
\mathcal{L}_w = &- \partial_\nu W^+_\mu \partial_\nu W^-_\mu - M^2 W^+_\mu W^-_\mu && (3.3)\\
&- \frac{1}{2}\partial_\nu Z^0_\mu \partial_\nu Z^0_\mu - \frac{1}{2c_w^2} M^2 Z^0_\mu Z^0_\mu && (3.4)\\
&- \frac{1}{2}\partial_\mu A_\nu \partial_\mu A_\nu && (3.5)\\
&- \frac{1}{2}\partial_\mu H \partial_\mu H - \frac{1}{2}m_h^2 H^2 && (3.6)\\
&- \partial_\mu \phi^+ \partial_\mu \phi^- - \frac{1}{2}\partial_\mu \phi^0 \partial_\mu \phi^0 - \frac{1}{2c_w^2} M \phi^0 \phi^0 && (3.7)\\
&- \beta_h \left[\frac{2M^2}{g^2} + \frac{2M}{g}H + \frac{1}{2}(H^2 + \phi^0\phi^0 + 2\phi^+\phi^-)\right] + \frac{2M^4}{g^2}\alpha_h && (3.8)\\
&- igc_w[\partial_\nu Z^0_\mu (W^+_\mu W^-_\nu - W^+_\nu W^-_\mu) - Z^0_\nu (W^+_\mu \partial_\nu W^-_\mu - W^-_\mu \partial_\nu W^+_\mu)
\end{aligned}$$

$$+ Z^0_\mu(W^+_\nu \partial_\nu W^-_\mu - W^-_\nu \partial_\nu W^+_\mu)] \tag{3.9}$$

$$- igs_w[\partial_\nu A_\mu(W^+_\mu W^-_\nu - W^+_\nu W^-_\mu) - A_\nu(W^+_\mu \partial_\nu W^-_\mu - W^-_\mu \partial_\nu W^+_\mu)$$
$$+ A_\mu(W^+_\nu \partial_\nu W^-_\mu - W^-_\nu \partial_\nu W^+_\mu)] \tag{3.10}$$

$$- \frac{1}{2}g^2 W^+_\mu W^-_\mu W^+_\nu W^-_\nu + \frac{1}{2}g^2 W^+_\mu W^-_\nu W^+_\mu W^-_\nu \tag{3.11}$$

$$+ g^2 c^2_w(Z^0_\mu W^+_\mu Z^0_\nu W^-_\nu - Z^0_\mu Z^0_\mu W^+_\nu W^-_\nu) \tag{3.12}$$

$$+ g^2 s^2_w(A_\mu W^+_\mu A_\nu W^-_\nu - A_\mu A_\mu W^+_\nu W^-_\nu) \tag{3.13}$$

$$+ g^2 s_w c_w[A_\mu Z^0_\nu(W^+_\mu W^-_\nu + W^+_\nu W^-_\mu) - 2A_\mu Z^0_\mu W^+_\nu W^-_\nu] \tag{3.14}$$

$$- g\alpha_h M[H^3 + H\phi^0\phi^0 + 2H\phi^+\phi^-] \tag{3.15}$$

$$- \frac{1}{8}g^2\alpha_h[H^4 + (\phi^0)^4 + 4(\phi^+\phi^-)^2 + 4(\phi^0)^2\phi^+\phi^-$$
$$+ 4h^2\phi^+\phi^- + 2(\phi^0)^2 H^2] \tag{3.16}$$

$$- gMW^+_\mu W^-_\mu H - \frac{1}{2}g\frac{M}{c^2_w}Z^0_\mu Z^0_\mu H \tag{3.17}$$

$$- \frac{1}{2}ig[W^+_\mu(\phi^0\partial_\mu\phi^- - \phi^-\partial_\mu\phi^0) - W^-_\mu(\phi^0\partial_\mu\phi^+ - \phi^+\partial_\mu\phi^0)] \tag{3.18}$$

$$+ \frac{1}{2}g[W^+_\mu(H\partial_\mu\phi^- - \phi^-\partial_\mu H) + W^-_\mu(H\partial_\mu\phi^+ - \phi^+\partial_\mu H)] \tag{3.19}$$

$$+ \frac{1}{2}g\frac{1}{c_w}Z_\mu(H\partial_\mu\phi^+ - \phi^0\partial_\mu H) \tag{3.20}$$

$$- ig\frac{s^2_w}{c_w}MZ^0_\mu(W^+_\mu\phi^- - W^-_\mu\phi^+) + igs_w MA_\mu(W^+_\mu\phi^- - W^-_\mu\phi^+) \tag{3.21}$$

$$- ig\frac{1-2c^2_w}{2c_w}Z^0_\mu(\phi^+\partial_\mu\phi^- - \phi^-\partial_\mu\phi^+) + igs_w A_\mu(\phi^+\partial_\mu\phi^- - \phi^-\partial_\mu\phi^+) \tag{3.22}$$

$$- \frac{1}{4}g^2 W^+_\mu W^-_\mu[H^2 + (\phi^0)^2 + 2\phi^+\phi^-] \tag{3.23}$$

$$- \frac{1}{8}g^2\frac{1}{c^2_w}Z^0_\mu Z^0_\mu[H^2(\phi^0)^2 + 2(2s^2_w - 1)^2\phi^+\phi^-] \tag{3.24}$$

$$- \frac{1}{2}g^2\frac{s^2_w}{c_w}Z^0_\mu\phi^0(W^+_\mu\phi^- + W^-_\mu\phi^+) - \frac{1}{2}ig^2\frac{s^2_w}{c_w}Z^0_\mu H(W^+_\mu\phi^- - W^-_\mu\phi^+) \tag{3.25}$$

$$+ \frac{1}{2}g^2 s_w A_\mu\phi^0(W^+_\mu\phi^- + W^-_\mu\phi^+) \tag{3.26}$$

$$+ \frac{1}{2}ig^2 s_w A_\mu H(W^+_\mu\phi^- - W^-_\mu\phi^+) \tag{3.27}$$

$$- g^2\frac{s_w}{c_w}(2c^2_w - 1)Z^0_\mu A_\mu\phi^+\phi^- - g^2 s^2_w A_\mu A_\mu\phi^+\phi^- \tag{3.28}$$

Given that this Lagrangian is somewhat long, let's go through it line by line. The first four lines 3.3-3.6 describe the kinetic and mass term of the

$W^\pm, Z^0$ and H boson, as well as the massless kinetic term of the photon A. Line 3.7 has the kinetic term of the charged and neutral higgs ghost ϕ^+, ϕ^-, ϕ^0, as well as the mass term of the neutral higgs ghost. Going on with higgs self couplings, line 3.8 has the tadpole term of the higgs with it's tadpole constant β_h, which needs to be 0 in lowest order. $\alpha_h = \frac{m_h^2}{4M^2}$ is the higgs scattering parameter.

Starting with line 3.9, the interactions of vector bosons are described. Line 3.9 is the scattering of a $W^\pm$ on a Z^0 and line 3.10 is the scattering of a $W^\pm$ on a photon. Four-point vertices with four $W^\pm$, two Z^0 and two $W^\pm$, two photons A and two $W^\pm$ as well as a photon A, a Z^0 and two $W^\pm$ are described in lines 3.11 - 3.14.

The remaining lines are the coupling of $W^\pm, Z^0$ and the photon A to both the physical higgs H as well as the ghost higgs $\phi^\pm, \phi^0$ in three- and four-point vertices. It should be noted however, that the photon is only allowed in vertices where either two $W^\pm$ or two of the charged higgs ghosts $\phi^\pm$ appear.

Fermions The Lagrangian for the fermions is:

$$\mathcal{L}_f = -\bar{e}^\lambda(\gamma\partial + m_e^\lambda)e^\lambda - \bar{\nu}^\lambda\gamma\partial\nu^\lambda - \bar{u}_j^\lambda(\gamma\partial + m_u^\lambda)u_j^\lambda - \bar{d}_j^\lambda(\gamma\partial + m_d^\lambda)d_j^\lambda \tag{3.29}$$

$$+ igs_w A_\mu[-(\bar{e}^\lambda\gamma^\mu e^\lambda) + \frac{2}{3}(\bar{u}_j^\lambda\gamma^\mu u_j^\lambda) - \frac{1}{3}(\bar{d}_j^\lambda\gamma^\mu d_j^\lambda)] \tag{3.30}$$

$$+ \frac{ig}{4c_w}Z_\mu^0[(\bar{\nu}^\lambda\gamma^\mu(1+\gamma^5)\nu^\lambda) + (\bar{e}^\lambda\gamma^\mu(4s_w^2 - 1 - \gamma^5)e^\lambda) + (\bar{d}_j^\lambda\gamma^\mu(\frac{4}{3}s_w^2 - 1 - \gamma^5)d_j^\lambda) + (\bar{u}_j^\lambda\gamma^\mu(1 - \frac{8}{3}s_w^2 + \gamma^5)u_j^\lambda)] \tag{3.31}$$

$$+ \frac{ig}{2\sqrt{2}}W_\mu^+[(\bar{\nu}^\lambda\gamma^\mu(1+\gamma^5)e^\lambda) + (\bar{u}_j^\lambda\gamma^\mu(1+\gamma^5)C_{\lambda\kappa}d_j^\kappa)] \tag{3.32}$$

$$+ \frac{ig}{2\sqrt{2}}W_\mu^-[(\bar{e}\lambda\gamma^\mu(1+\gamma^5)\nu^\lambda) + (\bar{d}_j^\kappa C_{\kappa\lambda}^\dagger\gamma^\mu(1+\gamma^5)u_j^\lambda)] \tag{3.33}$$

This Lagrangian is much simpler than the weak interaction Lagrangian as we only have two types of terms. In the line 3.29 are the kinetic and mass term of the 4 types of fermions defined. e^λ, with $\lambda = 1, 2, 3$, are the three generations of charged leptons, so electron, muon and tau. Similar are ν^λ the corresponding neutrinos. As the standard model describes these as massless, they only come with a kinetic term and no mass term. u^λ and d^λ are the three up-type and down-type quarks.

The interaction with a photon is given in line 3.30. As the neutrinos are not electrically charged they don't appear here. The relative coupling strength for the charged lepton, the up-type and the down-type quarks are

$1 : \frac{2}{3} : \frac{1}{3}$ corresponding the electric charges of the three particle types. The γ^μ are four anticommutation matrices which represent a Clifford algebra. One of several option of defining them is:

$$\gamma^1 = \begin{pmatrix} 0 & 0 & 0 & -i \\ 0 & 0 & -i & 0 \\ 0 & i & 0 & 0 \\ i & 0 & 0 & 0 \end{pmatrix}, \qquad \gamma^2 = \begin{pmatrix} 0 & 0 & 0 & -1 \\ 0 & 0 & 1 & 0 \\ 0 & 1 & 0 & 0 \\ -1 & 0 & 0 & 0 \end{pmatrix}$$

$$\gamma^3 = \begin{pmatrix} 0 & 0 & -i & 0 \\ 0 & 0 & 0 & i \\ i & 0 & 0 & 0 \\ 0 & -i & 0 & 0 \end{pmatrix}, \qquad \gamma^4 = \begin{pmatrix} 1 & 0 & 0 & 0 \\ 0 & 1 & 0 & 0 \\ 0 & 0 & -1 & 0 \\ 0 & 0 & 0 & -1 \end{pmatrix}$$

Lines 3.31 - 3.33 describe the three-point interactions of the Z^0 or $W^\pm$ boson with two fermions. As the Z boson is electrically neutral, the two fermions in the Z^0 interaction can be either a pair of charged leptons, a pair of neutral leptons, a pair of up-type quarks or a pair of down-type quarks. Mixing between these 4 types is not possible with a Z^0. With the $W^\pm$ on the other hand there is the requirement of having a pair of a charged and a uncharged lepton or a pair of a up-type and a down-type quark in the 3 point interaction with the $W^\pm$. A mixing between quarks and leptons also does not happen. But contrary to the Z^0 interaction, the quark – $W^\pm$ interaction allows for the change in generation (here index κ and λ). The strength of the mixing between the different combinations quarks is given by the magnitude of Cabibbo–Kobayashi–Maskawa matrix C elements [87]:

$$\begin{aligned} C &= \begin{pmatrix} |V_{ud}| & |V_{us}| & |V_{ub}| \\ |V_{cd}| & |V_{cs}| & |V_{cb}| \\ |V_{td}| & |V_{ts}| & |V_{tb}| \end{pmatrix} \\ &= \begin{pmatrix} 0.097446 \pm 0.00010 & 0.22452 \pm 0.00044 & 0.00365 \pm 0.00012 \\ 0.22438 \pm 0.00044 & 0.97359^{+0.00010}_{-0.00011} & 0.4214 \pm 0.00076 \\ 0.00896^{+0.00024}_{-0.00023} & 0.04133 \pm 0.00074 & 0.999105 \pm 0.000032 \end{pmatrix} \end{aligned}$$

The term for these interactions makes use of the γ^5 matrix, which is just a combination of the other four γ matrices:

$$\gamma^5 = \gamma^1\gamma^2\gamma^3\gamma^4 = \begin{pmatrix} 0 & 0 & -1 & 0 \\ 0 & 0 & 0 & -1 \\ -1 & 0 & 0 & 0 \\ 0 & -1 & 0 & 0 \end{pmatrix}$$

Fermion-Higgs boson coupling The Lagrangian for the fermion-Higgs boson coupling is:

$$\mathcal{L}_{fH} = \frac{ig}{2\sqrt{2}}\frac{m_e^\lambda}{M}[-\phi^+(\bar{\nu}^\lambda(1-\gamma^5)e^\lambda) + \phi^-(\bar{e}^\lambda(1+\gamma^5)\nu^\lambda)] \tag{3.34}$$

$$- \frac{g}{2}\frac{m_e^\lambda}{M}[H(\bar{e}^\lambda e^\lambda) + i\phi^0(\bar{e}^\lambda\gamma^5 e^\lambda)] \tag{3.35}$$

$$+ \frac{ig}{2M\sqrt{2}}\phi^+[-m_d^\kappa(\bar{u}_j^\lambda C_{\lambda\kappa}(1-\gamma^5)d_j^\kappa) + m_u^\lambda(\bar{u}_j^\lambda C_{\lambda\kappa}(1+\gamma^5)d_j^k)] \tag{3.36}$$

$$+ \frac{ig}{2M\sqrt{2}}\phi^-[-m_d^\lambda(\bar{d}_j^\lambda C^\dagger_{\lambda\kappa}(1+\gamma^5)u_j^\kappa) - m_u^\kappa(\bar{d}_j^\lambda C^\dagger_{\lambda\kappa}(1-\gamma^5)u_j^k)] \tag{3.37}$$

$$- \frac{g}{2}\frac{m_u^\lambda}{M}H(\bar{u}_j^\lambda u_j^\lambda) + \frac{ig}{2}\frac{m_u^\lambda}{M}\phi^0(\bar{u}_j^\lambda\gamma^5 u_j^\lambda) \tag{3.38}$$

$$- \frac{g}{2}\frac{m_d^\lambda}{M}H(\bar{d}_j^\lambda d_j^\lambda) - \frac{ig}{2}\frac{m_d^\lambda}{M}\phi^0(\bar{d}_j^\lambda\gamma^5 d_j^\lambda) \tag{3.39}$$

All of the lines contain the Higgs boson ghost particles. Therefore only the first term in the lines 3.35, 3.38 and 3.39 describe a three-point interaction which is observable. All the terms are proportional to the ratio of the fermion mass over the vector boson mass M.

Fermion strong interaction The Lagrangian describing the interaction between fermions under the strong force is:

$$\mathcal{L}_{fc} = \frac{1}{2}ig_s(\bar{q}_i^\sigma\gamma^\mu\lambda_{ij}^a q_j^\sigma)g_\mu^a \tag{3.40}$$

This Lagrangian only contains quarks and gluons, as the quarks are the only fermions interacting under the strong force due to their color charge (lower index i and j). The six quarks are differentiated under the strong force and are therefore in this line as a summation index σ, which is summed over up, down, charm, strange, top and bottom. There are eight 3×3 hermitian traceless matrices λ^a, describing the interaction of the 8 gluons with color charge pairs of the quarks:

$$\lambda^1 = \begin{pmatrix}0&1&0\\1&0&0\\0&0&0\end{pmatrix} \qquad \lambda^2 = \begin{pmatrix}0&-i&0\\i&0&0\\0&0&0\end{pmatrix} \qquad \lambda^3 = \begin{pmatrix}1&0&0\\0&-1&0\\0&0&0\end{pmatrix}$$

$$\lambda^4 = \begin{pmatrix}0&0&1\\0&0&0\\1&0&0\end{pmatrix} \qquad \lambda^5 = \begin{pmatrix}0&0&-i\\0&0&0\\i&0&0\end{pmatrix} \qquad \lambda^6 = \begin{pmatrix}0&0&0\\0&0&1\\0&1&0\end{pmatrix}$$

$$\lambda^7 = \begin{pmatrix}1&0&0\\0&-1&0\\0&0&0\end{pmatrix} \qquad \lambda^8 = \frac{1}{\sqrt{3}}\begin{pmatrix}1&0&0\\0&1&0\\0&0&-2\end{pmatrix}$$

Faddeev-Popov ghost strong interaction The Lagrangian for the Faddeev-Popov ghosts in the strong interaction is:

$$\mathcal{L}_{FPc} = \bar{G}^a \partial^2 G^a + g_s f^{abc} \partial_\mu \bar{G}^a G^b g_\mu^c \tag{3.41}$$

As these are fictitious particles like the higgs ghosts, they do not represent observable particles and interactions. They can only appear in internal loops and are necessary to preserve the consistency of path integrals.

Faddeev-Popov ghost weak interaction Like for the strong interaction there is also a Lagrangian for Faddeev-Popov ghosts in the weak interaction:

$$\mathcal{L}_{FPw} = \bar{X}^+(\partial^2 - M^2)X^+ + \bar{X}^-(\partial^2 - M^2)X^- + \bar{X}^0\left(\partial^2 - \frac{M^2}{c_w^2}\right)X^0 + \bar{Y}\partial^2 Y \tag{3.42}$$

$$+ igc_w W_\mu^+(\partial_\mu \bar{X}^0 X^- - \partial_\mu \bar{X}^+ X^0) + igs_w W_\mu^+(\partial_\mu \bar{Y} X^- - \partial_\mu \bar{X}^+ Y) \tag{3.43}$$

$$+ igc_w W_\mu^-(\partial_\mu \bar{X}^- X^0 - \partial_\mu \bar{X}^0 X^+) + igs_w W_\mu^-(\partial_\mu \bar{X}^- Y - \partial_\mu \bar{Y} X^+) \tag{3.44}$$

$$+ igc_w Z_\mu^0(\partial_\mu \bar{X}^+ X^+ - \partial_\mu \bar{X}^- X^-) \tag{3.45}$$

$$+ igs_w A_\mu(\partial_\mu \bar{X}^+ X^+ - \partial_\mu \bar{X}^- X^-) \tag{3.46}$$

$$- \frac{1}{2} gM[\bar{X}^+ X^+ H + \bar{X}^- X^- H + \frac{1}{c_w^2}\bar{X}^0 X^0 H] \tag{3.47}$$

$$+ \frac{1 - 2c_w^2}{2c_w} igM[\bar{X}^+ X^0 \phi^+ - \bar{X}^- X^0 \phi^-] + \frac{1}{2c_w} igM[\bar{X}^0 X^- \phi^+ - \bar{X}^0 X^+ \phi^-] \tag{3.48}$$

$$+ igMs_w[\bar{X}^- Y \phi^- - \bar{X}^+ Y \phi^+] + \frac{1}{2} igM[\bar{X}^+ X^+ \phi^0 - \bar{X}^- X^- \phi^0] \tag{3.49}$$

These interactions are, as the strong interactions, only allowed in internal loops. They are not observable as such and are a necessary mathematical tool to preserve the consistency of path integrals.

3.2 Exotic model of a b^*

Even though the Standard Model is a very well tested theory, there are some observations which are not explained by the Standard Model [56]. There are many theories describing physics beyond the Standard Model. A possible theory to explain the structure and pattern of the fermion masses is provided by composite models. In these, the quarks and leptons would be composites

of fundamental particles. A convincing evidence of a composite nature would be the existence of excited versions of the quarks and leptons [48].

In this thesis, we focus on excited quarks and especially the excited form of the b quark, which we call b^*. This b^* couples to the gluon, W, Z, higgs boson and photon. As done in [76], we assume a sizable anomalous color-magnetic coupling and a suppressed anomalous electroweak magnetic coupling. This allows for a single b^* production using a gluon and b quark from the two colliding protons and decay either into gb, Wt, Zb or Hb and the heavily suppressed decay $b^* \to \gamma b$. The Lagrangian for the strong interaction of the b^* is:

$$\mathcal{L}_{b^*,\text{colour}} = \frac{1}{2} i g_s \bar{b}_i^* \gamma^\mu \lambda_{ij}^a b_j^* g_\mu^a + \frac{g_s \lambda}{\Lambda} i G_\mu \bar{b} \sigma^{\mu\nu} (\kappa_L^b P_L + \kappa_R^b P_R) b^* \tag{3.50}$$

Here the first term is exactly the quark – gluon interaction as for all other quarks in the Standard Model. So the gluon interaction with two b^* is just added. The second term is the more interesting, as this one couples a gluon to a Standard Model b and the excited b^*. Here two parameters are at play, λ which is a free parameter. It is set to $\lambda = 1$ for practical purposes. The other parameter is Λ and this one is the scale at which the new interaction takes place. The best guess of this scale is the mass of the particle $\Lambda = m_{b^*}$. $P_L = \frac{1-\gamma^5}{2}$ and $P_R = \frac{1+\gamma^5}{2}$ are projection operators and with non-vanishing κ_L and κ_R, both left- and right-handed b^* can couple to the Standard Model b-quark.

The coupling to the weak vector bosons and the higgs boson is described with the Lagrangian:

$$\mathcal{L}_{b^*,\text{weak}} = \frac{i g_2}{\sqrt{2}} W_\mu^- \bar{t} \gamma^\mu (f_L P_L + f_R P_R) b^* \tag{3.51}$$

$$+ \frac{i g_2}{2 c_w} Z_\mu \bar{b} \gamma^\mu (F_L P_L + F_R P_R) b^* \tag{3.52}$$

$$+ \frac{i m_b}{\nu} H \bar{b} (y_L P_L + y_R P_R) b^* \tag{3.53}$$

Here we have again the projection operators P_L and P_R and independent coupling parameters for left- and right-handed b^*. $\nu = \frac{2M_W}{g}$ is the vacuum expectation value of the Higgs field.

In order to understand the properties of the b^* we need to know the decay width depending on the different coupling parameters and the mass. The partial decay widths are also given in [76]:

$$\Gamma(b^* \to bZ) = \frac{g_2^2}{128 \pi c_w^2} \frac{m_{b^*}^3}{m_Z^2} (F_L^2 + F_R^2)(1 - x_Z^2)^2 (1 + 2x_Z^2) \tag{3.54}$$

$$\Gamma(b^* \to tW) = \frac{g_2^2}{64\pi} \frac{m_{b^*}^3}{m_W^2} (f_L^2 + f_R^2)(1 - x_t^2)^3 \tag{3.55}$$

$$\Gamma(b^* \to bh) = \frac{g^2}{128\pi} \frac{m_{b^*}^3}{m_W^2} (y_L^2 + y_R^2)(1 - x_h^2)^2 \tag{3.56}$$

$$\Gamma(b^* \to gb) = \frac{g_s^2}{12\pi} m_{b^*} (\kappa_L^2 + \kappa_R^2) \tag{3.57}$$

with $x_Z = \frac{m_Z}{m_{b^*}}$, $x_W = \frac{m_W}{m_{b^*}}$, $x_h = \frac{m_h}{m_{b^*}}$ and $x_t = \frac{m_t}{m_{b^*}}$.

Chapter 4

Sample production

4.1 Signal samples

In order to search for new particles like excited quarks, we first need to understand how they would manifest themselves in the ATLAS detector. In order to do this, we need to simulate the creation and decay of many of these particles and the detector response to the decay products.

4.1.1 Feynman diagram

The first step in this simulation is the determination of the process we want to generate. In this thesis, we are looking for a b^* decaying into Wt. According to [48], the highest partial width is $gb \to b^*$ and the second highest $b^* \to Wt$. The production of the b^* has to happen from two protons interacting. Thus the density of the partons required for the production multiplied with the partial width determines the fractions of the production. The highest partial width has the $b^* \to gb$ vertex with 83.4% of the total width. The alternative vertices $Zb \to b^*$, $\gamma b \to b^*$ and $Wt \to b^*$, not only require a third generation quark out of the sea quarks of the proton and also a boson less abundant in the proton than the gluon. Therefore it is safe to assume that the main b^* production mode is $gb \to b^*$.

To define which decays we need, we have to look forward to the intended analysis. In order to keep the backgrounds reasonably low, we require a single lepton. Primarily we will look at masses of the b^* quark, which are much greater than the mass of the Z or W bosons. Thus the decay products of the boson stay close together due to the high boost. In combination with the requirement of exactly one lepton, the fraction of $b^* \to Zb$ entering the analysis is expected to be small, as we do not expect many events where one lepton from the Z is identified but the other is not.

Given these reasons, we can safely create the process $gb \to b^* \to Wt$ and expect to produce the bulk of the b^* events for this analysis. Obviously this

does not describe the full model, but the sample can be used to obtain a lower bound on the expected number of events from a b^*. Therefore we would have to revisit this more closely if we would want to create a measurement and not just an exclusion limit.

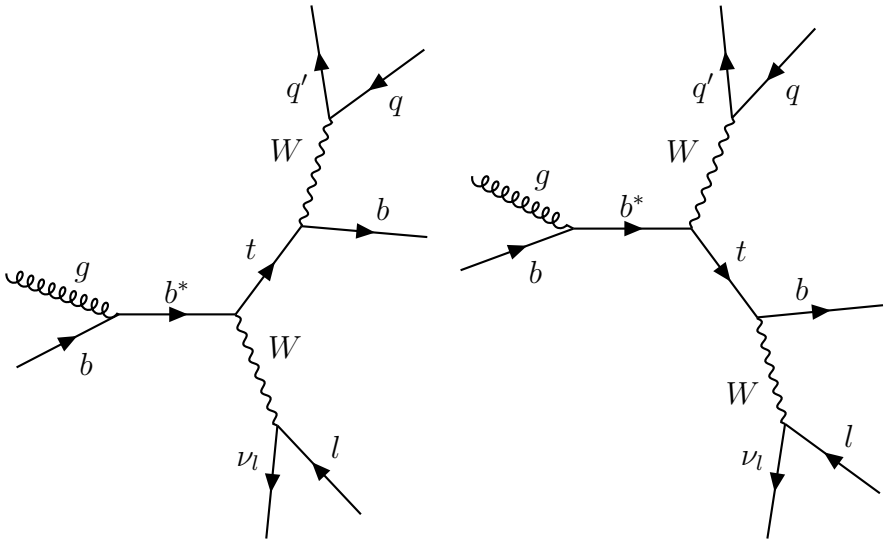

Figure 4.1: Feynman diagrams of main signal production and decay process. Diagrams (a) and (b) show the two options of either of two W bosons decaying hadronically and the other leptonically.

4.1.2 MadGraph configuration

MadGraph5 aMC@NLO [36] is a software to create events from a process. It comes with a description of the Standard Model and several different models of new physics. They can be enabled in the configuration of the process we want to generate. For the b^*, the model is not included by default. So the model from the paper [76] was used. This model adds the anomalous coupling needed to produce the excited b^*. With the Standard Model and the model adding the b^*, we configured MadGraph as follows to produce the events we are looking for:

```
import model Bprime
define p = p b b~
define l- = e- mu- ta-
define l+ = e+ mu+ ta+
define vl = ve vm vt
define vl~ = ve~ vm~ vt~
```

```
define tt = t t~
define WW = w+ w-
define bb = b b~
define bstar = bp bp~
define lep = l+ l- vl vl~
define q = u d s c b u~ d~ s~ c~ b~
generate p p > WW tt QAD=2 QCD=0 QED=0, tt > bb lep lep, WW > lep lep
add process p p > WW tt QAD=2 QCD=0 QED=0, tt > bb q q, WW > lep lep
add process p p > WW tt QAD=2 QCD=0 QED=0, tt > bb lep lep, WW > q q
```

This script does the following:

1. Import the model containing b^* to be used, it is called Bprime for historic reasons.

2. Tell madgraph we want to utilize a proton in a five flavour scheme, which also can contain a b and $\bar{b}$, not only gluons and the quarks u, d, s, c and anti-quarks $\bar{u}, \bar{d}, \bar{s}, \bar{c}$.

3. Define aliases for the used particle classes and combine them so particle and anti-particle production happens simultaneously.

   - The b^* is called bp in the model configuration.

4. Create three orthogonal processes of two protons going into W and t with the successive decay of the t and W where:

   (a) both W-bosons decay into leptons.

   (b) the W-boson directly from the b^* decays into leptons, the W-boson from the t-quark into non t quarks.

   (c) the W-boson from the t-quark decays into leptons, the W-boson directly from the b^* into non t quarks.

5. The modifier QAD=2 requests MadGraph to have two vertices of the anomalous coupling and thus have a b^* somewhere in the diagram.

The case of both W decaying into quarks was deliberately left out in order to have a higher fraction of events produced with the one lepton we are looking for. But MadGraph is aware that these cases would exist. So the cross section calculated is only the cross section times branching ratio fractions for this specific combination of processes we requested to be produced. To calculate quantities like the cross section, MadGraph needs to know the momentum fraction of the proton constituents. They are modeled by parton distribution functions (PDF). As PDFs are not yet calculable from first principles, they are obtained by fitting data from several experiments to describe the proton

parton density over a huge momentum fraction range. Due to the high number of free parameters in these distributions, there are several parton distribution functions calculated by different groups. So many even, that there is a special library, LHAPDF [52], to collect all of them in an interchangeable way. For the production of the b^* signal sample we chose NNPDF3.0 [93] in its leading-order variant with an $\alpha_s = 0.130$ and five quark flavors, to match the leading order process we are generating which requires a b quark in the proton.

In order to validate the choice of assuming the b as part of the parton sea at PDF level, a single sample for comparison was created in the four flavour scheme, where the necessary b quark was obtained by MadGraph using a gluon from the proton and splitting it into $b\bar{b}$. As this gluon splitting is the underlying process of the sea quark formation, both methods should create physically the same result. The changes necessary to have MadGraph do the gluon splitting explicitly are rather small. They involve only the removal of the b quarks in the proton definition in the MadGraph configuration file, the addition of an explicit b in the decay chain and the change of the PDF to the NNPDF3.0 variant with only four quark flavors in the proton.

4.1.2.1 Mass and width of the b^* quark

Neither the mass nor the width of the b^* quark are known or predicted. Therefore we create several samples of the b^* which mainly differ in the assumption of the mass. In order to assign a width to every mass we also have to make an assumption about the coupling parameters. As there is a priori no fundamental constraint on the coupling parameters, they are assumed to be of $O(1)$ and therefore we set the gluon and W coupling parameters to $\kappa_L = 1, \kappa_R = 0$ and $f_L = 1, f_R = 0$, as in [76]. For the full width of the b^*, we also need the Z and h coupling parameters, which are set to $F_L = 1, F_R = 0$ and $y_L = 1, y_R = 0$. With this configuration, we get the width from the sum of equations 3.54 to 3.57 for each mass. The resulting calculated values are tabulated in table 4.1.

These widths are smaller than 10 % of the mass and thus we don't expect to be able to resolve them. As the couplings chosen for these are already at the upper end of being reasonable, we don't need to create more samples with different widths in order to set limits on smaller couplings.

4.1.3 Showering with Pythia8

MadGraph takes the given processes, calculates the matrix elements and creates an event distribution accordingly. But these events only contain the part of the interaction which involves the directly used partons of the proton and the final state particles explicitly defined in the process. But we also need to take care of more effects of the interaction. This is done with Pythia8.2.

Mass [GeV]	Width [GeV]
400	12.4
600	26.5
1000	47.6
1200	57.8
1400	68.0
1600	78.1
1700	83.1
1800	88.2
2000	98.2
2200	108

Table 4.1: Masses and widths in of the b^* as used in the sample production.

It takes the events produced by MadGraph and modifies them to take the remaining effects into account. The full list of things taken care by Pythia8.2 is given in [84], but some are highlighted here.

The most relevant effect is the hadronization, which is the addition of new quark pairs and gluons to create color neutral objects. This is necessary, because the final state particles out of madgraph usually fly in different directions and if they are quarks or gluons, they are not color neutral. As the initial state protons are color neutral and all final state particles have to be color neutral, Pythia has to take care that the color flow is maintained and hadronize quarks as necessary.

Another important effect processed by Pythia is the initial- and final state radiation. In these, the particles in the initial or final state can radiate gluons or photons and thus increase the number of final state particles even more. This part is neglegted in MadGraph as the computation of the matrix element becomes more involved the more particles enter the calculation.

Pythia also takes care of the proton remnant. Therefore it knows when a b quark is taken from the proton for the hard process. In these cases it adds a second b to the proton remnant to preserve flavor numbers. Thus we expect to create very similar event topologies independent of whether we have a $b\bar{b}$ production in the hard process or only implicit in the proton remnant.

4.1.4 Detector simulation

After each event is processed by Pythia8.2, the events contain the final state particles of the produced process or their decay products. But in order to measure anything, these particles have to interact with the detector. So the next step in the simulation chain is the simulation of the interaction of all the particles with the material of the detector. This requires a full 3D model of all components in the ATLAS detector, which includes not only actively

measuring detectors but also all services and support structures.

One approach to do this simulation is by using Geant4 [32, 34, 35], which uses physics models to simulate the interaction of all the particles with all detector components they traverse and interact with. The interactions, especially in the calorimeters, create also showers of particles, which increases the amount of particles to be simulated really fast and is therefore quite computation intensive.

In order to reduce the amount of time needed to simulate the events, two shortcuts are applied in the simulations we use here. One of these is the use of frozen showers [44, 45], where the energy distribution pattern for many different particle interactions with the FCAL is simulated once in Geant4 and then stored in a database. When the simulation then needs to shower a particle in an event, the energy deposition pattern is read from this database, thus saving a significant amount of time compared to recalculating the full showering process over and over.

To reduce the computing time required in the other calorimeters, their response is parameterised [83] based on Geant4 simulations of electron, photons and charged pions entering the electromagnetic- and hadronic calorimeters. Electrons and photons are chosen to simulate the effect of electromagnetic showers, where as the pions represent the generic hadronic particle of hadronic showers. The parametrisation of the detector responses is obtained by using a fine grid of energies and pseudo rapidities of these single particles. Random sampling of the individual responses is used to build the detector response for the event. Even though the average shower shape is modelled well, substructure of jets is not. Therefore we can only use this simulation techique reliably if we don't require jet sub-structure for the analysis, like this analysis [39].

Two different combinations of these methods are used in the samples we use. Some samples are produced in "full simulation", which uses for most of the detector response the direct Geant4 simulation and only for the FCAL frozen showers are used. Most of the signal samples are produced with "AtlFast2" configuration, which uses Geant4 only in the tracker and muon system and frozen showers and a parameterised calorimeter response in the calorimeters.

4.1.4.1 Pile-up

After we have the detector responses for all the particles in the event, we need to add some more energy coming from interactions happening independent of the process we are interested in. Additional effects which create energy deposits in the detector are additional proton-proton interactions in the same event, beam halo, beam – gas, cavern background events and energy deposited in neighboring bunch crossings due to long signal integration times. These

are collectively called pile-up. As these are between other protons or even from outside the detector, they are completely independent of the process we are interested in. Thus, the most efficient way to add them to the simulation is by adding typical energy distributions of these processes to the event. As the processes are partially dependent on how many protons collide in a given bunch crossing, a certain distribution of these effects is assumed, as can be seen in figure 4.2, with the goal to cover most of the conditions during data taking [26].

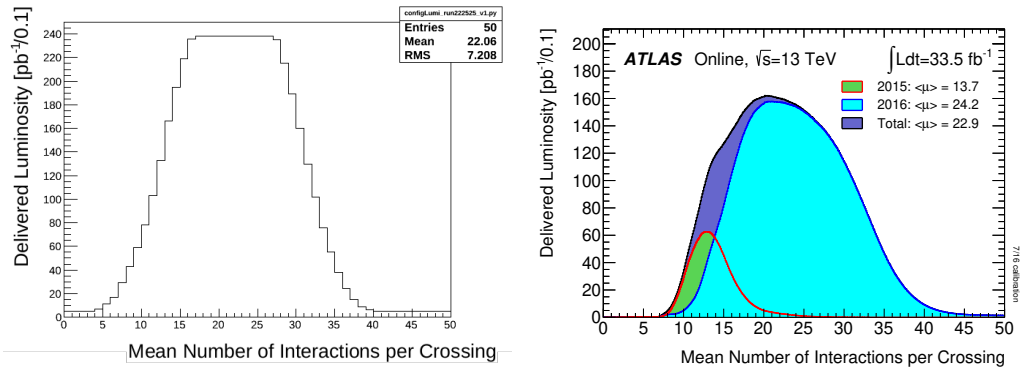

(a) (b)

Figure 4.2: (a) Luminosity distribution as a function of mean number of interactions per bunch crossing used for the simulation [75] and (b) the observed distribution in the 2015/2016 data taking [94]

4.1.4.2 Digitization

With all the energy deposits in place, the response of all components in the detector is simulated. This step also takes noise of the detector components into account.

4.1.5 Reconstruction

The simulated events after the digitization step are in the same data format as data recored with the actual detector. So from here onwards, the same tools are applied to data and simulation. The next step is to extract objects which are then used in the analysis itself. These objects are for example jets, electron candidates, muon candidates, photon candidates, tau candidates and an imbalance in the transverse deposited energy (E_T^{miss}). Section 5 will describe the objects used in this analysis in more detail.

4.2 Standard Model background samples

To create the full analysis, we don't only need to understand how the searched process is recorded by our detector, but also all the other processes from the Standard Model which are passing the same selection requirements. Therefore, we also need a collection of samples describing Standard Model processes, which are considered background in this analysis. The primary selection criterium for the processes in our background selection is an expectation, that a given process can create a signature matching our selection criteria and happens with a sufficiently high cross-section. Therefore we can focus on relatively simple processes like production and decay of $t\bar{t}$ pair, single top or W bosons. Processes with more complex internal structure are not only more difficult to calculate, but also have lower cross-sections.

The analysis aims for a single lepton (electron or muon) coming from one of two W in the process as well as a b quark coming from a t decay. Technically, we also have a second b in the proton remnant, but it is not required, that this one can be always detected. So we expect that we get most of our background events from the production and decay of $t\bar{t}$ pairs, as they have in their final state also two W bosons and two b quarks. Another relevant background is the production and decay of a W boson. The decay products of the W boson alone are not sufficient, but it is certainly possible to have initial state radiation producing a pair of b quarks and more hadronic activity. Also the production of a single top quark can fulfill the requirements of our final state.

We also add samples, which do not have such an obvious overlap with our intended selection, but may be able to contribute in cases where individual decay products are not identified properly. The most obvious process for such a case is the production and decay of a Z boson. Obviously we would expect either zero or two leptons here, but there can be cases where either one lepton was not properly identified, maybe due to overlap with hadronic activity. Or it was not visible to the detector due to a trajectory not passing through the necessary active components. Other processes just have a very low production cross section, like multi-boson events. The full list of samples is given in appendix A.

The general production chain for the background samples is the same as outlined for the signal samples in section 4.1. Depending on the specific sample, there are some differences though. One major difference is the use of different software packages to calculate the Feynman diagrams and do the showering. Instead of MadGraph + Pythia, the W and Z boson samples use Sherpa in the version 2.2.1 and the multi-boson samples use Sherpa in the version 2.2.0 [62]. The $t\bar{t}$ and single t samples use Powheg [74, 59, 33] to calculate the Feynman diagram interaction and do the showering with Pythia6 and Pythia8. The choice of generator for these Standard Model processes is

driven by reasonable agreement in other analyses. Also these samples are not generated at leading order, like the b^* signal samples are, but rather at next-to-leading order in QCD, which means they include all Feynman diagrams with a gluon or quark loop but have the same in- and out-going particles. This again improves agreement with measurements significantly. These calculations at next-to-leading order mostly change the cross section for each process. In order to incorporate these better calculations, the cross sections are modified by a k factor which scales the leading order cross section to the next-to-leading order one. These k factors are also given in the table in appendix A.

The single W or Z boson production is a relatively high cross section process. But most of the interactions producing W or Z utilize much less energy than our signal production. Thus we are mostly interested in a small fraction of the W and Z events which are in an extreme phase space. And so are most analyses searching for new particles. Thus the statistics in the interesting region is increased by dividing the samples by the final particle types and the energy involved in the interaction. This is achieved by adding a filter step in between the showering and the detector simulation. As the Feynman diagram calculation and the showering is relatively fast compared to the detector simulation it is feasible to produce a relatively high number of events even at extreme phase spaces. The filter used to separate the samples based on particles is a B Hadron filter, which categorizes events into ones which conatain a B hadron and events which don't. Events which contain a B hadron are referred to as "heavy" jet events where as events which don't contain a B hadron are referred to as "light" jet events. The relative filter efficiencies for the different samples are also given in the table in appendix A.

Another parameter, which is in general different between these samples, is the choice of the PDF. For most samples, NNPDF3.0 was used, but as these samples where produced at next-to-leading order, higher-order versions of the NNPDF3.0 set where chosen. Only the multi-boson samples use CT10 [70], which is a PDF from a different group.

4.3 Data driven backgrounds

In addition to the background which is produced by Standard Model processes with signatures fitting our selection, there is also the possibility to have objects mis-identified and thus resulting in a positive selection. The two most common cases where a mis-identification can happen are the identifications of a b-tagged jet and a lepton candidate. For the b-tagged jet, this is not a big problem, as this does not open up more different processes we didn't account for so far. The main source of contamination here are the W+light jets processes and assuming proper modeling of the b-tagging mis-identification

in the simulation, this should be covered by our background sample selection.

A bigger problem is the mis-identification of a jet as a lepton. There the ensemble of Standard Model processes is much bigger, as essentially any high momentum multijet event with a b-jet can pass the signal selection when one of the jets is misidentified as a lepton. And as the LHC is a hadron collider, most of the events are multijet events. Therefore estimating the contamination from fake leptons solely based on simulations would be very computation intensive and is not common in ATLAS. The approach we chose here is described in section 5.1.3. It is a data driven approach where the rate of real and fake identifications is determined using two different qualities of lepton identification and comparing data and simulation in specifically chosen regions.

Chapter 5

Object definition

We now have the signal and background events simulated to a point where the expected detector response is like the response of the real ATLAS detector. The next step is the reconstruction of these detector responses into objects which represent candidates of real physical entities. Within the ATLAS collaboration several possible sets of object definitions are available and an analysis can choose one. The main constraints for this choice are the compatibilty of calibration phase space with the analyis and the availabilty of recipies for systematic uncertainties on the object paramters.

This analysis is looking for events with a single lepton in the final state. Thus an electron or a muon candidate is required. Also there are jets of hadrons from our signal, which might be from a b quark. Other jets of hadrons come from the decay of a W boson which has to first order the momentum equivialent of half of the b^* mass. Thus the two jets from the W are close together. So if we use a jet definition, which can accommodate the jets of both quarks from the W decay, it would describe the full W. If the W from the t decay is the one which decays hadronically and the b is also close enough, the jet object might even contain the full t decay chain. As we require a single lepton from the second W in our signal sample, we know that there must be a neutrino as well.

5.1 Leptons

The aim of the analysis is to search for events with at least one lepton. Tau leptons decay to fast to be detected before they decay and because they decay quite often into pions, they are quite difficult to identify efficiently. So this analysis focuses on electrons and muons. As we don't look for tau decays specifically, we also don't reject events where a tau decays into an electron or muon.

As we require always one lepton we chose triggers based on the presence

of a lepton in the event.

5.1.1 Electrons

Electrons are charged particles and thus are tracked by the inner detector. In the calorimeter system, they are predominantly stopped by the electromagnetic calorimeters. The tracking of the electrons is used to distinguish them from photons or photons converting into electron – positron pairs. The photon conversion is primarily rejected by requiring a hit in the IBL. Several hits along the track in the tracker are required. The transition radiation measurement of the TRT is used to further differentiate electrons from other charged particles like pions. The shape of the energy deposition in the calorimeter is further used to distinguish electrons from hadrons. As we require that we have a high purity of electrons in the electron candidates, just looking at the calorimeter energy deposition topology is not enough to reject as much hadronic activity as necessary. Therefore additional isolation requirements are used. This analysis uses a combination of isolation in the calorimeter and in the tracker from other activity. In the calorimeter, a cone of $\Delta R = 0.2$ is investigated and the energy deposit within the cone but outside of the barycentral $|\Delta\eta|\times|\Delta\phi| = 0.125 \times 0.175$ is used. An (E_T, η) dependent correction is applied to account for leakage. Additional to the isolation requirement in the calorimeter, a track based isolation is also required. In this case, a cone of $\Delta R = \min\left(0.2, \frac{10\,\mathrm{GeV}}{E_T}\right)$ is used to reduce the cone size for high-momentum electrons.

Due to the requirement of a tracking detector, electrons are identified up to $|\eta| < 2.47$. With the services running in between the barrel and end-cap calorimeter, the two cone shells of $1.37 < |\eta| < 1.52$ are vetoed for electron identification to keep the energy resolution more homogeneous [7, 11, 6].

The trigger system is able to identify electron candidates. Single electrons are used to trigger the events we are interested in. Due to the high interaction rates, a combination of different trigger thresholds are required. Three thresholds ($p_T > 24\,\mathrm{GeV}, p_T > 60\,\mathrm{GeV}, p_T > 120\,\mathrm{GeV}$) with decreasing isolation and identification quality requirements are used. This allows for relatively consistent isolation and quality criteria to be applied in the offline analysis with high efficiencies especially for high-momentum electrons. In order to be in the plateau of the trigger efficiency, only electrons with $p_T > 28\,\mathrm{GeV}$ are used.

5.1.2 Muons

Muons are also charged particles and thus trackable in the inner detector. But as they deposit relatively little energy in the calorimeters, they cannot be

stopped by them. Therefore, the muon system as an additional tracker just for muons. This analysis uses relatively high-purity muons and therefore requires muons reconstructed in the muon system. It is also possible to associate tracks in the inner detector to the muon candidates, but this is not necessary for our muon definition. To have a similar acceptance as electrons, muons are only identified up to $|\eta|< 2.5$.

As with electrons, muons are a good source for triggering the events. The muon system comes with several trigger systems. Like for electrons, the high interaction rates make it necessary to use three different trigger thresholds for single muons with varying isolation and quality criteria. In order to be in the plateau of the trigger efficiency, only muons with $p_T > 28\,\text{GeV}$ are used.

Muons can also be created as decay products of hadronic decys. Therefore, the same isolation cuts as for electrons are applied. Especially the calorimeter isolation is applied as well, even though the calorimeter is not used to identify muons otherwise, but bigger energy deposits close to the muon candidate are a good indication of a muon originating from a hadronic shower [28].

5.1.3 Fake leptons

Electrons and muons are the primary selector for this analysis and provide a good discrimination from a huge number of the hadronic events. To get an estimate how many events in our selection don't actually contain an electron or muon from the primary process, but rather misidentified hadronic activity a Matrix Method is used [1]. The idea is that we can extrapolate the effect by looking at the selection efficiencies for two different lepton selections. One selection is our nominal selection, which we call tight. The other selection is a more loose selection, which does not require the isolation criteria for either electrons or muons and does not use the transistion radiation measurement of the TRT for electrons. With these two lepton definitions, we can express the number of tight leptons N^t and loose leptons N^l as:

$$N^l = N^l_r + N^l_f \tag{5.1}$$

$$N^t = \epsilon_r N^l_r + \epsilon_f N^l_f \tag{5.2}$$

where N^l_r is the number of real leptons in the loose selection and N^l_f is the number of fake leptons in the loose selection. The ϵ_r and ϵ_f are the efficiencies with which real and fake loose leptons pass the tight selection. These efficiencies are derived in specially crafted control regions. The real efficiencies are obtained with a tag-and-probe method from $Z \to ll$ events. The fake efficiencies are obtained in a region with a low fraction of real leptons. This region utilizes the feature, that single real leptons are only produced by a decaying W. But these decays also produce a neutrino and thus E_T^{miss}. So a low E_T^{miss} upper cut can be used to decrease the fraction of real single leptons.

Additionally the simulated background containing real leptons is subtracted [57].

Our contamination of the tight selection with fake events is then:

$$N_f^t = \frac{\epsilon_f}{\epsilon_r - \epsilon_f}(\epsilon_r N^l - N^t). \tag{5.3}$$

ϵ_r and ϵ_f are quite dependent on the kinematics of the event. As these efficiencies cannot be determined with high statistics in the signal region phase space, we expect relatively big uncertainties. But this method gives at least some insight into this background. And we will see later, that this background source is not a very big one. Therefore, this relatively simple method is sufficient.

5.2 Jets

Hadronic jets are measured in the calorimeters of ATLAS. They are a collimated collection of energy deposits in the calorimeter. Thus they are defined by clustering energy entries together. The most common algorithm for jets in ATLAS is the anti-k_t algorithm [54]. The anti-k_t algorithm first defines two distances:

$$d_{ij} = \min(k_{ti}^{-2}, k_{tj}^{-2})\frac{\Delta_{ij}^2}{R^2} \tag{5.4}$$

$$d_{iB} = k_{ti}^{-2} \tag{5.5}$$

with k_{ti}/k_{tj} being the transverse momentum of energy entries, $\Delta_{ij}^2 = (y_i - y_j)^2 + (\phi_i - \phi_j)^2$ the distance between the energy entry under test i and pseudojets j in rapidity y and azimuth ϕ with a free parameter R. The clustering is an iterative process, in which all these squared distances are calculated and in case a d_{ij} is the smallest distance, energies i and j are clustered together and the distances are calculated again. If the distance d_{iB} between the energy entry under test and the jet is minimal, the clustering of this jet is finished.

An important property of this clustering algorithm is safety against co-linear and infrared radiation. This means that neither a co-linear radiation nor a radiation of infinitesimally small energy should change the properties of the clustered object. This is achieved by starting two cluster entries with high transverse momentum close to each other. So co-linear radiation entries cannot cause the jet to split in two. For low energy entries, they are clustered either last and thus cannot move the main momentum much, or not clustered at all in a given jet, if they are too far away ($\Delta > R$). This now also shows us, that R can be understood as the $\eta - \phi$ radius of the jet, as all energy within R around the center-of-mass of a jet is clustered into the jet, and all outside

is not. As there is not only one jet in a given event, all energy entries used to create a jet are removed from the full list and a next jet is constructed until all jets in an event are found.

The energy entries used in ATLAS are not derived from individual calorimeter cells, but rather topological clusters [30] which are noise-corrected and energy-calibrated collections of deposited energy in three dimensional topologically connected calorimeter cells. The calibration of the energy is based on the electromagnetic calorimeter.

This analysis uses two different radius parameters for the clusterization. The most common one in ATLAS is $R = 0.4$ [18]. The other one used is $R = 1$, but this one is created in a special way. Instead of using topological clusters to create these jets, jets from the collection of $R = 0.4$ jets are used to create these $R = 1$ jets. This has the advantage, that we can utilize the detailed calibration we have for the $R = 0.4$ jets. Also as we will see later (Section 6), there is a significant number of systematic effects associated to jets. By using jets for which systematics are already determined, they can just be propagated to these larger jets [12].

Jets with a radius of $R = 0.4$ are required to have a $p_T > 20\,\text{GeV}$ and $|\eta| < 4.5$. In cases where the jet has a $p_T > 60\,\text{GeV}$ and $|\eta| < 2.4$, a Jet Vertex Tagging (JVT) [2] algorithm is used to suppress jets from pile-up by using information from the tracker.

For jets with radius $R = 1$, two sets of requirements are applied. The first one is, that the conditions of the $R = 0.4$ jets are met for all candidate jets for the reclustering. Then after the reclustering, only jets are kept which have $p_T > 50\,\text{GeV}$, $|\eta| < 2.5$ and a trim $f_{\text{cut}} < 0.05$ [67], which means jets with less than 5% of the combined jet transverse momentum are rejected, this helps to reject pile-up induced contamination.

5.2.1 *b*-jets

As we know from our signal, we always expect at least one jet to originate from a b quark, which hadronizes to a B hadron. The method we use for identifying these b-jets is a multi-variate tagging algorithm called $MV2c10$ [8, 21]. The identification of B hadrons is essentially based on the relatively long lifetime of these hadrons $\sim 10^{-12}\,\text{s}$ [87]. This long lifetime results in a secondary vertex which might be resolved by the tracker. Thus to differentiate b-jets from non b-jets, we require to have a tracking detector. And as we are interested in secondary vertices, the most inner pixel detector, the IBL, is the most relevant one for the b-tagging performance, hence the B in the name.

As the tagger is based on a boosted decision tree, it needed to be trained on b-jets, c-jets and light jets, where c-jets are jets originating from a charm quark and light jets from a ligher quark or gluon. As charm containing hadrons also have a sizable lifetime, it is particularly difficult to differentiate

between b- and c-jets, thus they are explicitly added to the training. The specific algorithm $MV2c10$ used 7% of c-jets in the background training sample [8].

b-tagging information is obtained for all of the previously defined $R = 0.4$ jets within $|\eta| < 2.5$ as b-tagging requires the tracking detector. This analysis chooses the 77% working point of the $MV2c10$ tagger, which means that a typical b-jet is identified with 77% chance as such. But it has to be noted here that these 77% are only valid for the typical kinematics of $t\bar{t}$ events, not necessarily for the kinematics we get from our signal. [14]

5.3 Missing transverse momentum

Neutrinos cannot be detected by the detector, but everything else can be. With no transverse momentum in the colliding protons, the sum of all transverse momenta in the final state has to be zero. So it is possible to estimate the amount of transverse momentum carried by the sum of all neutrinos produced by adding up all momenta of all detected energy deposits and muon momenta. This is of particular interest in this analysis as the expected signal decay chain contains only a single neutrino from a leptonic W decay.

The missing transverse momentum E_T^{miss} is calculated using energy deposits in the calorimeters and tracks reconstructed in the inner detector and the muon system. Thereby the momentum of all reconstructed objects is used. So electron candidates, muon candidates, photon candidates and jets. Photons are identified like electrons with the difference, that a photon requires no track pointing to the calorimeter entry. The calorimeter energy distribution of electrons and photons are almost the same. In addition to these reconstructed objects, all tracks originating from the hard scatter collision vertex which are not part of reconstructed objects are summed up and added to E_T^{miss}, the so-called "soft term". [15, 22]

Chapter 6

Systematic Uncertainties

To build the analysis we do not only need the simulated samples and the object definitions, but we also need to unterstand their systematic uncertainties. Simulations are only a good guess of what actually happens and therefore inherently have some systematic uncertainty. Object definitions and their efficiencies are obtained by comparing properties of simulated objects with objects in measured data. This is limited both by statistics for this comparison as well as the choices taken for the selections for comparisons. Also the detector simulation itself has some limitation in describing the real ATLAS detector and thus the response of particles.

6.1 Systematic uncertainties on simulated samples

The most obvious uncertainty for matching simulated samples to data is the luminosity scale factor. In order to scale a simuation correctly to data, we need to know how much integrated luminosity the data represents. And this luminosity measurement has an associated uncertainty, which is in the case of the used 2015/2016 ATLAS data set 2.1%. It is derived following a methodology similar to that detailed in Ref. [17], and using the LUCID-2 detector for the baseline luminosity measurements [42], from calibration of the luminosity scale using $x - y$ beam-separation scans.

In addition to the luminosity uncertainty, the corresponding cross-section of each simulated sample has an uncertainty as well. The uncertainties on the cross-section for the main background processes is given in table 6.1

In addition to the cross-section uncertainties, there are other differences between the different models applied by the different generators and generator configurations. For the main samples, this is taken into account by creating systematic uncertainties from comparing the effect of background samples generated with different generators in the control and signal regions. $t\bar{t}$ and single t backgrounds get this generator uncertainty by comparing the simula-

Process	Cross-section uncertainty	Reference
$t\bar{t}$	6%	[16]
Single top	6.8%	[66]
W+jets	5%	[10]
Z+jets	5%	[10]
Multiboson	6%	[13]

Table 6.1: Cross-section uncertainties of background samples

tion from the nominal sample to an aMC@NLO[36] produced sample. For the W+jets background a Madgraph+Pythia8 sample is used to determine the generator systematic. The fragmentation and hadronization model differ also between generators. To take this into account as an uncertainty, the nominal sample is compared to a Herwig++[43, 49] generated sample. Uncertainties in shower radiation are covered by special samples, in which the showering was artificially increased and dereased for $t\bar{t}$ and single t [16].

As the event simulation happens usually before the data taking, only an estimated pileup distribution can be used in these events. This is compensated by reweighting the events to match the pileup profile of the data measured later. Uncertainties arising from the difference in the pileup of simulated events and measured data are taken into account.

6.1.1 Parton Density Function uncertainties

PDFs are obtained and made available as a collection of the nominal and uncertainty PDFs. These are determinied by propagating the uncertainties of the inputs though the determination process. These alternative / uncertainty PDFs are used in this analysis to create individual event weights by looking at the parton kinematic chosen for each event and reweighting the probability according to the alternative PDFs. These weights are then used to create the systematic event distributions for each of the uncertainty PDFs. Due to limitations in the event generation and analysis chain, this process is not perfectly streamlined. The ideal location for the determination of the different weights would be in the hard-process generation. But in our case this weight determination could only be done after the object reconstruction. For $t\bar{t}$ samples, there was sufficient information to recalculate the informations in order to create the necessary weights. For the Sherpa W+jets sample, this was not possible. But to still get PDF uncertainties for the W+jets background, an MadGraph8 sample was chosen. In this sample, the PDF uncertainties could be evaluated. As both $t\bar{t}$ and W+jets used NNPDF3.0, they both have 30 PDF sets for their systematic uncertainty. Additionally, we use the nominal choice of the PDF in the systematic named PDF0, as in the $t\bar{t}$ case this contains the recalculated "nominal" PDF choice and for

W+jets this contains effectively the difference between Sherpa and Pythia8 as well as the recalculated "nominal" PDF. All other PDF systematics are always obtained relative to PDF0 to avoid double counting of the differences towards the nominal sample [53].

6.1.2 W+jets reweighting

In Section 7.2, figure 7.5 the preselection event distribution shows some discrepancy between the modeled and observed event yields. This discrepancy can be interpretet as systematic uncertainty. To include this uncertainty a p_T dependent reweighting factor for the W+jets at pre-selection level is obtained. This reweighting factor is then applied to an event by event basis to the W+jets events in the signal and control regions to create the yield estimates from this systematic. Figure 6.1 shows the mismodelling and correction in effect.

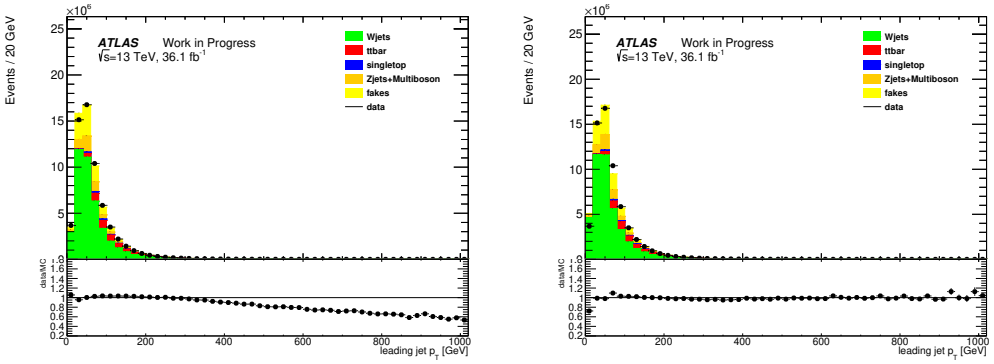

(a) Pre-reweight (b) Post-reweight

Figure 6.1: Effect of W+jets reweighting on the pre-selection leading small jet transverse momentum distribution.

6.1.3 W+jets AtlFast2

The W+jets samples contain so many events that it was unfeasable to produce them in full simulation. Therefore, they were produced with AtlFast2. A proper systematic handling of the effect of using AtlFast2 instead of the full simulation would need a huge number of fully simulated events, which defeats the purpose of using AtlFast2 in the first place. A flat 5% uncertainty is assigned.

6.2 Object systematic uncertainties

In addition to the uncertainties from the simulation of the production of particles, we also have uncertainties for the conversion of detector responses to reconstructed objects. This is particularly relevant as we base the analysis and discriminating variables on these higher-level reconstructed objects and most notably their energy or momenta. Therefore, the calibration and resolution needs to be taken into account.

6.2.1 Electron

A full description of all the different effects contributing to the scale of the electron energy, contains more than 70 independent parameters [6]. In order to make the systematics more manageable, a combined energy scale variation is used, which was determined by quadratic summation. For the energy resolution, the picture is quite similar. A big number of independent parameters describing all the known sources of electron energy resolution uncertainty are quadratically summed to create a single combined energy resolution systematic. This results in two quite conservative systematics [19].

There are four additional systematic uncertainties associated with electrons. They originate from the scale factors we have to apply to simulated events in order to match the triggering, reconstruction, identification and isolation to the efficiencies observed in data. As these scale factors were determined by comparing simulated events with measured data and are essentially just ratios, they come with an uncertainty [41].

6.2.2 Muon

As with the electron, the muon uncertainties are also comprised of a momentum scale and a resolution component. But as muons are reconstruced in both the inner detector and the muon spectrometer, the resolution uncertainty is treated independently for these two detector components. The momentum scale uncertainty used is a combination of several contributions [28].

Also there are additional systematic uncertainties arising from the scale factors between simulated events and measured data. Like with the electrons, these scale factors are applied to correct the description of trigger, identification and isolation efficiencies. But unlike for electrons, the muon scale factor systematics are available separated into systematic and statistical components.

6.2.3 Fake leptons

Fake leptons are introduced in section 5.1.3 as a background estimate of non-prompt leptons. But the method of obtaining them is relatively crude and the background turns out to be quite small in this analysis. Thus we go a simple route and assume 100% systematic uncertainty on the fake yield. But the fake estimate is also quite phase space dependend. So we also include a systematic based on the lepton p_T in the event. The shape for this uncertainty is determined by taking the ratio of the lepton p_T distribution of observed and expected events at preselection level and ignore the scale, as this would be double counting with the 100% flat uncertainty.

6.2.4 Jets

The jet energy scale calibration relies heavily on comparing the measured and simulated events of well understood processes. Therefore, more than 60 different uncertainty sources contribute to the calibration uncertainty. In order to efficiently utilize these systematic uncertainties, they are combined together. To still get a good description of the jet energy scale uncertainty, the merged set of 19 systemtics is used [4]. This is not as an aggressive reduction as for the electrons and muons, but jet kinematics are quite relevant for the analysis. Especially with the aim of combining several $R = 0.4$ jets into bigger jets, the choice of the reduction to 19 parameters seems to be a good compromise between accuracy and computing time. In addition to the energy scale, also the energy resolution has a systematic uncertainty to cover the imperfection in simulated energy deposits. In cases where the jet vertex tagging is used, also an uncertainty on this is taken into account in order to cover imperfections in the simulated events.

6.2.4.1 *b*-jets

For *b*-tagging, jets get additional systematic uncertainties associated with the efficiency calibration of the *b*-tagging algorithm. Especially the *b*-tag efficiency uncertainty as well as the mis-tag efficiency uncertainty of *c*- and light-jets are propaged into the analysis [21, 9].

6.2.5 Missing transverse momentum

Most contribution to the missing transverse momemtum comes from reconstructed objects like electrons, photons, muons, and jets. Therefore, any energy or momentum uncertainty on these higher-level objects translates directly into an uncertainty of the calculated missing transverse momentum. But as these uncertainties are already covered by the corresponding object

systemtics, only the uncertainties on the soft term of missing transverse momentum contributors is unaccounted for by other systematics. The uncertainty on the soft term is determined in events of $Z \to \mu\mu$ by comparing the hard term, so the sum of transverse momenta of the reconstruced objects, with the soft term. Systematic uncertainties are then extracted in two components of the soft term: parallel and perpendicular to the momentum direction of the hard term. This is done, because the scale offsets affect primarily the component longitidinal to the hard term momentum direction, whereas the resolution affects both components [3].

Chapter 7

Path to a selection strategy

We have to understand the most efficient selection for our signal while selecting as little background as possible.

In a first step, we have to understand where the limitations of the signal sample description are. This is done in section 7.1. Afterwards, in section 7.2, we find a set of potential variables with good discrimination power between signal and background events. The goal here is to use a small number of variables with simple cuts, resulting in efficient separation of signal and background events.

7.1 Studies of different production conditions

To make sure we understand the signal we produce, we look at different options for the production. Pythia8 gives us events with all particles and decay products in the final state, just before they interact with the detector. These particles can be used to create objects of jets, electrons, muons and E_T^{miss} like we can do from tracks and energy deposits from the detector simulation or real data. So we can get kinematic distribution for these objects. But we don't run the simulation of the interaction of the particles with a detector, so this approach only requires a fraction of the comuputing time. This allows for studies of different MadGraph settings.

Most parameters of the sample production were already defined by an earlier analysis looking at the same signal, e.g. [29]. But we still want to make sure we understand the implications of choosing the 5-flavor production scheme and validate that it is still sufficient to produce only one chirality and apply the finding to all combinations. In the end, we want to probe higher masses and have a higher proton collision energy.

Figure 7.1 shows the distributions of b^* mass and p_T for different production settings. The width of the mass distribution is just the width we put in MadGraph. The ratio between the samples produced in 4-flavor and 5-flavor

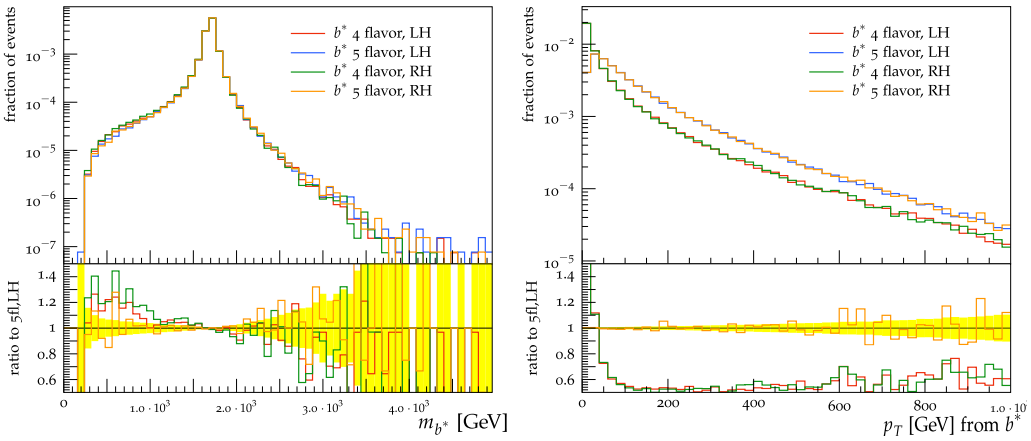

Figure 7.1: Mass and p_T of the produced b^* with the different choices of 4- or 5-flavor scheme and left-handed (LH) or right-handed (RH) b^* chirality. [2]

scheme has a slight slope with a somewhat higher fraction of events at low masses for 4-flavor production. The p_T distribution gives a hint to why we see this slope in the mass distribution ratio. In the 5-flavor scheme, the b quark starts with a $p_T = 0$, where as in the 4-flavor scheme the b quark is produced by a gluon splitting into a $b\bar{b}$ pair, where each quark gets a transverse momentum. This additional momentum also means that the 4- and 5-flavor production use a slightly different portion of the PDF. And even though Pythia8 tries to compensate the $p_T = 0$ for the 5-flavor production, it is not sufficient to put the 4-flavor and 5-flavor production exactly on top of each other. The different momentum fractions in the PDF result then also in a small difference in the mass distribution, as the probabilities of the different masses shift a little bit.

This difference in b^* p_T translates into the decay products of the b^* as well. But the effect on objects like the leading jets in figure 7.2 is already quite small, due to the high mass of the b^* compared to the $\sim 50\,\text{GeV}$ shift in the b^* p_T spectrum. The jets shown in this figure are obtained with two different cone sizes (R) in the jet algorithm. A bigger $R = 1.0$ jet is more likely to fully contain the hadronically decaying W, than the $R = 0.4$ jet. Therefore smaller fraction of events have small leading p_T when looking at the $R = 1.0$ jet collection, than when looking at the $R = 0.4$ jet collection. This is also visible in the jet mass for both jet collections in figure 7.3, where the $R = 1.0$ jets have more events at masses compatible with the W mass or even the t mass than the $R = 0.4$ jets.

The difference from the 4-flavor vs. 5-flavor b^* p_T distribution in figure 7.4 is mainly visible in the slope at high p_T of the jets, see figure 7.2. As the

[2] The yellow band is statistical uncertainty from the limited number of generated events.

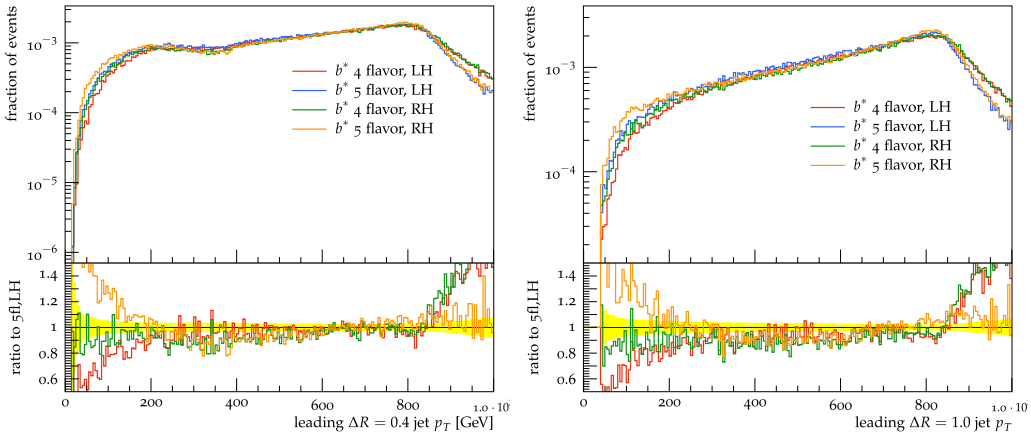

Figure 7.2: Leading $R = 0.4$ and $R = 1$ jet p_T with the different choices of 4- or 5-flavor scheme and LH or RH chirality.

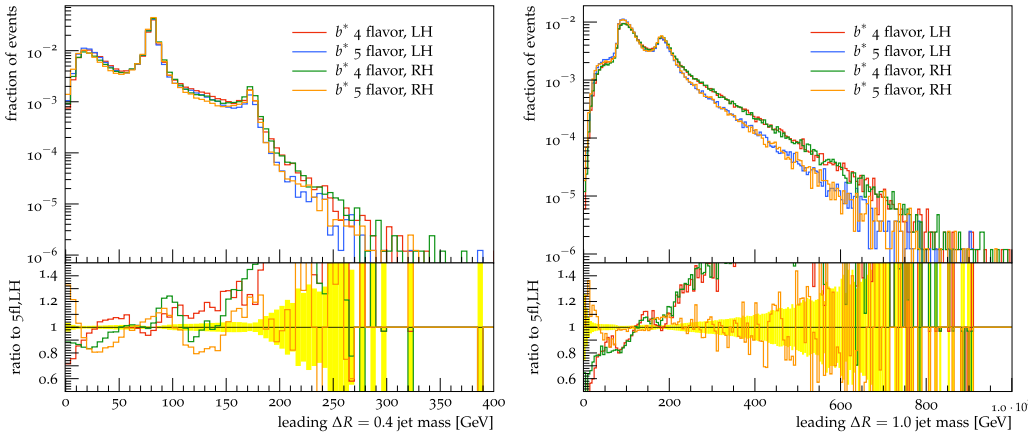

Figure 7.3: Leading $R = 0.4$ and $R = 1$ jet mass with the different choices of 4- or 5-flavor scheme and LH or RH chirality.

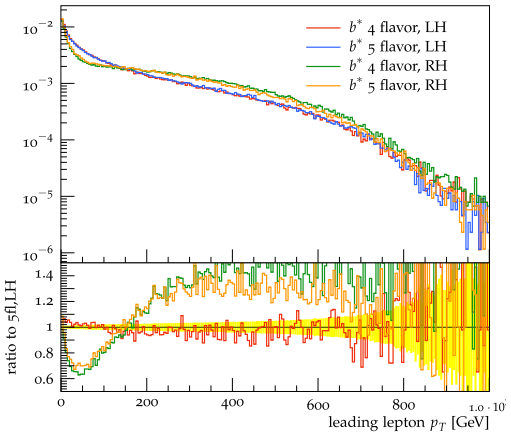

Figure 7.4: Leading lepton p_T with the different choices of 4- or 5-flavor scheme and LH or RH chirality.

slope is relatively steep compared to the bulk of the spectrum, only a very small number of events are actually sensitive to this effect.

Also the leptons seem to be insensitive to the choice of a 4- or 5-flavour production scheme. But the chirality does show an effect, where the left handed b^* creates a higher fraction of low transverse-momentum leptons. But in either case most of the leptons have low transverse momenta and just the tail extends into the very high transverse momenta. As a result, we should not cut to strongly into the lepton p_T spectrum to keep most of our signal events.

7.2 Cutflow optimization

7.2.1 Preselection

We plan to build an analysis which targets a single-lepton final state. There are recommendations from performance groups in ATLAS for these kind of anlyses. These can be considered standard cuts, as they are used by many different exotic particle searches in ATLAS. The list of these preselection cuts is:

1. Pass of a Good Run List (GRL), which contains all time intervals in which all detector subsystems were operating nominally [63].

2. Pass of good calorimeter criteria. They require that neither the tile nor the liquid-argon calorimeter reported any problems. Additionaly the SCT is required to not report any problems and that the event was completly recorded.

3. A primary vertex is found, so a jet vertex fraction can be calculated and b-tagging algorithms can be used to identify b-jets.

4. The event was triggered by one of the six triggers described in section 5.1.

5. There is exactly one electron or muon with at least 28 GeV transverse momentum

6. Veto events with a "BadLoose" jet according to [5]

7. $E_T^{\text{miss}} > 20\,\text{GeV}$

8. $E_T^{\text{miss}} + m_T(l, E_T^{\text{miss}}) > 60\,\text{GeV}$

9. At least two small radius ($R = 0.4$) jets

We don't expect that these cuts reduce the sensitivity to the b^* signal unnecessarily. Thus they can just be applied to all events, which allows the usage of well understood "default" systematic uncertainties for all of the used objects. This way we don't need to determine all of these ourselves.

7.2.2 Scan for best $\frac{\text{signal}}{\sqrt{\text{background}}}$

So far we looked at the distributions of some kinematic variables based on Pythia8 output for the signal. The next step is the construction of an analysis which enhances the fraction of signal events by filtering out background events from the data.

The initial plan was to follow the earlier analysis [29]. But as the new analysis uses data with $\sqrt{s} = 13\,\text{TeV}$ collisions instead of $\sqrt{s} = 8\,\text{TeV}$ collisions and targets a higher mass b^*, it is not obvious that the old analysis strategy can be just copied. Instead the variables and cuts used in the old analysis are taken as suggestions for a matrix of possible cuts from which the most effective combination is chosen. The number of jets is one variable, which was used in the old analysis quite effectively, but does not seem to work any more in this analysis. In the $\sqrt{s} = 8\,\text{TeV}$ analysis a requirement of two or three jets was imposed on the events for the signal selection. Due to the high mass of the b^* and compared to the low p_T of the b^*, the W and the t from the decay have a big angular distance. By having a single lepton analysis, either the W directly from the b^* or the W from the t had to decay into a lepton and neutrino and the other into two jets. With the b-jet from the t decay, three jets are expected. But as the W bosons have quite high momenta, it is possible that jets merge, therefore two jets were also allowed. But for the $\sqrt{s} = 13\,\text{TeV}$ analysis we can see in figure 7.5, the main content of the signal is not only in the two jet and three jet bins, but rather extends

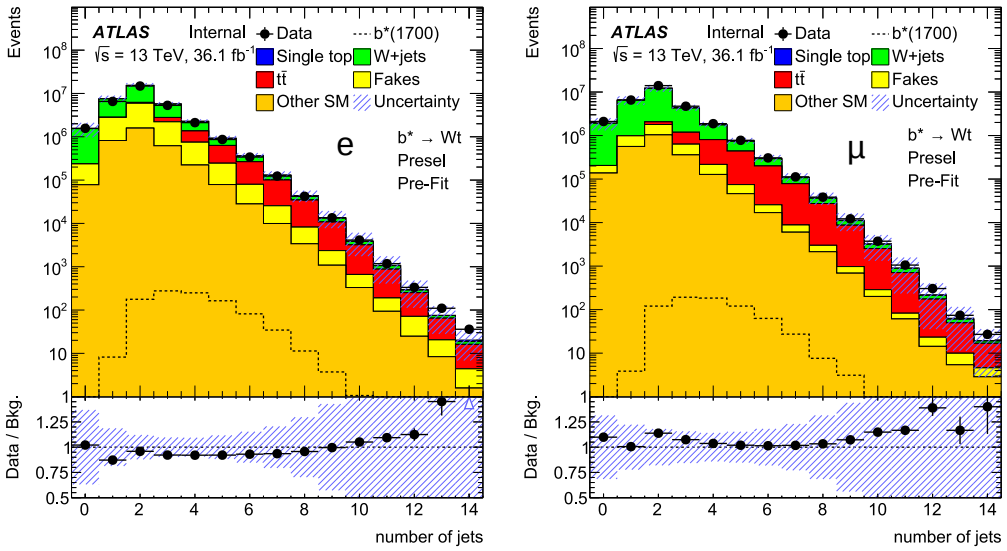

Figure 7.5: Number of $R = 0.4$ jets after preselection cuts defind in subsection 7.2.1. The one lepton selected in the events is either an electron (left) and a muon (right). The expected contribution of a exemplatory 1.7 TeV b^* is drawn in for comparison. The hashed blue uncertainty is the combination of the statistical and systematic uncertainty.

significantly into four jet and five jet bins where also the background is lower. This is most likely the result of the higher energy in the collision resulting in more radiation being above the threshold of forming valid jets. With these additional jets we also loose the possibility to easily use angular distances between the jets and between jet and lepton.

But even though we lost the option to easily boost our signal to background ratio by using cuts on angular distances, we got the new opportunities by exploiting the higher target mass of the b^*. As the $\sqrt{s} = 8\,\text{TeV}$ analysis obtained an observed limit of $m_{b^*} > 1.5\,\text{TeV}$ and had an expected limit of $m_{b^*} > 1.66\,\text{TeV}$ for the b^* mass, we can target this new analysis to masses $m_{b^*} \simeq 1.7\,\text{TeV}$.

In order to build the analysis we have to first evaluate different variables for their effectiveness in separating signal from background. This becomes particularly interesting in cases where the separation power is dependent on the combinatorics of different variables. To address also these correlations, a multitude of combinations of different cuts on many variables were tested systematically. The discriminating variable to evaluate the effectiveness of a certain set of cuts is $\frac{\text{signal}}{\sqrt{\text{background}}}$ $\left(\frac{S}{\sqrt{B}}\right)$. This does not take any systematic uncertainties into account and thus is a relatively crude method. But it allows for fast processing of a huge number of possibilities.

The variables tested for their effectiveness in separating signal from background are:

- number of $R = 0.4$ (small-radius) jets
- number of b-tagged small-radius jets
- mass of the leading (in p_T) $R = 1.0$ (large-radius) jet
- p_T of the leading large-radius jet
- difference in azimuthal angle between the leading large-radius jet and the lepton: $\Delta\phi(j_{R=1.0}, l)$
- maximum distance between the lepton and any small-radius jet: $\max(\Delta R(j_{R=0.4}, l))$[3]
- maximum distance between the leading large-radius jet and any small-radius jet: $\max(\Delta R(j_{R=0.4}, \text{lead}(j_{R=1.0}))$
- missing transverse momentum E_T^{miss}
- scalar sum of all transverse momenta: $H_T = p_{T,l} + E_T^{\text{miss}} + \sum p_{T,j_{R=0.4}}$

For these variables, lower and upper bounds where tested with possible cuts covering reasonable ranges for each variable. With the inclusion of all variables used in the $\sqrt{s} = 8\,\text{TeV}$ selection, this analysis could be found again if it still provides a reasonably optimal selection strategy. But it is also possible, that any number of variables is ignored.

The best performing combinations are

1. less than six small-radius jets
2. at least one b-tagged small-radius jet
3. a minimum mass of the large-radius jet of $m_{j_{R=1.0}} > 70\,\text{GeV}$
4. a minimum transverse momentum of the large-radius jet of $p_{T,j_{R=1.0}} > 700\,\text{GeV}$

and

1. at least one b-tagged jet
2. a minimum mass of the large-radius jet of $m_{j_{R=1.0}} > 70\,\text{GeV}$

[3] $\Delta R = \sqrt{(\Delta\phi)^2 + (\Delta\eta)^2}$ is a nearly lorentz invariant measure of distance. Actual lorentz invarianz is only given for massless particles, but for $p_z c \gg mc^2$ it is a good approximation.

3. a minimum transverse momentum of the large-radius jet of $p_{T,j_{R=1.0}} > 550\,\text{GeV}$
4. a minimum missing transverse momentum $E_T^{\text{miss}} > 200\,\text{GeV}$

As these two sets of cuts are both reasonably efficient in terms of $\frac{S}{\sqrt{B}}$ they should be better compared and refined with proper limit setting, which also takes systematic uncertainties into account. But to aid the process of getting to limit setting with proper systematic uncertainties we choose an intermediate definition of signal region. This is relatively easily possible as these two sets are also quite close. As these set of cuts are only teated as suggestion, we loosen them again a little before the final set of cuts is beeing determined. So until the final signal region is defined, we work with the intermediate definition of:

1. at least one b-tagged jet
2. a minimum mass of the large-radius jet of $m_{j_{R=1.0}} > 70\,\text{GeV}$
3. a minimum transverse momentum of the large-radius jet of $p_{T,j_{R=1.0}} > 400\,\text{GeV}$.
4. a minimum missing transverse momentum $E_T^{\text{miss}} > 100\,\text{GeV}$ to get above the triangle cut of $E_T^{\text{miss}} + m_T(l, E_T^{\text{miss}})$ in the preselection

7.2.3 Variable for shape fit

This analysis employs a template fitting in order to increase the sensitivity to the signal compared to a cut-and-count based analysis. Thus we need to find a variable which shows different shapes for signal and backgrounds. The natural choice here is a variable which is sensitive to the high-energy content in our signal events. A possible shape discriminant is the sum of all transverse momenta, H_T. Another option is to try to reconstruct the mass of our b^* particle. For this we utilize the knowledge, that our b^* decays effectively into two W bosons and a b quark. We also know that one of the two W bosons decays into the lepton and the neutrino. This is the only source of neutrinos in our signal events, therefore, the neutrino can be fully reconstruced using the E_T^{miss} and the knowledge that it came from the W and we know the 4-vector of the charged lepton. The other W and the b are slighly more ambiguous. There are now two options as shown in figure 4.1.

1. Both the hadronically decaying W and the b are coming from the t-quark
2. The b comes from the t quark and the hadronically decaying W from the b^* directly.

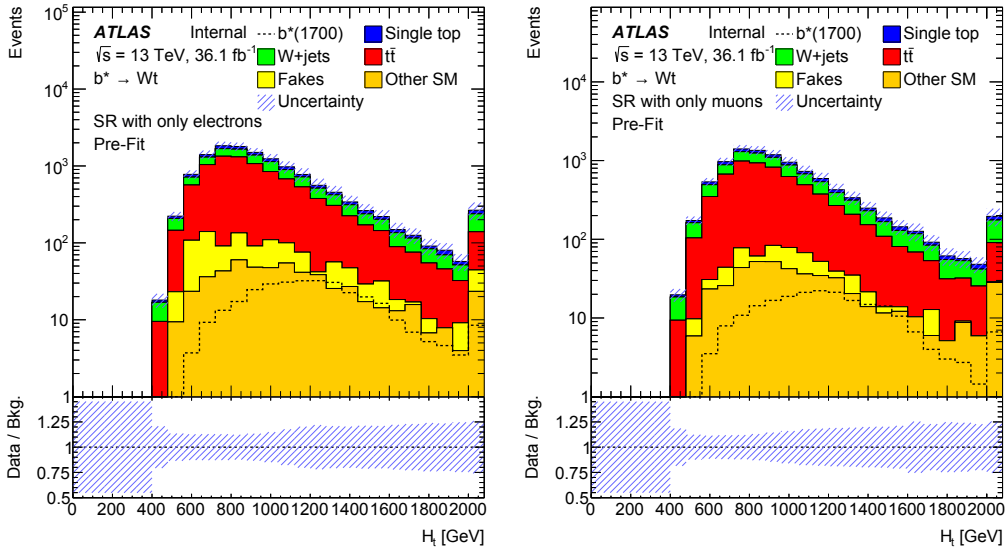

Figure 7.6: H_T distribution for the electron and muon signal region events as defined at the end of subsection 7.2.2. H_T is the scalar sum of transverse momentum of lepton and jets. It correlates quite well with overall energy transfer in the hard collision. The uncertainty contains the systematic and statistical uncertainty and the Data / Bkg ratio plot shows the uncertainty band in which the data would be expected.

In the first case, the W and b are usually so close together, that the b is contained in the large-radius jet. In the second case the b-jet and the large-radius jet are far apart and thus we would need to take both into account.

7.2.3.1 Neutrino reconstruction

For the neutrino momentum, only the two components transverse to the beam axis can be measured indirectly. If there is only one neutrino, like in our signal sample, the full neutrino momentum vector is obtained by setting the lepton-neutrino system invariant mass to the W boson mass. This results in a quadratic equation which is solved for the z-component of the neutrino momentum. The smallest real solution is used.

7.2.3.2 Shape comparison of different variables

Figures 7.6 to 7.10 show the intermediate signal region selection defined in section 7.2.2, with a large-radius jet $p_T > 400\,\text{GeV}$ for several variables. The simplest variable is the scalar sum of lepton and jet transverse momenta, H_T in figure 7.6. Several approaches to reconstruct the mass of the b^* are shown

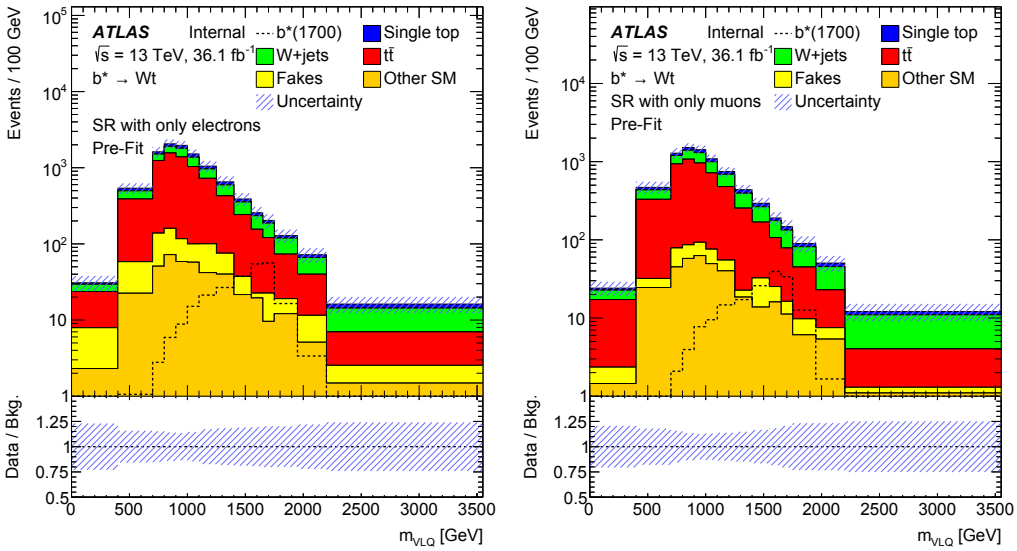

Figure 7.7: Invariant mass distribution for the electron and muon signal region events as defined at the end of subsection 7.2.2. The invariant mass $m_{\mathrm{VLQ}} = \sqrt{||P_l + P_\nu + P_{1^{\mathrm{st}}\mathrm{largejet}}||^2}$ in these plots is calculated from the charged lepton, neutrino and the leading large-radius jet. This mass should reconstruct most of the original b^*.

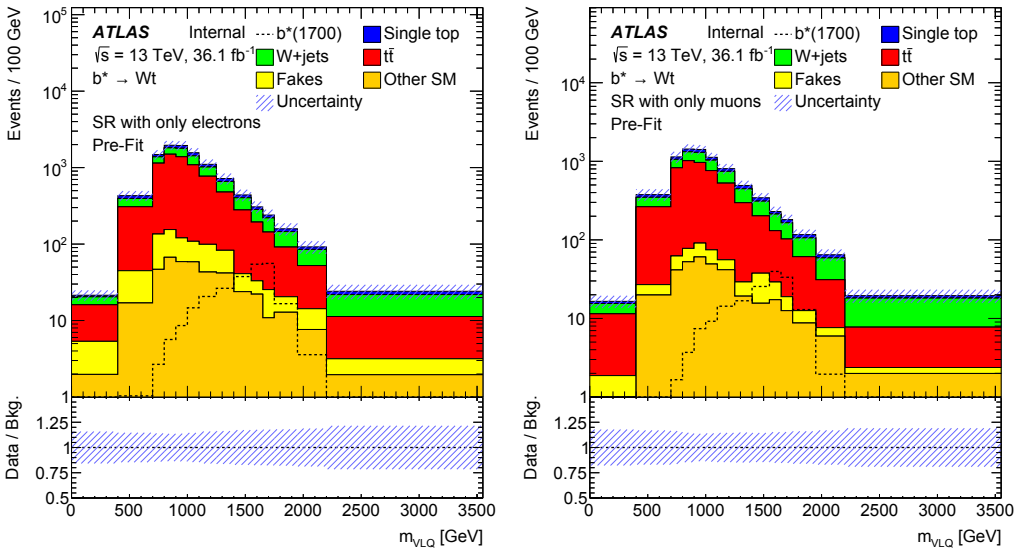

Figure 7.8: Invariant mass distribution for the electron and muon signal region events as defined at the end of subsection 7.2.2. The invariant mass $m_{\mathrm{VLQ}} = \sqrt{||P_l + P_\nu + P_{b-\mathrm{jet}} + P_{1^{\mathrm{st}}\mathrm{largejet}}||^2}$ in these plots is calculated from the charged lepton, neutrino, b-jet and the leading large-radius jet. This mass should reconstruct all decay products of the original b^*.

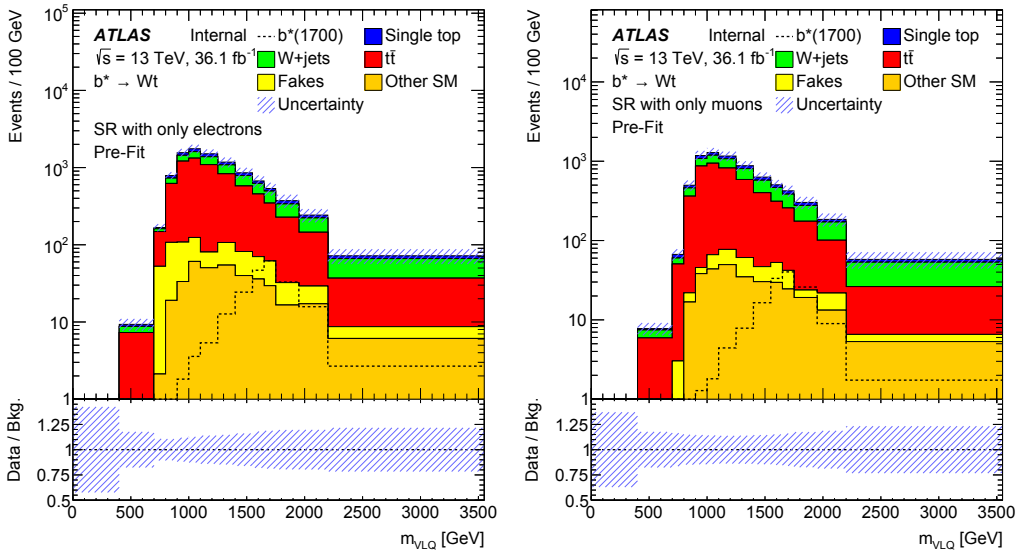

Figure 7.9: Invariant mass distribution for the electron and muon signal region events as defined at the end of subsection 7.2.2. The invariant mass $m_{\mathrm{VLQ}} = \sqrt{||P_l + P_\nu + P_{1^{\mathrm{st}}\mathrm{largejet}} + P_{2^{\mathrm{nd}}\mathrm{largejet}}||^2}$ in these plots is calculated from the charged lepton, neutrino and the leading two large-radius jets. This mass should reconstruct all decay products of the original b^*.

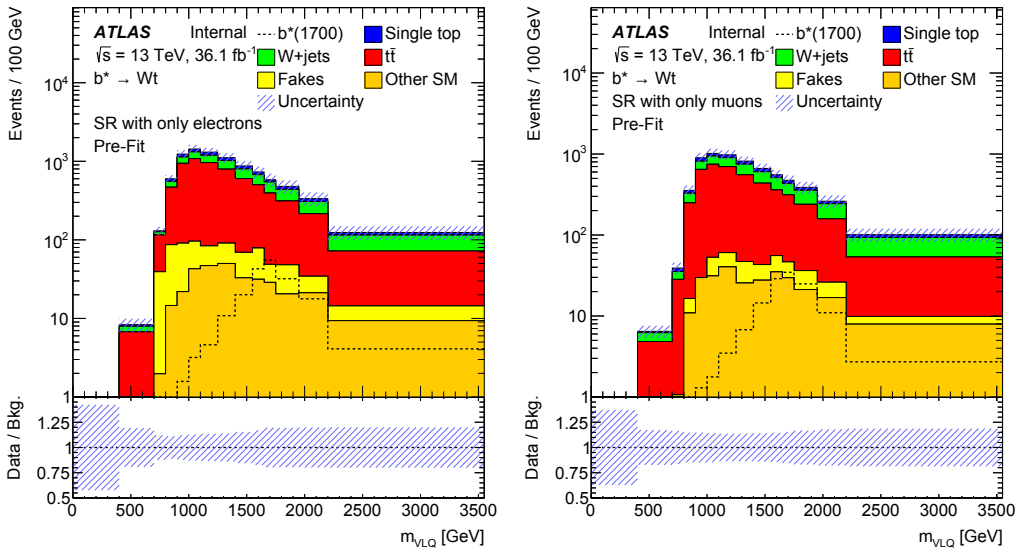

Figure 7.10: Invariant mass distribution for the electron and muon signal region events as defined at the end of subsection 7.2.2. The invariant mass $m_{\mathrm{VLQ}} = \sqrt{||P_l + P_\nu + P_{b-\mathrm{jet}} + \sum P_{\mathrm{largejet}}||^2}$ in these plots is calculated from the charged lepton, neutrino and all the large-radius jets. This mass should reconstruct all decay products of the original b^*.

in figures 7.7 to 7.10. For these the four-momentum-vectors of the decay products of the assumed b^* decay are added up. The interesting question here is: Which particles do we need to add to this mass calculation in order to get a handle on the b^* but to not add particles which didn't come from the direct b^* decay chain but rather from other initial particles?

To find a good choice of particles to be added in the mass calculation, several options are tried. A simple and quite conservative approch is tested in figure 7.7, by only using leading p_T large-radius jet, the lepton and the neutrino. This choice only contains all decay products if the large-radius jet contains the hadronically decaying W as well as the b-jet from the t decay. In order to cover events where the b-jet is not close enough to the hadronically decaying W and thus does not end up in the large-radius jet, an invariant mass is calculated from the leading p_T large-radius jet (j_{RC}), the charged lepton and the neutrino and the b-jet (j_b) is added to the sum of 4-vectors if the $\Delta R(j_b, j_{RC}) > 1$ in figure 7.8. An alternative approach to also capture the b-jet is followed in figure 7.9, where the invariant mass is calculated from the two leading p_T large-radius jets, the lepton and the neutrino. Here the assumption is, that due to the high mass of the b^*, also the b-jet alone would contain enough momentum in order to satisfy the criteria for large-radius jets. And lastly, 7.10 contains the invariant mass of the four-momentum-vector sum of all large-radius jets, the lepton and the neutrino.

The deciding factor between these four options is now the suitability for a profile likelihood fit. An important feature for this is the ability to produce different shapes for signal an background. For the signal, this is achieved by obtaining a narrow peak, while the background is as homogeneous as possible. Looking now at the plots for the mass peak, we see that the H_t performs worst according to these requriements. The invariant masses look rather similar, but figures 7.9 and 7.10 have a slightly broader distribution than figures 7.7 and 7.8 for the b^* sample. Therefore, the most promising variable for a discriminant is the invariant mass calculated from the large-radius jet, the lepton and the neutrino. The addition of the b-jet in case of $\Delta R(j_b, j_{RC}) > 1$ shows a little bit worse signal to background ratio. But the addition of the b-jet or not, does not change the shape significantly. Therefore the final decision if the b-jets should be included or not based on the expected limit later.

7.2.3.3 Comparison of different signal regions

As described in section 7.2.2, two different options are favoured by just looking at $\frac{S}{\sqrt{B}}$. The main difference between the two options is the minimum E_T^{miss} of either just the preselection or 200 GeV and minimum $p_{T,j_{R=1.0}}$ of either 550 GeV or 700 GeV. The results of these two options are shown in figures 7.11 and 7.12 using as discriminating variable the mass consisting out of the

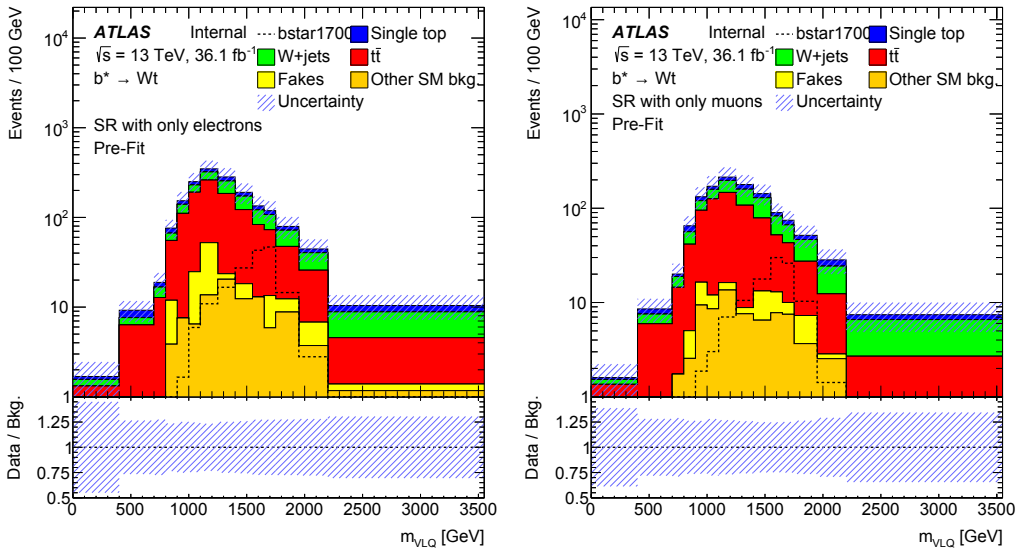

.

Figure 7.11: Invariant mass distribution for the electron and muon signal region events. The invariant mass in these plots is calculated from the charged lepton, neutrino and the leading large-radius jet. This mass should reconstruct most of the original b^*. The signal region chosen in this plot requires a minimum transverse momentum of the large-radius jet of $p_{T,j_{R=1.0}} > 550\,\text{GeV}$ and a missing transverse momentum $E_T^{\text{miss}} > 200\,\text{GeV}$.

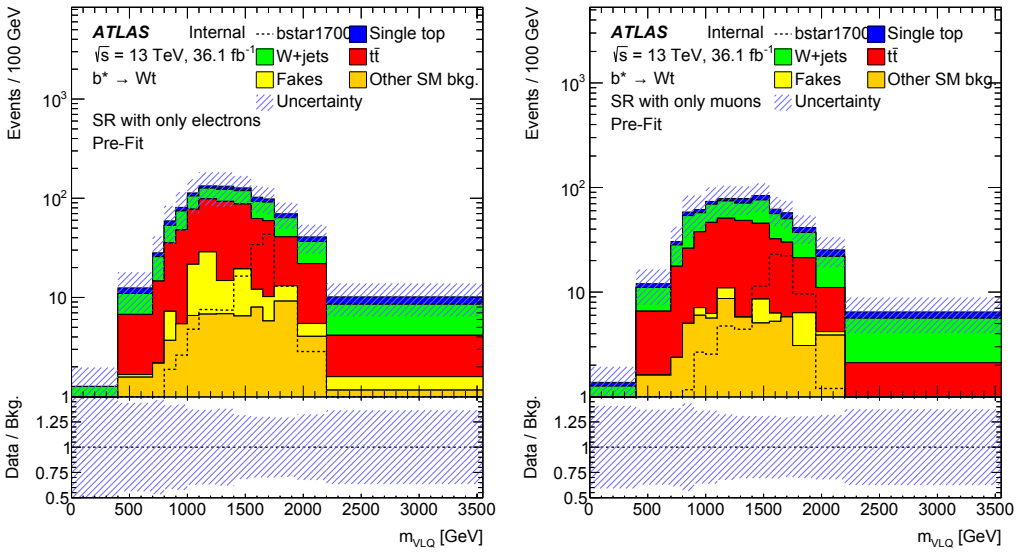

Figure 7.12: Invariant mass distribution for the electron and muon signal region events. The invariant mass in these plots is calculated from the charged lepton, neutrino and the leading large-radius jet. This mass should reconstruct most of the original b^*. The signal region chosen in this plot requires a transverse momentum of the large-radius jet of $p_{T,j_{R=1.0}} > 700\,\text{GeV}$.

lepton, neutrino and the leading large-radius jet as in figure 7.7. For both regions, we see drastically reduced statistics compared to the one used in figure 7.7. For low masses this would be expected just due to the higher p_T cut. But also in the region of a potential 1.7 TeV signal is affected. Due to the small statistics, the uncertainties in each bin are relatively high. To keep statistics high, we stick with the preliminary definition of the signal region with a cut on $E_T^{\text{miss}} > 100\,\text{GeV}$ together with a cut on the transverse momentum of the large-radius jet of $p_{T,j_{R=1.0}} > 400\,\text{GeV}$.

7.2.4 Determining control and validation regions

After having a signal region defined, we can move on and derive from this control regions. They are necessary to match the background estimate to the measurement without interference of the potential signal. But the control regions still need to be kinematically close to the signal region. Ideally we have a control region for each major background, which is primarily populated by this background.

Looking at the signal region candidate found by the optimization, it is clear that our primary backgrounds are $t\bar{t}$ and W+jets. For both of them the bulk of the events are removed by the cuts, primarily the high transverse-momentum

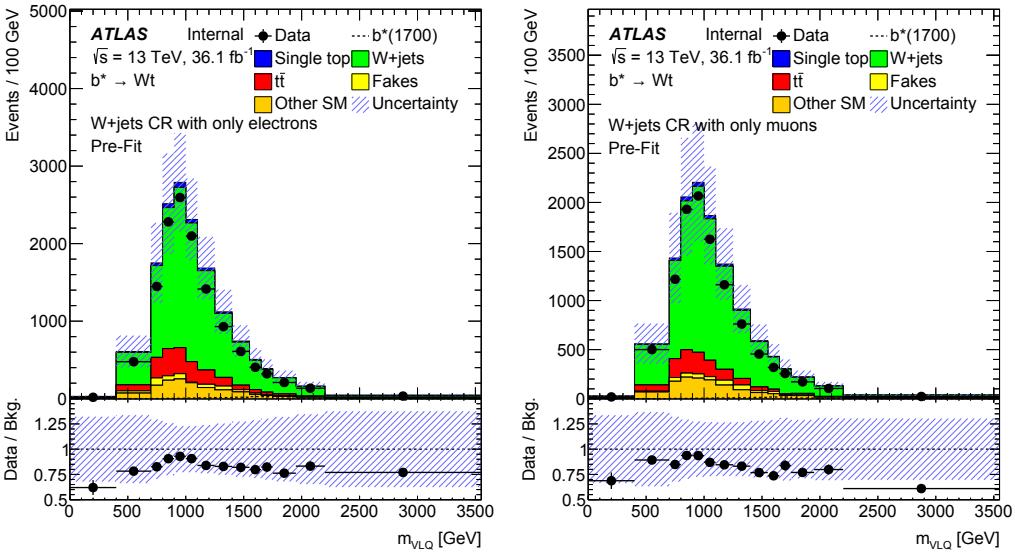

Figure 7.13: Invariant mass distribution for the electron and muon W+jets control region. The invariant mass in these plots is calculated from the charged lepton, neutrino and the leading large-radius jet.

cut on the large-radius jet.

7.2.4.1 W+jets control region

To get now to a control region for the W+jets samples, a simple inversion of the b-tagging requirement can be done. This keeps all the kinematic cuts in place and thus preserves a very similar phase-space as the signal region. But the requirement of exactly 0 b-jets effectively supresses signal and $t\bar{t}$ as both contain actual b quarks in the decay and the W+jets background becomes the biggest contribution, as can be seen in figure 7.13.

7.2.4.2 $t\bar{t}$ control region

For the $t\bar{t}$ background the situation is much more complicated. As outlined above the particle content is practically identical to that of the signal. And only the phase-space would be different. But as we cut strongly into the phase-space, the remaining events populate effectively the same phase-space as the signal. So the only way to get a $t\bar{t}$ enriched region is by touching the large-radius jet p_T cut. This is done in figure 7.14 by chosing $400\,\text{GeV} \leq p_{T,j_{R=1.0}} < 700\,\text{GeV}$. But this brings us two major problems.

1. We move away from the phase-space the signal region is covering. This reduces the power of such a region to convince us that we understand the $t\bar{t}$ background in the signal region.

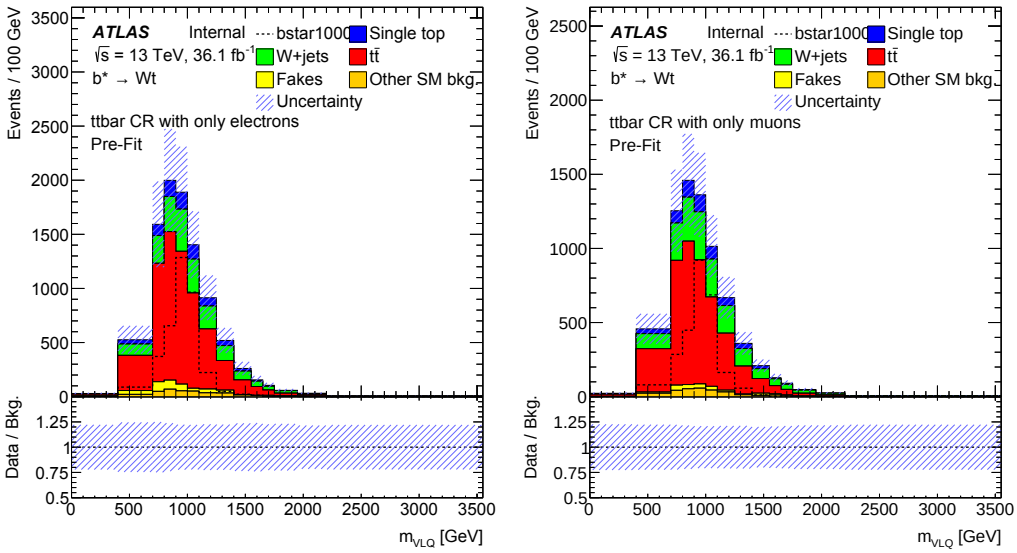

Figure 7.14: Invariant mass distribution for the potential electron and muon $t\bar{t}$ control region. The invariant mass in these plots is calculated from the charged lepton, neutrino and the leading large-radius jet.

2. The signal rejection is not very great, especially for smaller masses of b^*, so we would have to deal with quite a bit of signal contamination.

For these two reasons we decide not to use a dedicated $t\bar{t}$ control region. Instead we use a modified signal region to contain more phase-space and thus more $t\bar{t}$ events. This is done by setting the cut on the large-radius jet p_T to 400 GeV. Even though this now includes the same events, the potential control region would have contained, it gives us several advantages. With the decrease in large-radius jet transverse momentum we also get slightly more signal events. With the addition of lower large-radius jet p_T, lower reconstructed mass bins are populated. But as the events with the low p_T large-radius jet don't populate many high mass bins, the signal sensitivity is not much affected.

The low mass region of the signal region now covers mostly $t\bar{t}$ events with very minimal signal contamination, we can use this to evaluate $t\bar{t}$ background production. For this to work we will use a staged unblinding, where we first validate the W+jet agreement and then unblind the signal region in two steps allowing validation of $t\bar{t}$ aggreement before the signal containing part of the signal region is unblined.

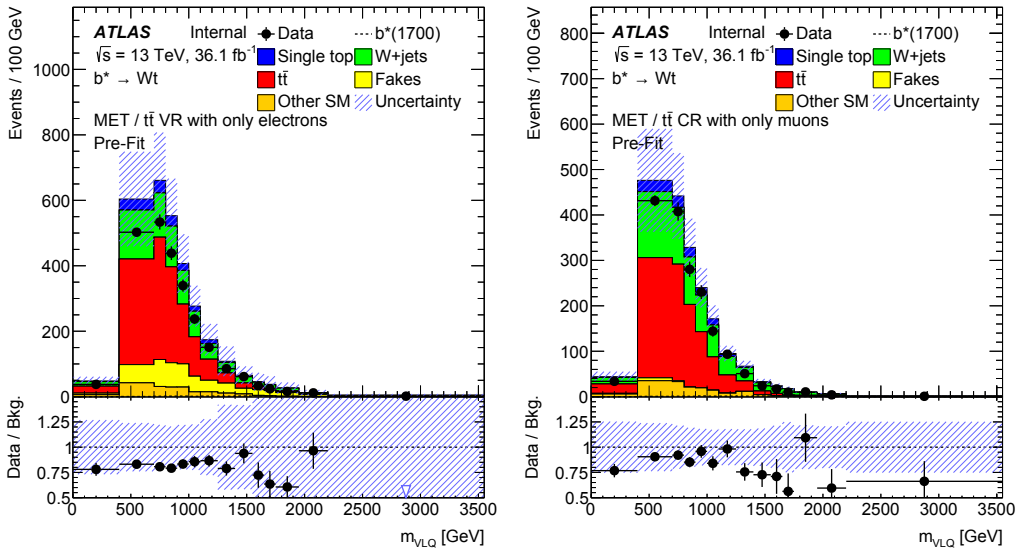

Figure 7.15: Invariant mass distribution for the electron and muon fake control region. The invariant mass in these plots is calculated from the charged lepton, neutrino and the leading large-radius jet.

7.2.4.3 Fake lepton control region

Even though the expected background from fake leptons is comparatively small, the determination of this background is particularly uncertain. Therefore, we are aiming for a dedicated control region for this kind of background. As the nature of the fake leptons is, that they do not originate from the W decay with a neutrino, the inbalance in the transverse momentum of the event is quite small. Thus we expect an enrichment of fake lepton events, when we concentrate the low E_T^{miss} events. We don't want to touch the preselection cuts. So the cuts on E_T^{miss} and $E_T^{\text{miss}} + M_T^W$ stay in place. But we create an upper cut: $E_T^{\text{miss}} < 100\,\text{GeV}$. As electron fakes and muon fakes are created by independent processes and features of the detector, it is natural to disentangle them by splitting this region into an electron-only and a muon-only case.

As seen in figure 7.15, the expected rate of muon fakes is much smaller than the rate of electron fakes. This is easy to understand as muon identification is much simpler with the muon detector outside of the calorimeter. As we reject muons with calorimeter energy deposits along the track, muons produced by decay products in jets are highly rejected. For electrons this is not as easy as both electrons and jets create tracks in the inner detector as well as deposit all their energy in the calorimeters. The main difference between jets and electrons is just the pattern of energy distribution and thus there is the chance of one being identified as the other.

The low fake rate of muons allows a secondary use of these low E_T^{miss}

regions. With the low fakes content, the dominant content in the low E_T^{miss} μ region is $t\bar{t}$ and thus we now even have something like a control region for $t\bar{t}$ background. For the electron case, the situation is not as simple. The fake estimate is much higher than for the μ case. But in combination with the very high uncertainty assigned to the fake estimate, the constraints cannot be very tight Thus this low E_T^{miss} e region is not very suitable for constraining $t\bar{t}$. A better use of this region is as a validation region. This way we only use it to see how the pull of the different backgrounds from the other control regions affect the agreement in this region.

7.2.4.4 Chosen cuts for signal, control and validation regions

With the lower p_T cut on the large-radius jets in the signal region, we choose the same p_T cut for the W+jets control regions and the low E_T^{miss} regions so the kinematic phase-space for all regions stays as similar as possible.

The low E_T^{miss} regions have a cut of $E_T^{\text{miss}} < 100\,\text{GeV}$ to increase the selection of fake events while rejecting signal event. To keep the signal region orthogonal to these low E_T^{miss} regions, a E_T^{miss} cut of $E_T^{\text{miss}} > 100\,\text{GeV}$ is used in the signal region definition. To keep the W+jets control regions close to the signal region, the same E_T^{miss} cut as in the signal region is applied. As it is beneficial for the low E_T^{miss} region to be split in electron and muons, the same split is implemented in the signal and the W-jets control region.

Table 7.1 summarizes the cutflow after the preselection cuts.

Cut variable	SR e	SR μ	W+jets CR e	W+jets CR μ	low E_T^{miss} VR e	low E_T^{miss} CR μ
# of e	1	0	1	0	1	0
# of μ	0	1	0	1	0	1
# of b-tagged jets	≥ 1		0		≥ 1	
E_T^{miss}[GeV]	> 100				$60 < E_T^{\text{miss}} < 100$	
p_T of $R = 1$ jet	$> 400\,\text{GeV}$					
mass of $R = 1$ jet	$> 70\,\text{GeV}$					

Table 7.1: Cut selection after optimization for the signal regions and the control regions.

Figures 7.16 to 7.18 show a selection of observables in the three different regions, split for electrons and muons. In order to follow a proper blinding strategy, the signal region plots don't contain the observed events, only simulated events. The control and validation regions contain the measured events, to be able to understand how well the description of the measurement already works, as all these regions are in a quite extreme phase-space. The agreement between observed data and expected number of events is not very good, but mostly within the systematic uncertainties. Also it looks like a

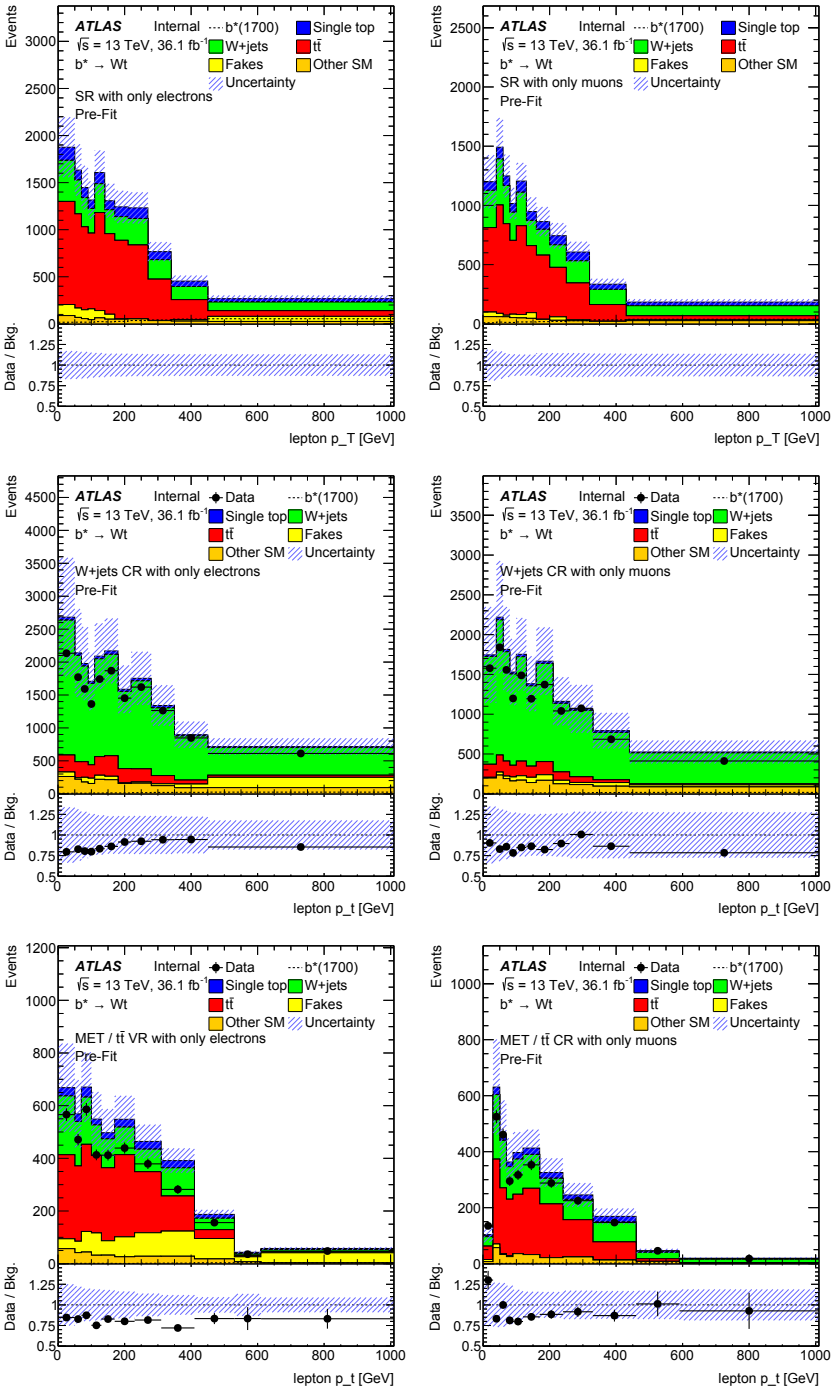

Figure 7.16: Lepton p_T distribution of the signal regions and all control regions.

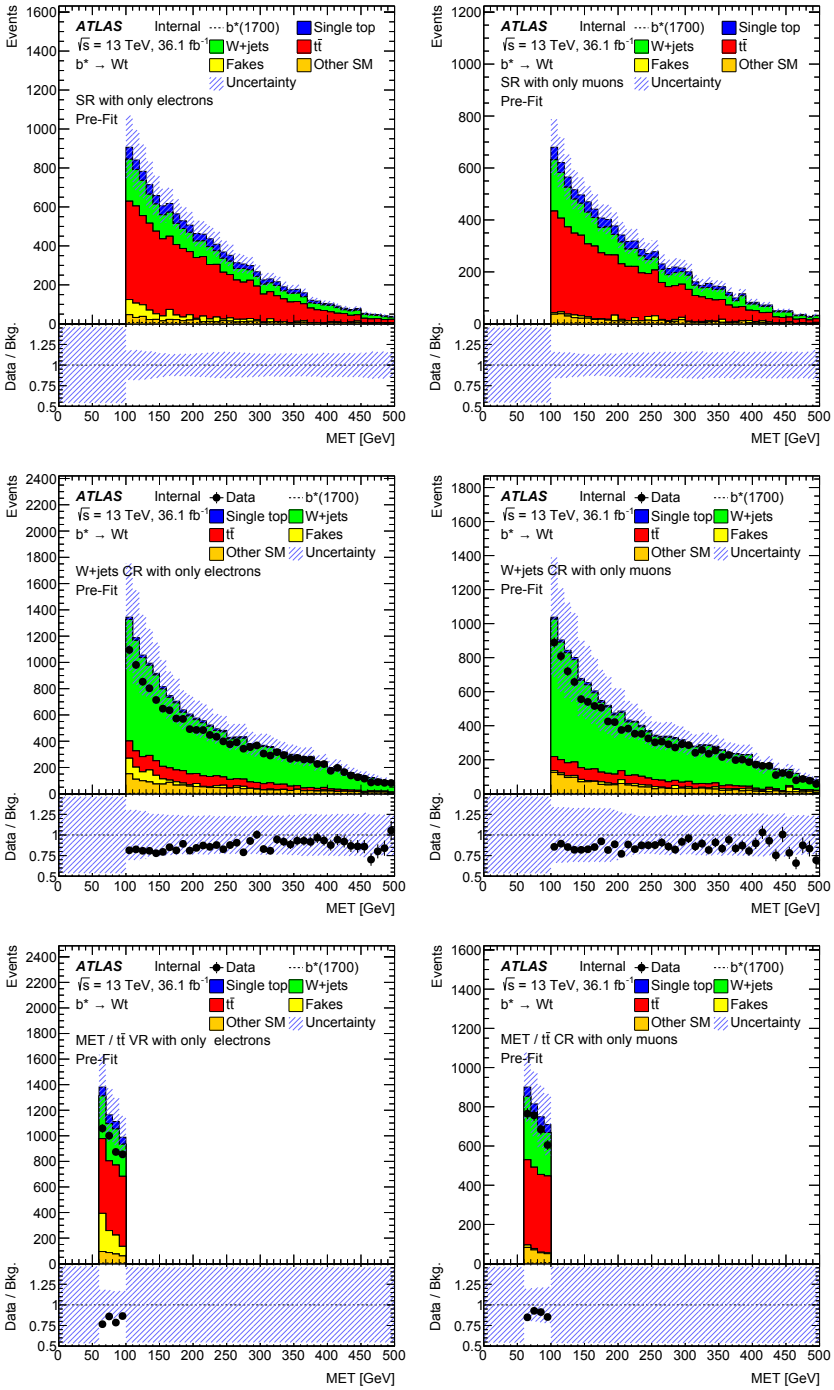

Figure 7.17: Missing transverse momentum E_T^{miss} distribution of the signal regions and all control regions.

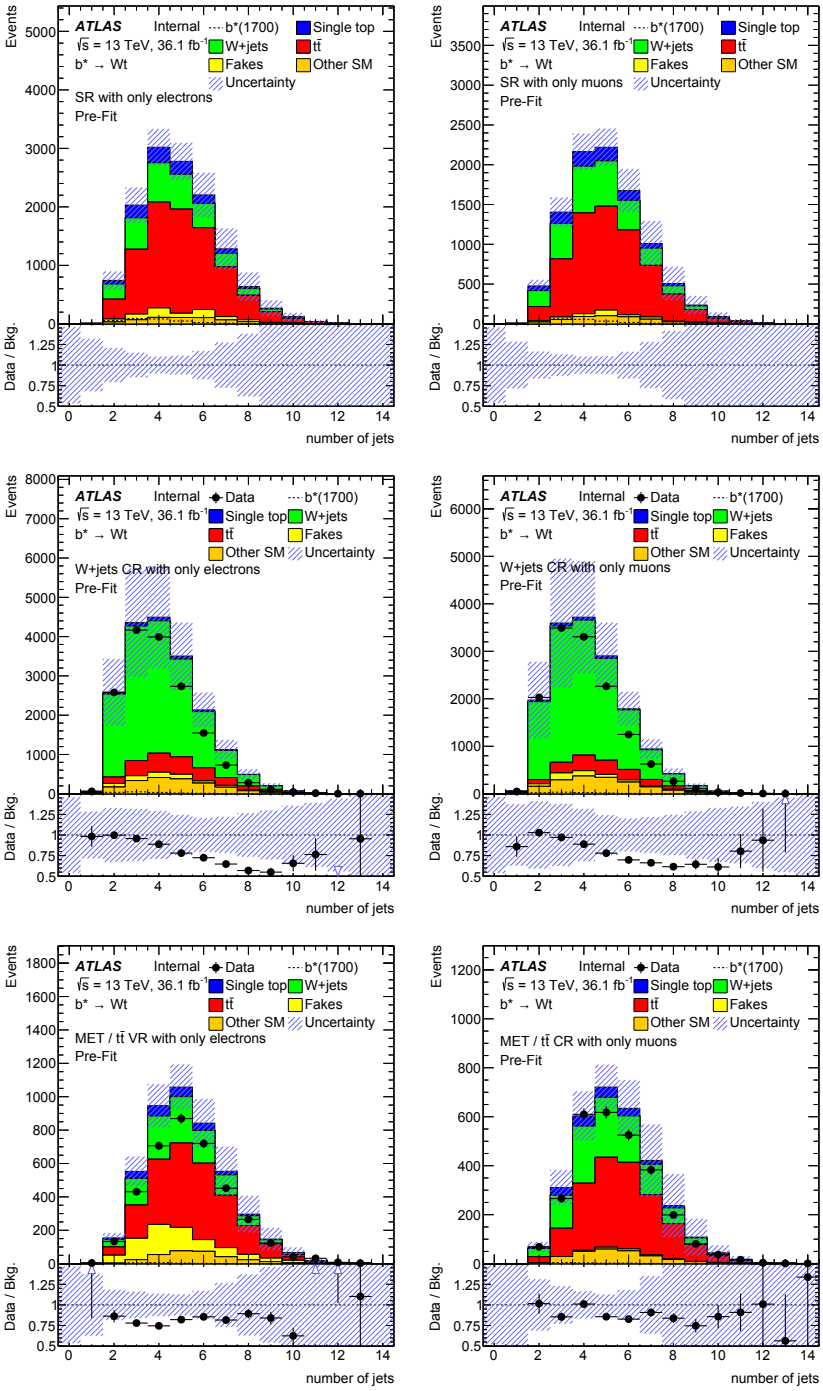

Figure 7.18: Number of jets distribution of the signal regions and all control regions.

normalization shift could correct for most of the discrepancy and being mostly within the systematic uncertainty suggests that the fit could improve the description of the measurement quite a lot.

The lepton p_T plots in figure 7.16 also show that a higher lepton p_T cut is not necessarily beneficial as the signal content is nearly flat across the whole range. We would assume that the content in the low-momentum region ends up in the low-invariant masses, which are keept intentionally to get a handle on the $t\bar{t}$ background.

Like for the lepton p_T, the signal does not show a pronounced peak in the missing transverse-momentum E_T^{miss} plot in figure 7.17. But at least the low momenta are less populated with signal events, which allowed us to generate the fakes control region. But these plots show especially that a much higher cut would also add more signal to this region.

The number of jets plots in figure 7.18, show that even though the signal sample peaks at three to four jets, the five jet bin still contains a significant amount and thus the number of jets is not a very effective discriminator anymore for the b^* signal compared to the $t\bar{t}$ background. This is the main reason we couldn't follow the two and three jet selection from the 8 TeV analysis.

Chapter 8

Statistical Analysis

In order to test for the presence of a signal, a binned maximum-likelihood fit to data is performed. For this, we take the bins of the discriminating variable, the reconstructed mass, from the signal and control regions. The binned likelihood function $\mathscr{L}(n, \theta^0|\mu, \theta)$ for a given distribution of event count n is constructed from the product of the Poisson propability terms of these bins n_i, with $\mu S(\theta)$ being the expected signal yield for a given set of nuisance parameters θ from the systematic uncertainties and $B(\theta)$ being the background expectation. As a penalty term for the systematic uncertainties a Gaussian with the central values of θ^0 is used.

$$\mathscr{L}(n, \theta^0|\mu, \theta) = \prod_{i \in \text{bins}} P(n_i|\mu S(\theta) + B(\theta)) \times \prod_{j \in \text{n.p.}} G(\theta_j^0|\theta_j) \qquad (8.1)$$

To measure now the signal strength μ, this likelihood needs to be maximized, or better the negative log-likelihood needs to be minimized. But this minimization does not only return μ, but θ, so we can get our binned distribution of expected events modified within the systematic uncertainties to better match the data. These improved expectations can be plotted again for visualization. By using only the events in the control regions, we can get the information which systematics are used to improve agreement and what level of agreement can be reached. As the measurement in the signal region is not used in this first step, small modifications to the analysis are still possible, without endagering the signal discovery process. For this to work though, it is important that the control regions don't contain significant amount of signal events. We also have chosen a validation region, which is not used in the fit, but modified to the expected events yields. This gives us additional confidence, that the description of the expected events actually gets better in describing the phase space, rather than just being pulled to match data with the huge number of degrees of freedom due to the large number of systematic uncertainies.

After the control region only fitting is understood, a new fit is performed, which also includes the signal regions. This then gives us the information whether the observation is compatible with the background hypothesis or whether adding the signal gives a better description of the measurement.

The final result will be something like a confidence level of the signal, or rather the exclusion of the signal. In order to cope with potential downward fluctuations of the background, the CL_s method is used [82]. $CL_s = \frac{CL_{s+b}}{CL_b}$ is the ratio of the confidence level of the signal + background hypothesis over the confidence level of the background only hypothesis. This gives a conservative limit on the signal hypothesis. Even though CL_s does not provide a proper confidence level, but rather a ratio, it can be used to set exclusion limits with certain confidence levels CL when

$$1 - CL_s \leq CL. \tag{8.2}$$

The power of the analysis is evaluated by the limits we can expect under background only conditions. This is calculated by running many limit setting calculations using pseudo-data, which is the background-only epxectation, varied according to the known uncertainties. By using a sufficiently high statistics, the 1σ (68%) and 2σ (95%) band of the expected limit are obtained.

8.1 Binned log-likelihood fit

The first step in the statistical analysis is the fit of expected background with and without the expected signals to the observed data. This serves two main purposes.

1. We improve the background description, by utilizing the freedom within the systematic uncertainties to better match the measured number of events. This improvement of the background description is only applicable to our specific phase-space.

2. When we include data in regions where we expect signal, the fit also returns the most compatible signal strength.

In order to follow a blinding strategy, the first fits only contain measured data in control regions. This is done to make sure that we can confidently say that the conclusions we draw from (dis)-agreement of expected background and data is not biased in either direction from the presence or non-presence of the signal.

In figure 8.1 we can see the result of the fitting of the control region expected event yields to the observed data. These plots need to be compared to figure 7.13 and figure 7.15, which show the equivalent plots before the fit.

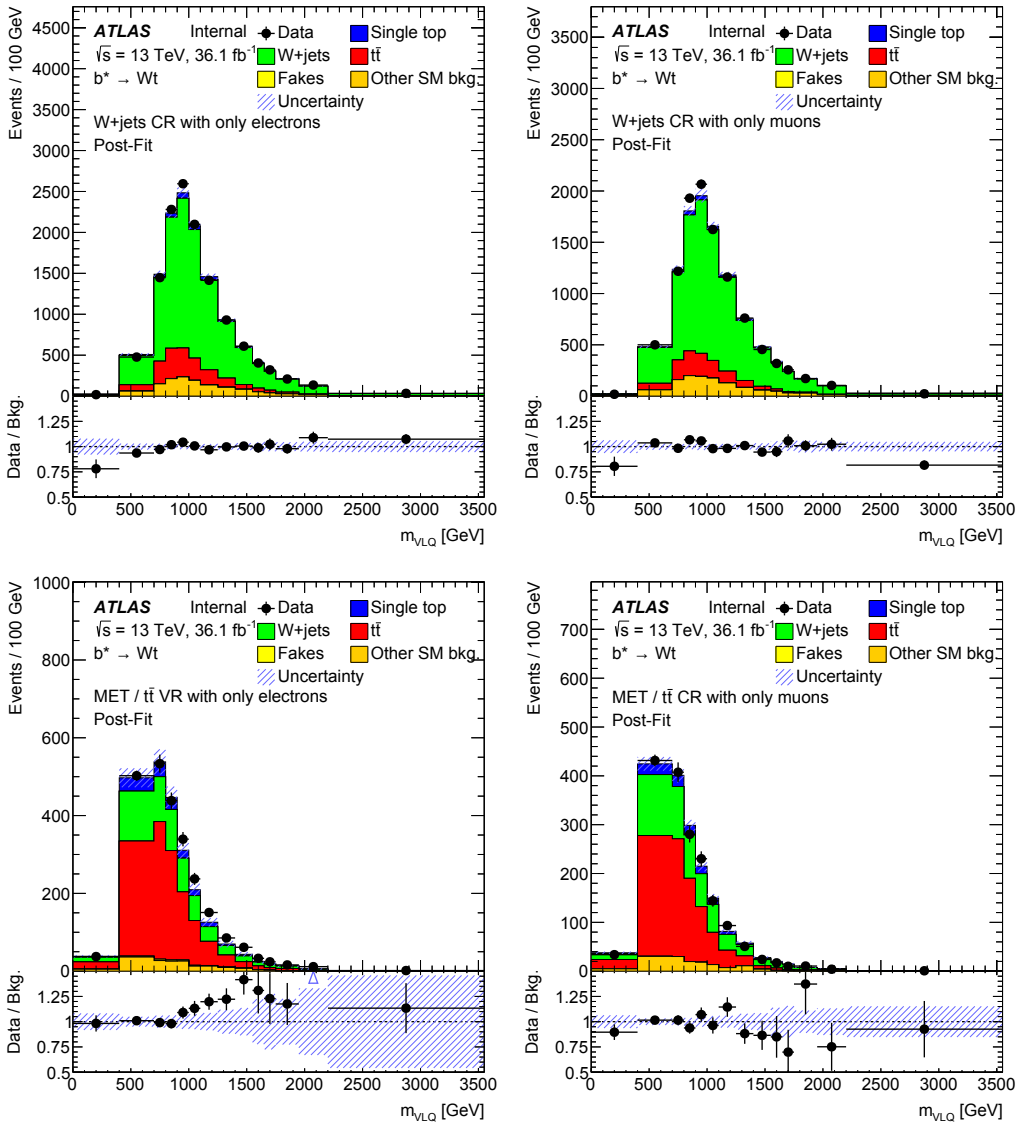

Figure 8.1: Invariant mass distribution of the electron and muon W+jets and low-E_T^{miss} control and validation region. The invariant mass in these plots is calculated from the lepton, neutrino and the leading large-radius jet. The fakes got reduced by the fit to an amount not / barely visible in the plots.

Not only is the normalization corrected, but also the shape got somewhat corrected in the W+jets control region. This results in pretty good agreement between the fitted expectation and the observed data in the W-jet control region, except for the tail bins. And this is achieved while constraining the systematic uncertainties as well. In the low-E_T^{miss} region, only the muon region is a control region and thus part of the fit. The agreement with data looks comparable to the W+jets control regions, just the statistics are smaller and thus the points fluctuate more visibly. The electron part of the low-E_T^{miss} region is used as a validation and thus was not part of the fit, but rather shows us how the corrected backgrounds match data in a region which didn't contribute to likelihood maximization. As expected the agreement is not as good as in the control regions and there is some deviation around 1.4 TeV. But this deviation is most likely not from the small fake electron contribution as this would be predominantly be below 1 TeV as seen in figure 7.15. Also the W+jets region doesn't show a lack of events and this is the primary reson for the small fit result.

8.1.1 Pull of nuisance parameters

In order to fit the different backgrounds to the observed data, the backgrounds are varied within their respective systematic uncertainties.

In figure 8.2 a subset of the considered systematic uncertainties is shown. The plot shows the chosen value of the systematic in quantities of σ of the systematic and post fit coverage range of each systematic shown as black bar. Before the fit each systematic would cover $\pm 1\sigma$ with a central value of 0. In order to keep computational effort acceptable and the plot somewhat readable, only systematics with at least 1% effect (pruning) on the final plots where considered. And from this selection only a small fraction is actually pulled in order to fit the background to data. The full set of systematics and the results of the 1% pruning threshold are shown in the appendix in figure B.1.

The most utilized systematics are one of the jet energy scale nuisance parameters, jet energy resolution, the flat fakes uncertainty and W+jets PDF0. Whereas the W+jets PDF0 uncertainty is due to technical reasons not actually a systematic of the PDF, but rather the difference between the nominal sample and the sample used to determine the PDF uncertainties. This means this uncertainty is effectively a second generator uncertainty. Therefore the designated generator uncertainty is highly anti-correlated to it, as can be seen in figure 8.3. This matrix shows the correlation between all the systematics which have at least in one combination more than 5% correlation.

The other set of highly correlated systematics are the ones concerning the $t\bar{t}$ sample, where the generator systematic is correlated with the cross-section and anti-correlated with the radiation systematic.

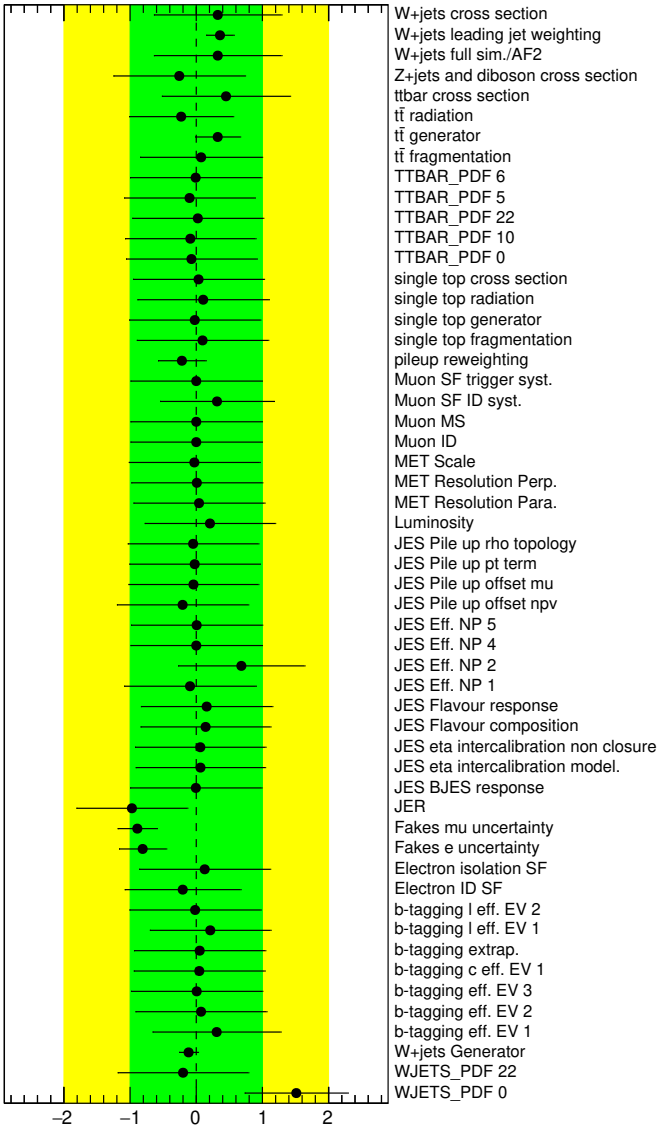

Figure 8.2: Pulls on the nuisance parameters from a fit of only background samples in the control regions.

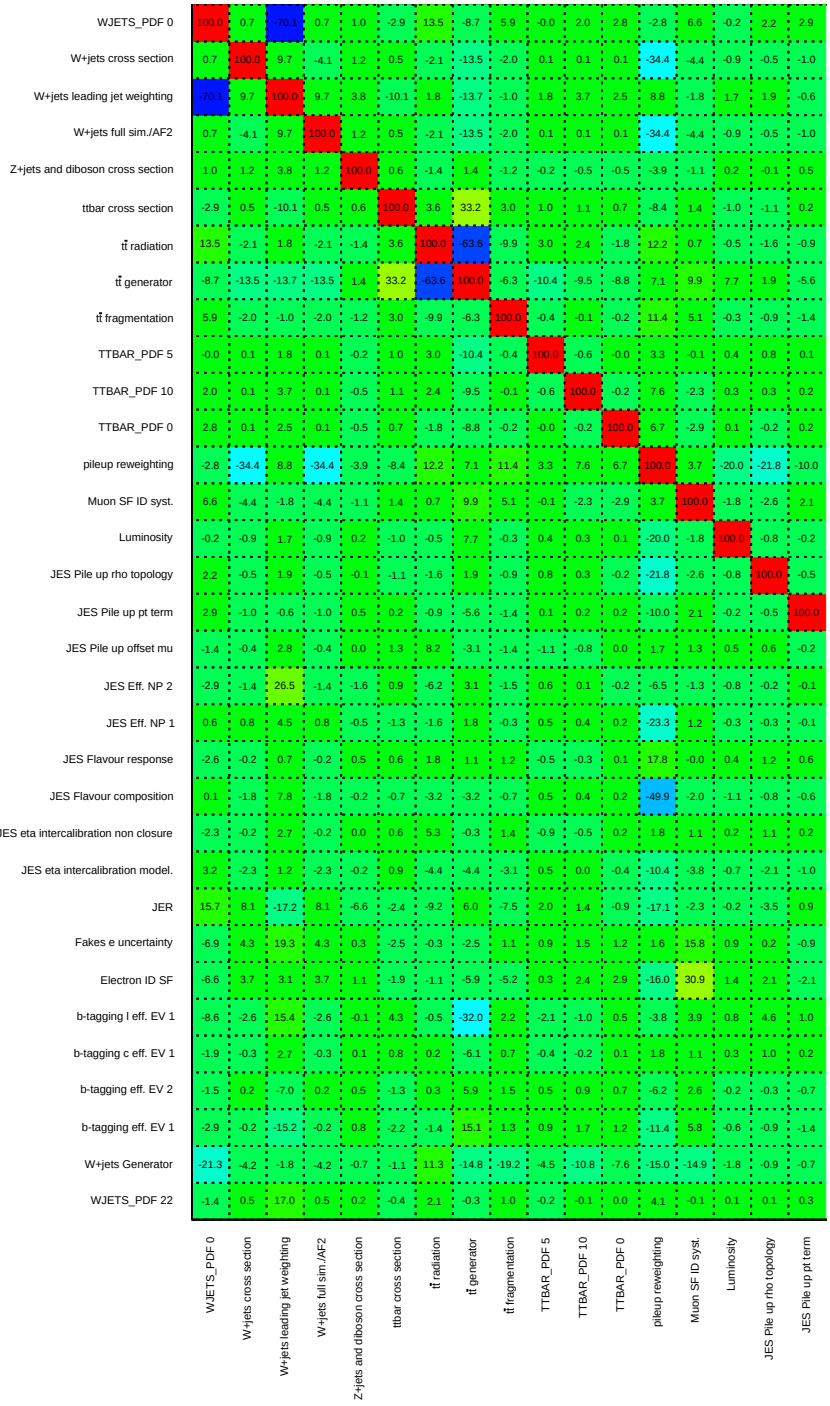

Figure 8.3: First half of correlation of the pulls on the nuisance parameters from a fit of only background samples in the control regions.

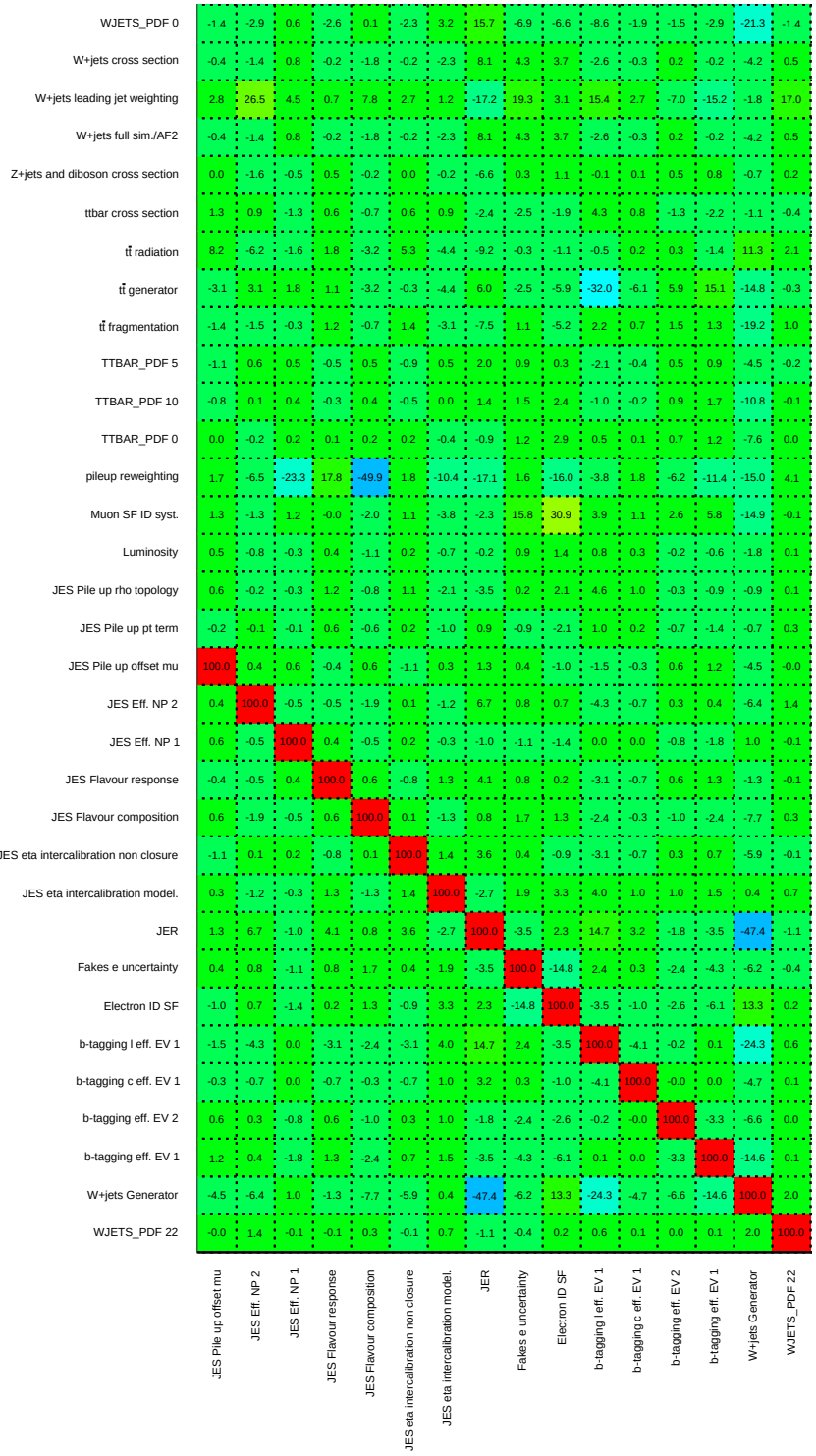

Figure 8.4: Second half of correlation of the pulls on the nuisance parameters from a fit of only background samples in the control regions.

Figure 8.2 shows as well, that some systematic variations are reduced. This is usually caused by overestimation of the systematic. It can be seen in particular in the generator systematics, the pile-up, fake and W+jets reweighting. For the reweighting and generator systematics this is somewhat expected as both are essentially wild guesses.

8.1.2 Expected limits

With the now improved background and systematic uncertainty description, the expected effect from the signal can be investigated. To do this, the fitted background is extrapolated into the signal region and the hypothesis of a signal for various masses can be tested using asymptotic properties of the likelihood function. As a result, we get the expected cross-section limit for all mass points probed. This is shown in figure 8.5. When comparing the expected cross-section limit line with theoretical cross-section for the different masses, the crossing point of expected cross-section limit denotes the expected mass limit. In case of unity mixing for both left and right handed b^*, the expected mass limit is even beyond the highest simulated mass point of 2.2 TeV. As the crossing point is very close and the shape of the expected cross-section limit is smooth, it was decided that no higher mass point was produced after the inital production campaign and the expected mass limit is obtained by extrapolation.

8.1.2.1 Final choice of discriminating varbiable

So far all the fitting and limit plots used as discriminating variable the invariant mass of the electron or muon, the neutrino and the leading p_T large jet. But when we were looking at different candidates in section 7.2.3.2, we kept open the option to add the b-jet in case its distance to the large jet is large enough. To conclude on this now, all the steps of fitting and limit setting are done for this alternative discriminating variable as well and the expected cross-section limit is shown in figure 8.6.

As expected from the small differences in the signal region between these two variables, the difference in the expected limit is also quite small. But upon close inspection, the invariant mass which does not explicitly include the b-jet has slightly better expected cross-section limits. So we can now fix the discriminating variable.

8.1.3 Validation of fit and limit setting procedure

With the analysis now in place, we have to do some final checks in order to make sure the fit does not converge in a weird local mininum. It needs to be tested that the limit setting procedure is actually sensitive to a signal

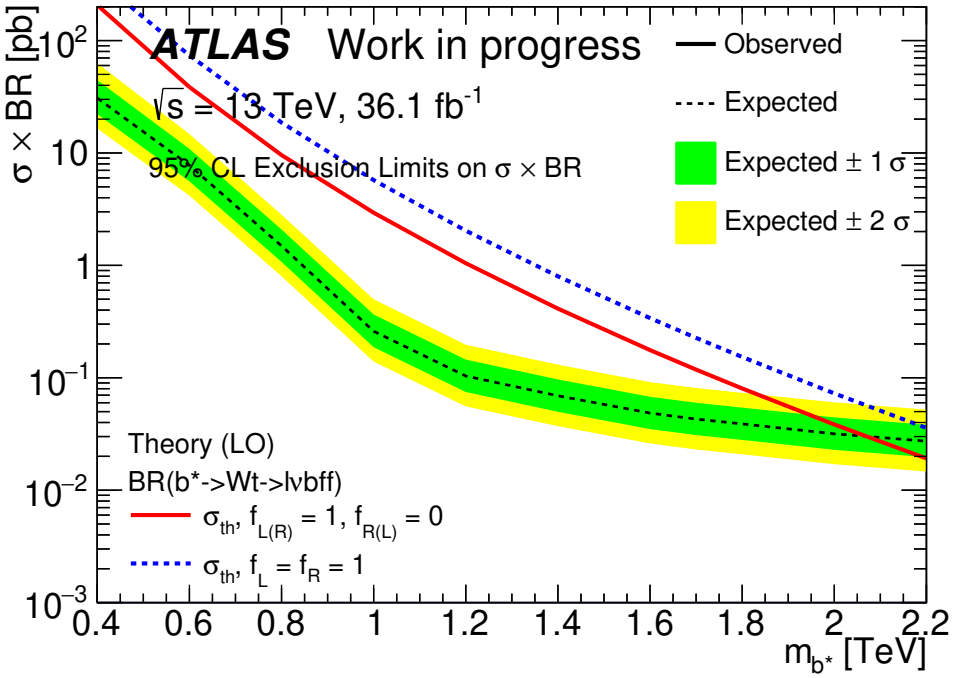

Figure 8.5: Expected cross-section limit from a fit of only background samples in the control regions.

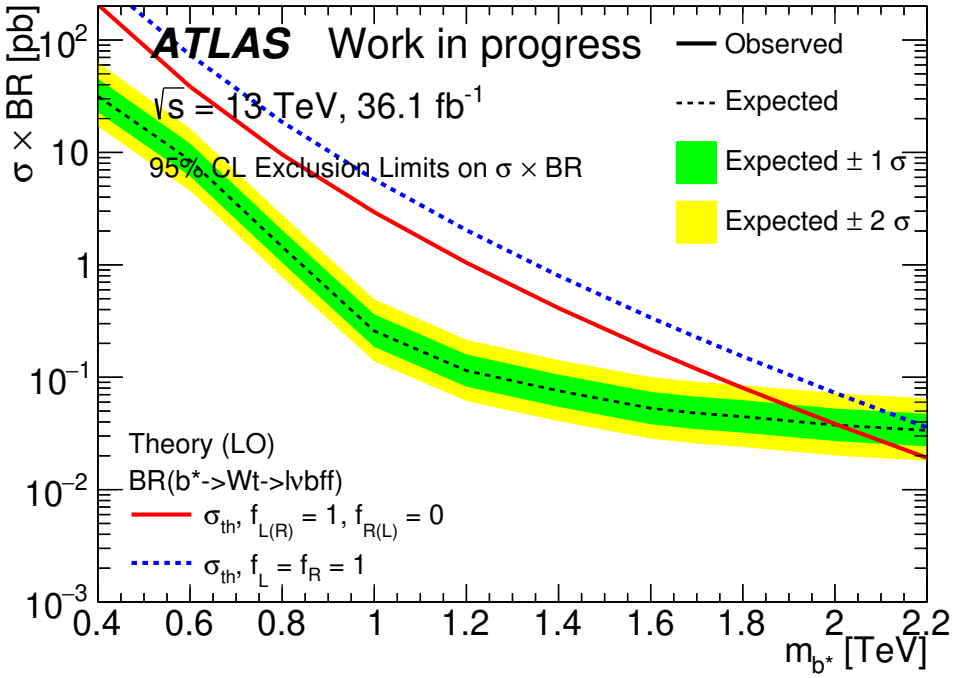

Figure 8.6: Expected cross-section limit from a fit of only background samples in the control regions. As discriminating variable the invariant mass of electron or muon, the neutrino, the leading p_T large jet and the b-jet in case of no overlap with the leading p_T large jet is used.

and the signal does not just get absorbed in the systematic uncertainties. To do these kind of validations, the fit and limit setting is run with several modifications. For one, the measured data is replaced by a synthetic set of events, Asimov sample, obtained by adding up all unmodified backgrounds. This so obtained data set corresponds to the background only hypothesis. The signal hypothesis sample is produced by adding up all backgrounds and a chosen representative signal point. For the following plots we chose the signal mass point of $m_{b^*} = 1700\,\text{GeV}$. Other mass points were also tested with comparable results.

8.1.3.1 Fitting of Asimov datasets

To make sure the systematic uncertainties do not cover up a potential signal, a fit with only the background samples is done on the Asimov samples for the background-only and signal hypothesis. The nuisance parameter pull plot for the background-only hypothesis sample is in figure 8.7. As expected, the systematics don't need to be pulled to reproduce a dataset built from the nominal event distributions for all backgrounds. But one can also see, that some systematics are constrained, indicating, that the statistics available is sufficient to constrain the large systematics. Thus the constraint of these systematics in a fit with measured data is not a result of particular event yields, but rather expected from the availiable statistics.

When running the fitting of background only events to an Asimov dataset, which has signal events included, the pull of the nuisance parameters is not 0 everywhere anymore as seen in figure 8.8. But this is expected as the fit now tries to accomodate events which are not part of the background samples. But unlike the pulls obtained from a fit of backgrounds in the control regions but with measured data, all systematics stay compatible with zero pull.

The case of having signal events included is much better described by a fit containing also signal regions. In the case of figure 8.9 the injected signal and the test signal are both the same $m_{b^*} = 1700\,\text{GeV}$. Thus the nominal value of all systematic variations is expected to fit the given data best, which is shown by a zero pull plot again. Also when looking in the extracted signal strength, the fit correctly recovers $\hat{\mu} = 1.0 \pm 0.2$.

All this shows that the fit seems to behave in an unbiased way.

8.1.3.2 Limit setting on Asimov dataset

We can also attempt to set limits with these background-only and signal events containing datasets. This primarily proves whether the limit setting procedure would actually uncover signal if it is present. Figures 8.10 and 8.11 show the expected and "observed" limit in cases of only background events and an injected signal of $m_{b^*} = 1700\,\text{GeV}$. With the injected signal, the

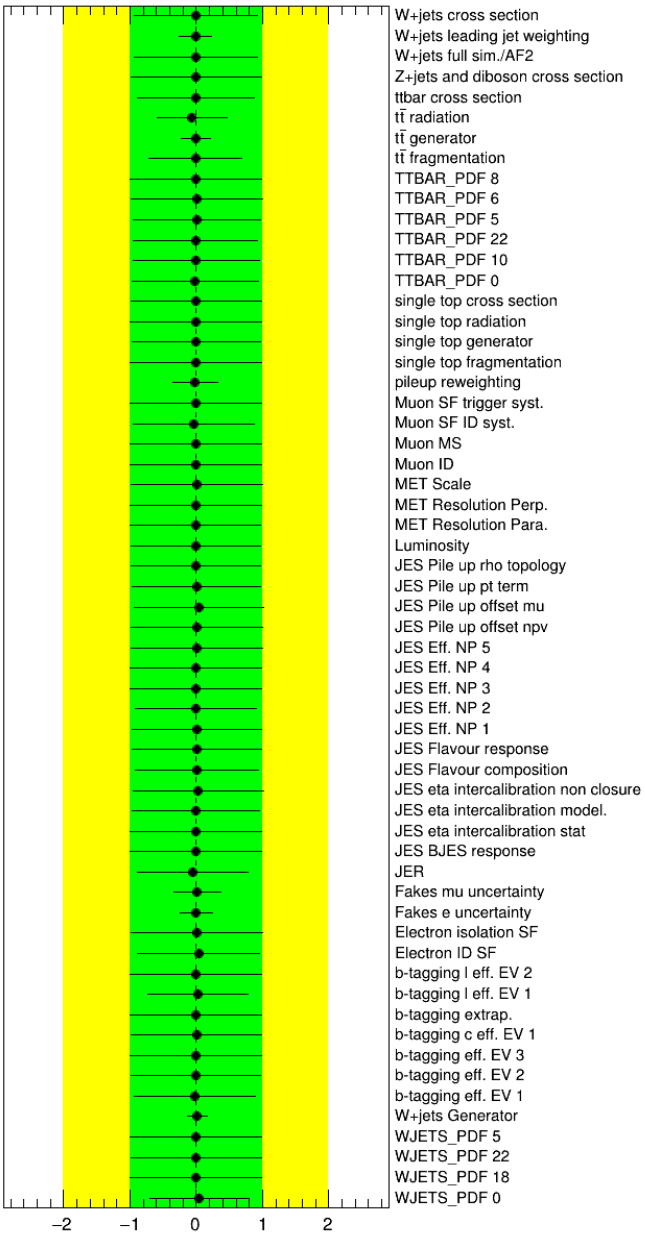

Figure 8.7: Nuisance parameter pull plot of the systematic uncertainties in case of a background only samples fit of an Asimov dataset for background-only hypothesis.

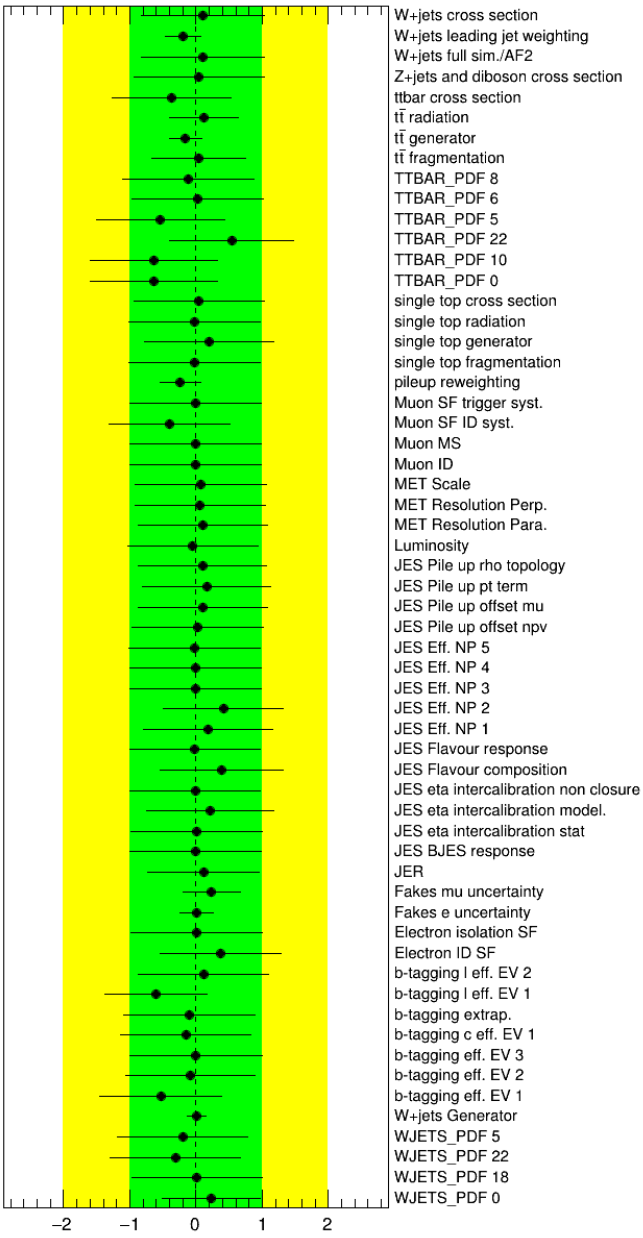

Figure 8.8: Nuisance parameter pull plot of the systematic uncertainties in case of a background only samples fit of an Asimov dataset containing background and signal events.

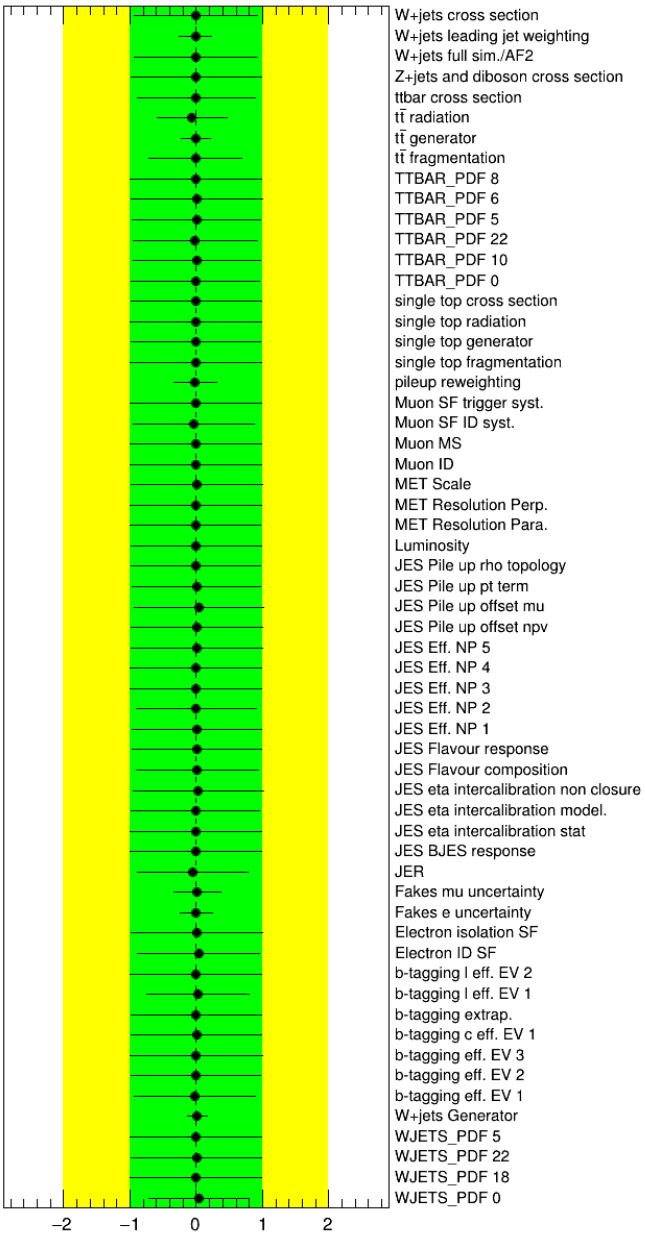

Figure 8.9: Nuisance parameter pull plot of the systematic uncertainties in case of a signal plus background samples fit of an Asimov dataset containing background and signal events.

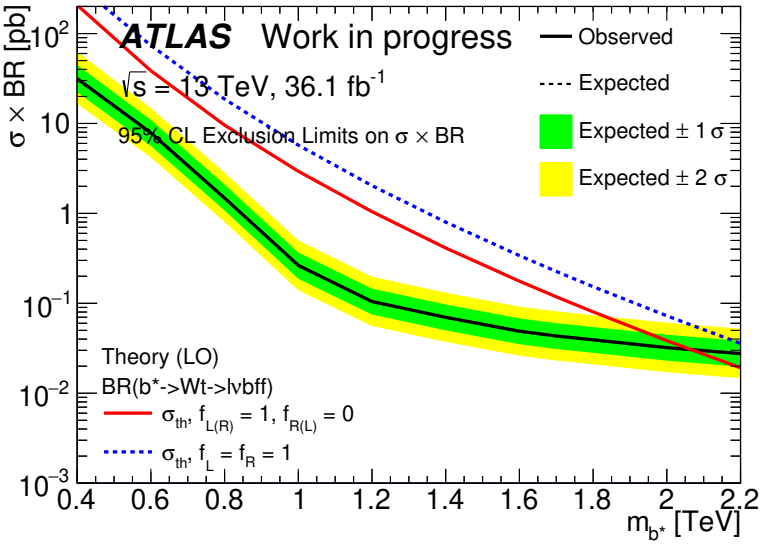

Figure 8.10: Cross-section limits obtained on Asimov data containing only background events.

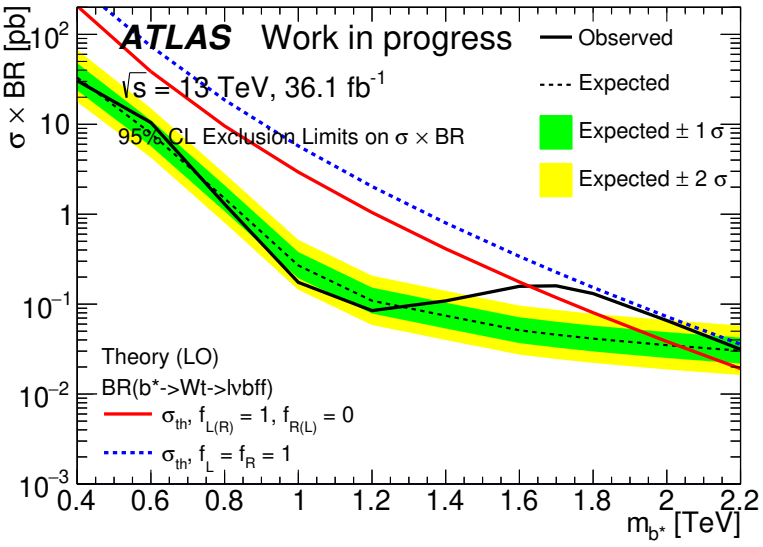

Figure 8.11: Cross-section limits obtained on Asimov data containing a $m_{b^*} = 1.7\,\text{TeV}$ signal and background events.

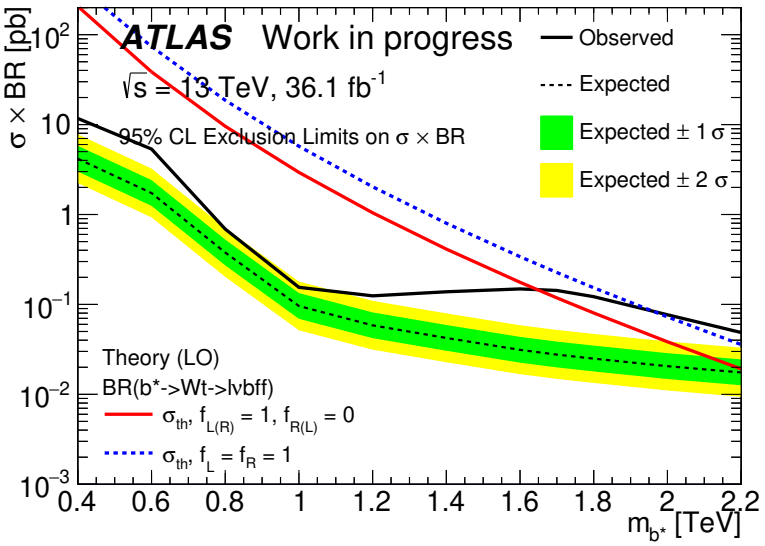

Figure 8.12: Cross-section limits based on statistical power alone, obtained on Asimov data containing a $m_{b^*} = 1.7\,\text{TeV}$ signal and background events. No systematic uncertainties are taken into account and thus only the effect from the finite statistics is shown.

cross-section limit stays above the theory cross-section for $m_{b^*} = 1700\,\text{GeV}$. Also neighboring mass points are affected, which adds to the confidence that we would not exclude signals even if they are not exactly at the simulated mass points. Even though the fit needed to accommodate the signal, the expected limit does not change much compared to the case of background-only Asimov data. Thus the calculation of the expected limit is properly done even with signal present.

To understand how much the cross-section limit is actually limted by the systmematics and what part is due to limited statistics, the limit setting on the Asimov datasets are repeated with no systematics enabled. The results are shown in figure 8.12. It is rather interesting, but not really surprising, that the largest differences are seen in the lower mass regions, where the effect from the systematics on the expected cross-section limit is up to a factor 10, while it is only a factor of two in the high mass region. This is most likely due the the higher backgrounds and thus background systematic uncertainties in the lower-mass bins of the discriminating variable. Also the nominal signal cross-section decreases more slowly for high masses than the signal yield of the background process, and thus the background becomes less relevant at higher masses.

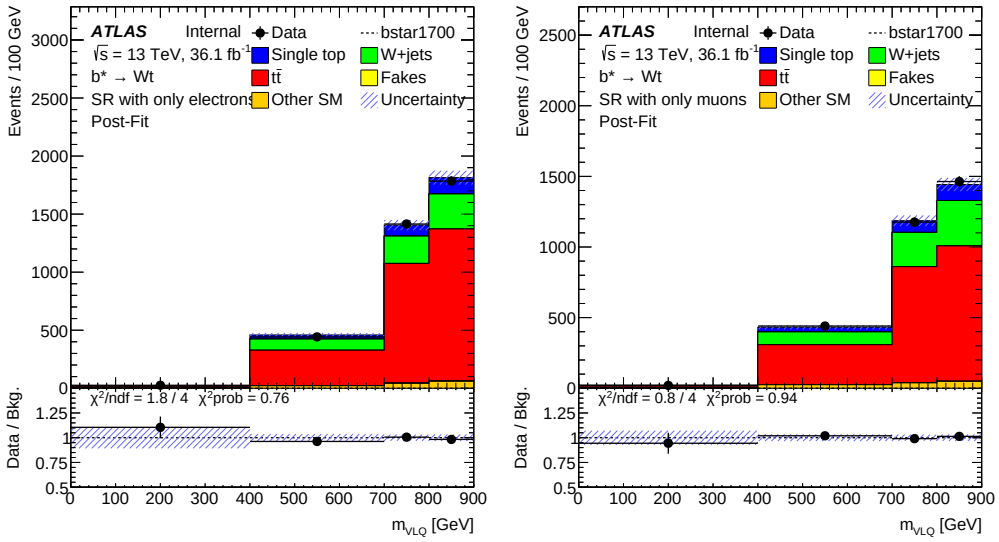

Figure 8.13: Partially unblinded signal region containing only the four lowest mass bins. These bins don't contain much expected signal, but show that the $t\bar{t}$ expectation matches measured data after the backgrounds were fitted to the control regions and these bins of the signal region.

8.1.3.3 Partial unblinding

In order to go towards an unblinded signal region, an intermediate step of a partially unblinded signal region is taken. This is done to make sure, that even with the limited constraining power of the control regions on the $t\bar{t}$ background, the modelling is adequate. The first four mass bins are unblinded first, as they don't contain much signal of the interesting high mass b^* we are looking for. In figure 8.13 the first four bins of the signal regions are shown as they where part of the fit. The good agreement between the expected background events and the observed events increases our confidence, that the background modelling is reasonable. In Figure 8.14 the nuisance parameters of the fit are shown. They need to be compared to Figure 8.2. The main difference between the nuisance parameter plot with just the control regions versus the control regions plus the partially unblinded signal region is the constraint and a small pull of the radiation, generator and fragmentation uncertainties of the $t\bar{t}$ sample. This is expected as already these few bins of the signal region contain comparable number of $t\bar{t}$ events as the full control regions with an even higher purity.

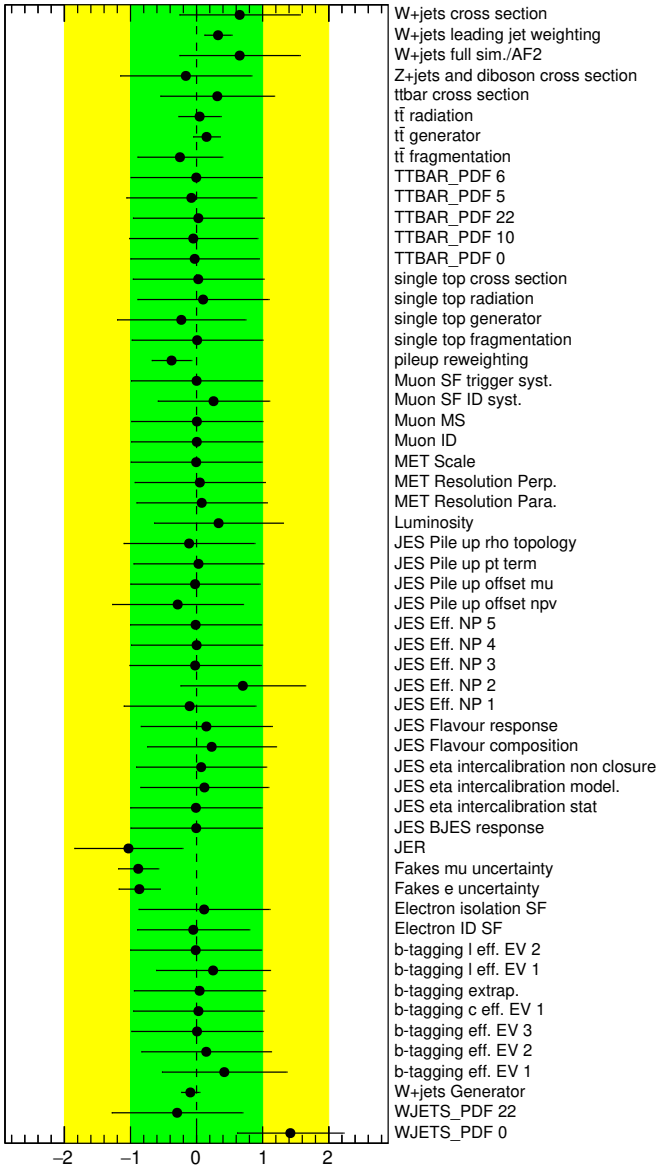

Figure 8.14: Nuisance parameter plot of the partially unblinded signal region and full background fit.

8.1.4 Final fit with full unblinding

After the validation of the background estimates without looking at the measured data distribution in the signal regions, the final step is running the full fit and limit setting including the signal regions. The control, validation and signal regions are shown in figure 8.15. The agreement between measured data and expected background is quite good. The only big deviation between data and expectation is in the validation region of the low-E_T^{miss} electron region. But this was already present before the signal region was included in the fit. Thus including the signal region didn't move the backgrounds so much, that the agreement in the control or validation region changed much. This is a good sign and indicates that the background estimation obtained by just the control regions was already decent. Looking a little closer in the signal region, we see a small deficit of events around 1.5 TeV. Comparing this to the control regions does not show indications of a systematic background mismodelling in this direction.

With the fit in place we can also have a look on the pulls of the nuisance parameters in figure 8.16. This should be compared to the equivalent plots of the fit of just the control regions in figure 8.2 and the fit of the control regions and a partially unblinded signal region in figure 8.14. Comparing these shows even larger differences than we got from the partial unblinding. Most notably two b-tagging efficiencies and one JES efficiency systematic change slightly. Also $t\bar{t}$ related systematics change. The latter is definitly not surprising, as the signal regions have more $t\bar{t}$ events than any other region. But non of the pull changes should cause a big change in background predictions.

Figure 8.17 shows the effect from the most significant systematics on the signal strength obtained in the limit setting. Quite unsurprisingly, the largest effect on the obtained limit comes from the $t\bar{t}$ cross-section. A little bit more surprising is the effect from the single top cross-section, given that single-top production gives a small contribution to the signal region. But it is also not unreasonable, given that the signal itself does not add a huge number of events to the signal region either and there is no control region dedicated towards constraining single-top contributions better.

The comparison between the correlation matrices of the nuisance parameters with and without the signal regions in the fit in figures 8.3,8.4,8.18 and 8.19 shows only minor differences. The only significant differences are the $t\bar{t}$ systematics, which is somewhat expected with better constraints on these.

With no obvious problems in the signal region and in the pulls on systematics in the fit, we can look now into the expected and observed mass dependent cross-section limit of for b^* production figure 8.20. By reading off the (extrapolated) intersection between the theory cross-section and the expected / observed cross-section limit, the mass limit can be obtained. In the case that only either f_L or f_R is 1 and the other 0, we get an expected mass limit of

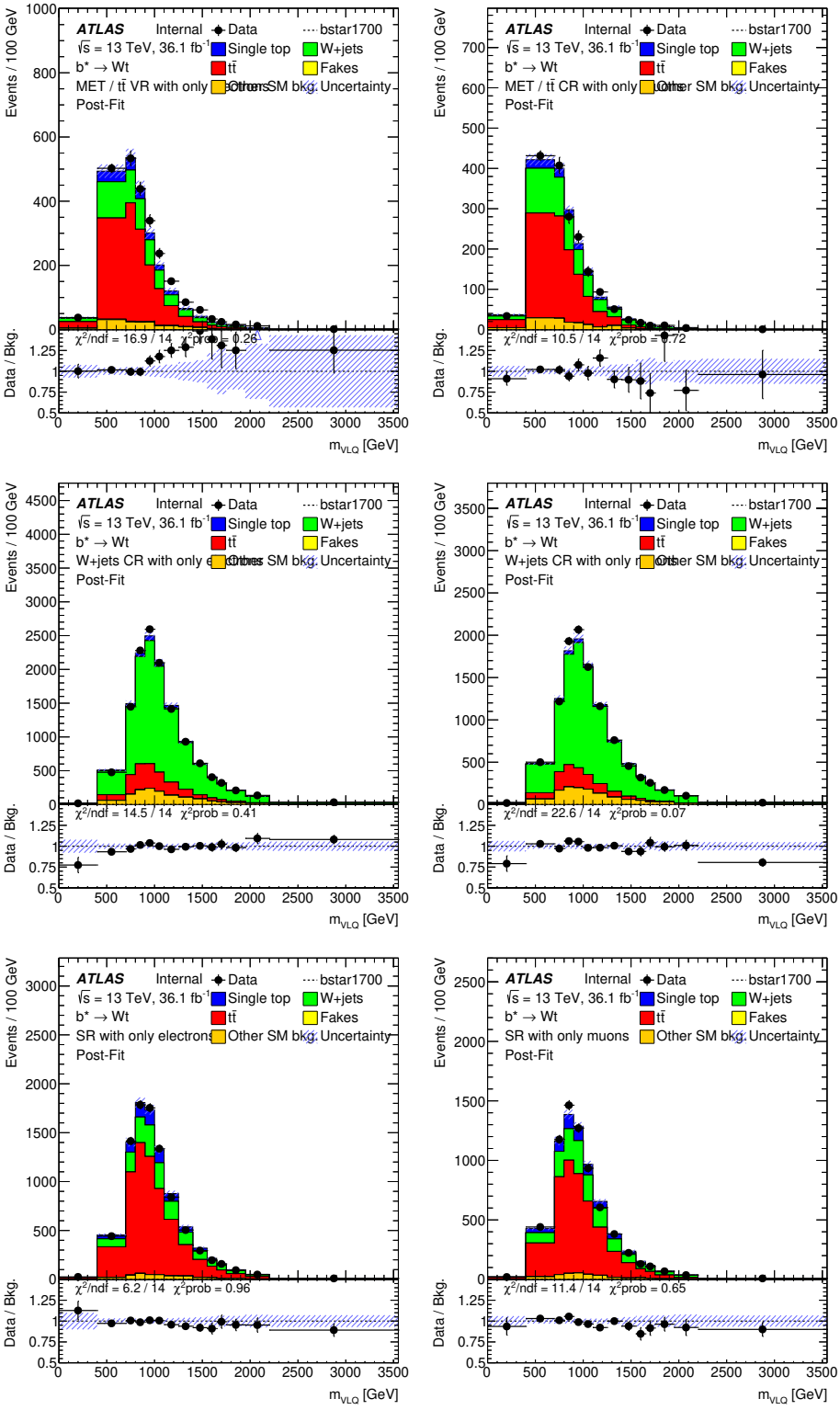

Figure 8.15: Control, validation and signal regions after unblinding the signal region. The background estimates are post-fit, where the fitting contained also the data distribution in the signal region.

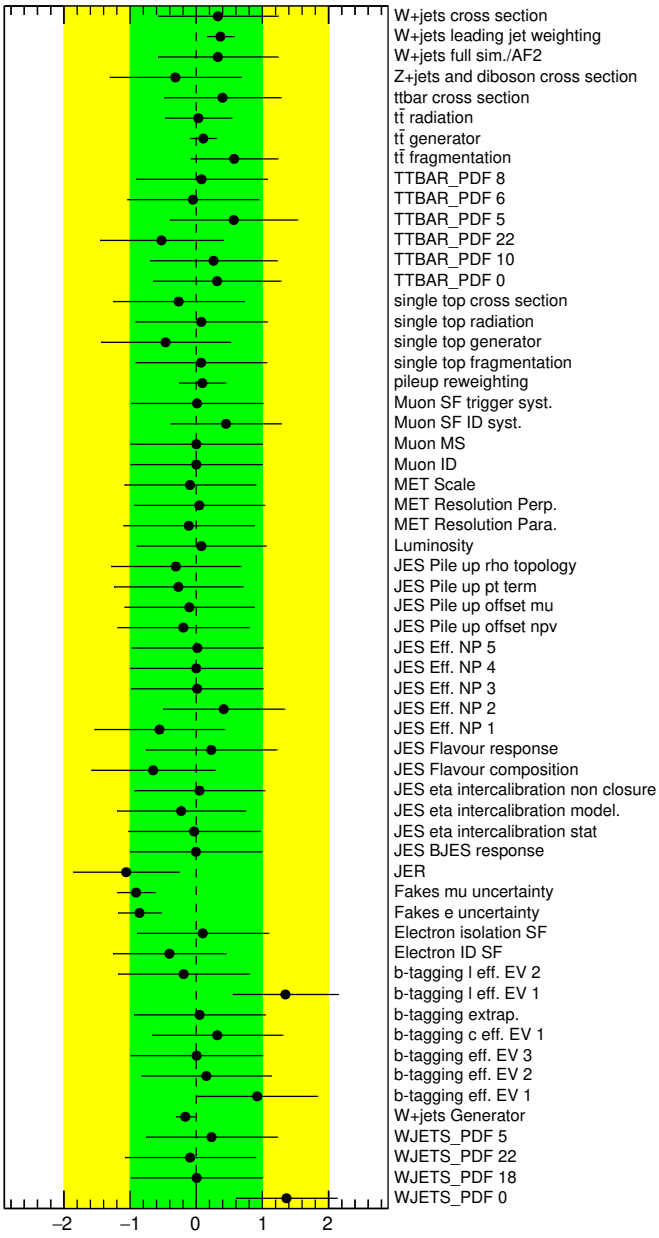

Figure 8.16: Nuisance parameter plot of the fully unblinded fit.

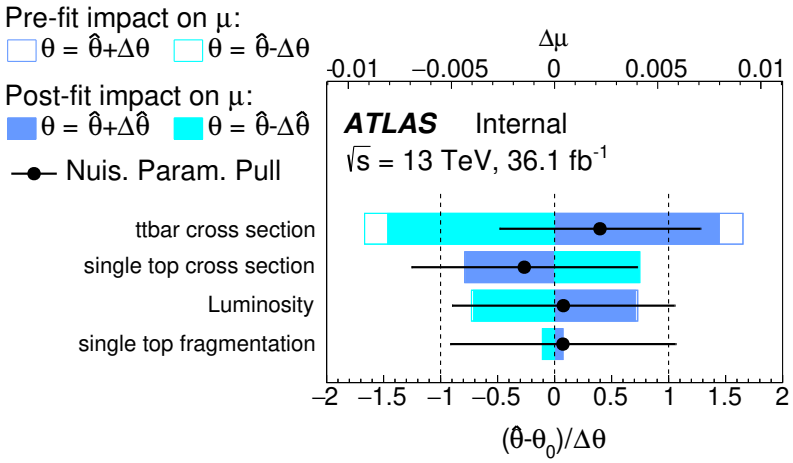

Figure 8.17: Ranking of the nuisance parameters of the fully unblinded fit.

$m_{b^*,\mathrm{exp}} = 2.17\,\mathrm{TeV}$ and an observed mass limit of $m_{b^*,\mathrm{obs}} = 2.24\,\mathrm{TeV}$. In the case of $f_L = f_R = 1$, an even higher expected mass limit of $m_{b^*,\mathrm{exp}} = 2.4\,\mathrm{TeV}$ and an observed mass limit of $m_{b^*,\mathrm{obs}} = 2.5\,\mathrm{TeV}$ is reached. For lower masses the cross section limit can be interpreted as a limit on coupling combinations as well. From 3.55 and 3.57 we know that the cross section scales with $\sqrt{f_L^2 + f_R^2}$ and $\sqrt{\kappa_L^2 + \kappa_R^2} = f_g$. Figure 8.21 shows the corresponding coupling limits for different masses in the plane f_g – $f_L = f_R$.

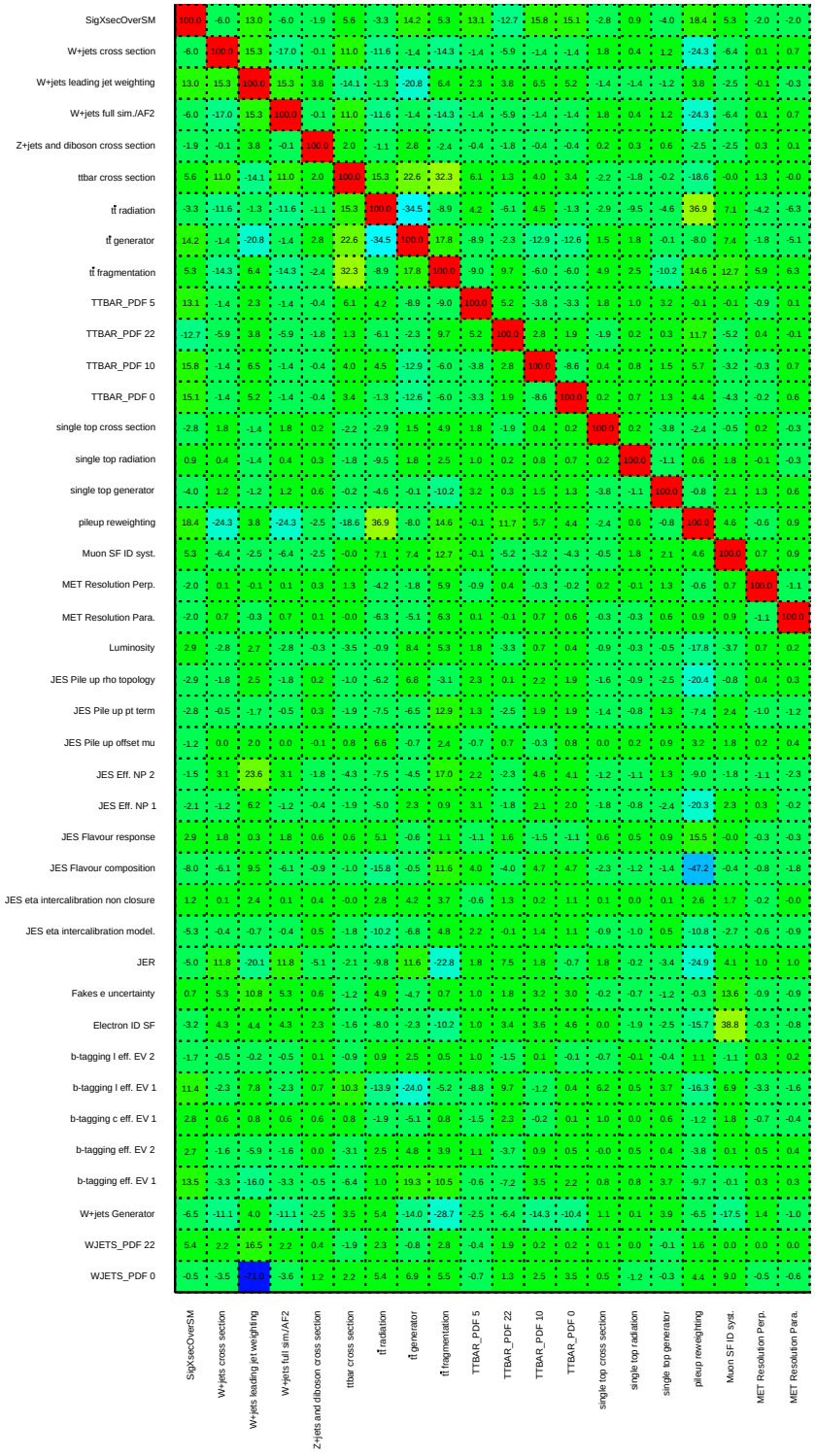

Figure 8.18: First half of the correlation matrix of the nuisance parameters of the fully unblinded fit.

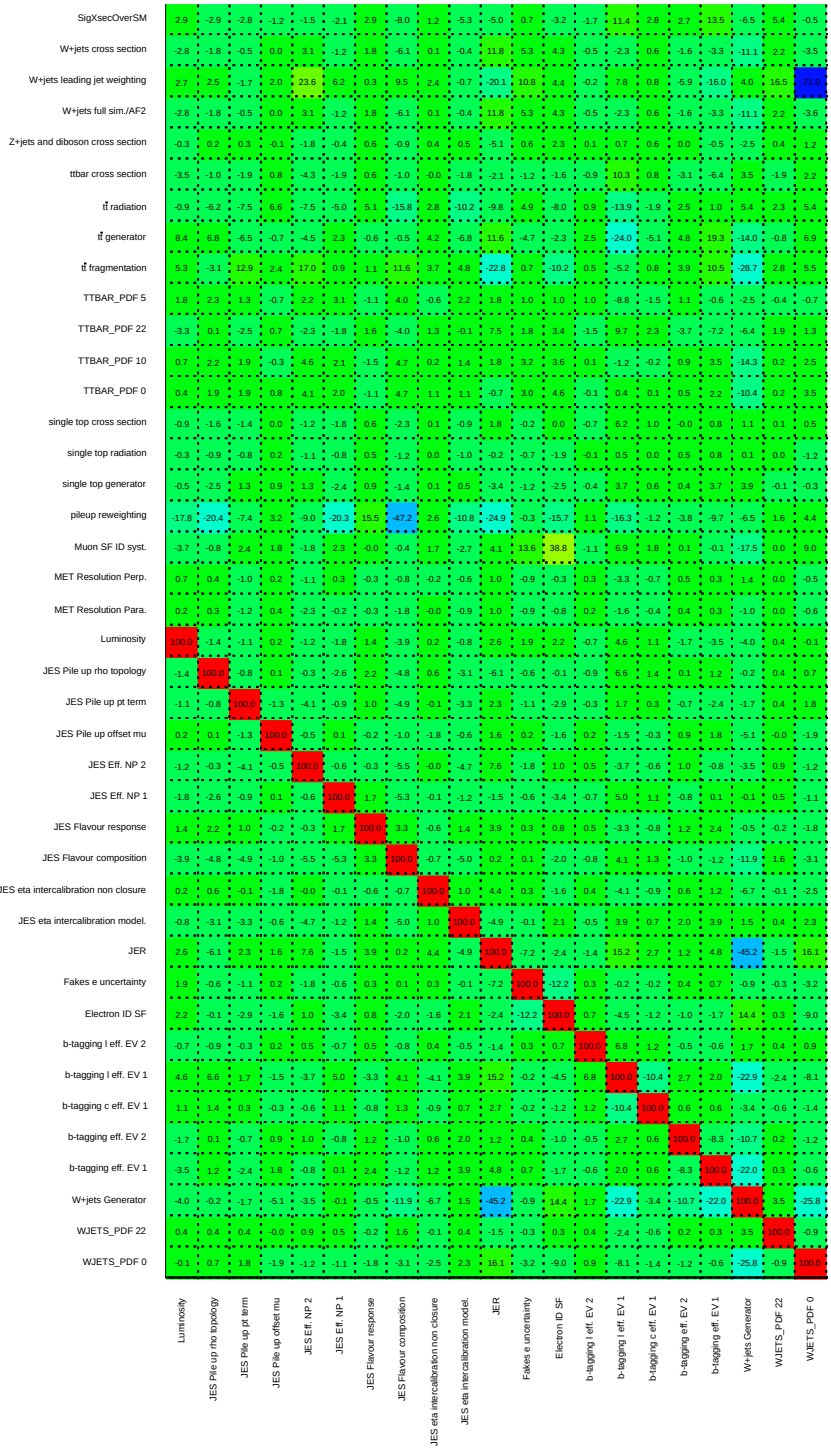

Figure 8.19: Second half of the correlation matrix of the nuisance parameters of the fully unblinded fit.

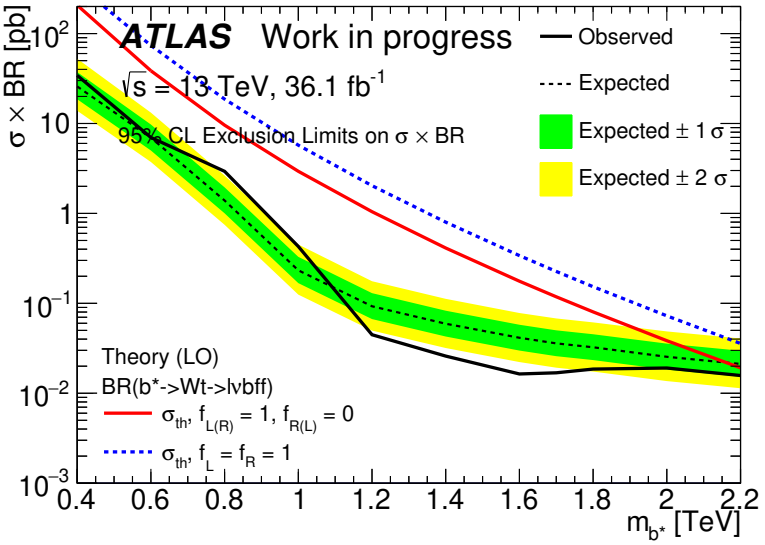

Figure 8.20: Final expected and observed cross-section limit as a function of b^* mass.

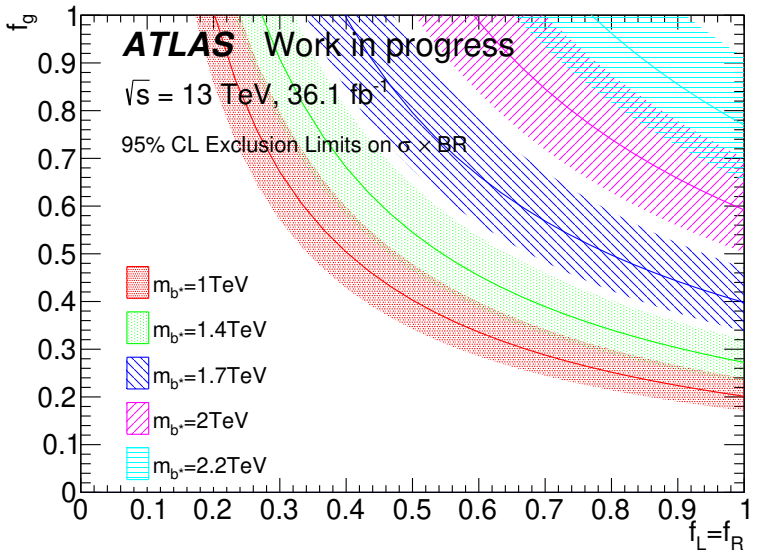

(a)

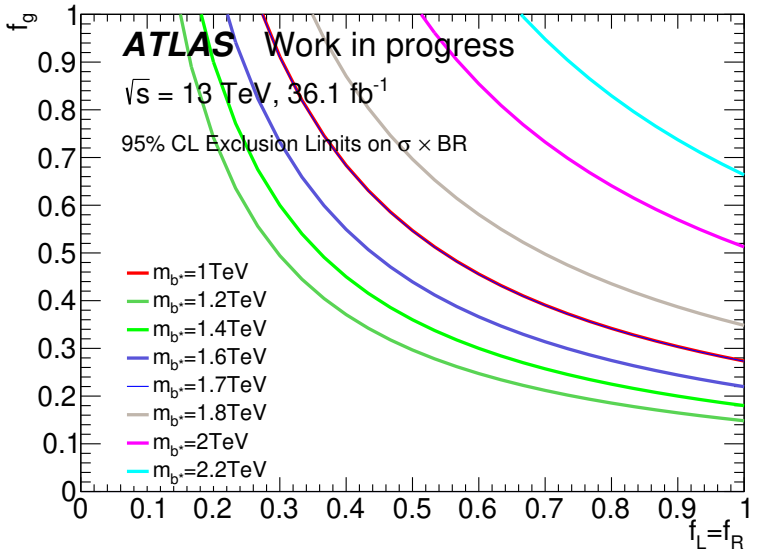

(b)

Figure 8.21: Limit in the $f_g - f_L = f_R$ coupling parameter plane, in (a) for the expected limit and in (b) for the observed limit. Coincidentally, the lines for $m_{b^*} = 1\,\text{TeV}$ and $m_{b^*} = 1.7\,\text{TeV}$ are exactly on top of each other due to variations in the observed cross-section times branching ratio limit.

Chapter 9

Summary

In this thesis we created signal samples and an analysis to search for b^*, an excited b quark, in the Wt final state with one W decaying leptonically. To obtain a competitive result, a new analysis strategy was found to efficiently use the higher collision energy compared to earlier analysis. The data is consistent with the background only hypothesis and thus we obtain exclusion limits. A production of both left- and right-handed b^* via an anomalous colored magnetic coupling with standard model b quarks for production and an electroweak anomalous magnetic coupling for decay with nominal (unit coupling) strength can be excluded with an expected limit up to $m_{b^*,\mathrm{exp}} = 2.4\,\mathrm{TeV}$ and an observed limit up to $m_{b^*,\mathrm{obs}} = 2.5\,\mathrm{TeV}$. This is quite an improvement over the prior $m_{b^*,\mathrm{exp}} = 1.65\,\mathrm{TeV}$ and an observed limit of $m_{b^*,\mathrm{obs}} = 1.5\,\mathrm{TeV}$ obtained in the $\sqrt{s} = 8\,\mathrm{TeV}$ search at ATLAS [29]. In addition to the unit coupling case, also coupling limits could be obtained for several masses, improving also these limits. The lowest limits are obtained for a mass of $m_{b^*,\mathrm{obs}} = 1.2\,\mathrm{TeV}$ with limits of e.g. $f_g = F_L = F_R = 0.39$. For $m_{b^*,\mathrm{obs}} = 1.6\,\mathrm{TeV}$, the limit on the coupling is still $f_g = F_L = F_R = 0.47$ and for $m_{b^*,\mathrm{obs}} = 2\,\mathrm{TeV}$ it is $f_g = F_L = F_R = 0.72$.

Bibliography

[1] Estimation of non-prompt and fake lepton backgrounds in final states with top quarks produced in proton-proton collisions at $\sqrt{s}$=8 TeV with the ATLAS detector. Technical Report ATLAS-CONF-2014-058, CERN, Geneva, Oct 2014.

[2] Tagging and suppression of pileup jets with the ATLAS detector. Technical Report ATLAS-CONF-2014-018, CERN, Geneva, May 2014.

[3] Expected performance of missing transverse momentum reconstruction for the ATLAS detector at $\sqrt{s} = 13$ TeV. Technical Report ATL-PHYS-PUB-2015-023, CERN, Geneva, Jul 2015.

[4] Monte Carlo Calibration and Combination of In-situ Measurements of Jet Energy Scale, Jet Energy Resolution and Jet Mass in ATLAS. Technical Report ATLAS-CONF-2015-037, CERN, Geneva, Aug 2015.

[5] Selection of jets produced in 13TeV proton-proton collisions with the ATLAS detector. Technical Report ATLAS-CONF-2015-029, CERN, Geneva, Jul 2015.

[6] Electron and photon energy calibration with the ATLAS detector using data collected in 2015 at $\sqrt{s} = 13$ TeV. Technical Report ATL-PHYS-PUB-2016-015, CERN, Geneva, Aug 2016.

[7] Electron efficiency measurements with the ATLAS detector using the 2015 LHC proton-proton collision data. Technical Report ATLAS-CONF-2016-024, CERN, Geneva, Jun 2016.

[8] Optimisation of the ATLAS b-tagging performance for the 2016 LHC Run. Technical Report ATL-PHYS-PUB-2016-012, CERN, Geneva, Jun 2016.

[9] Performance of b-jet identification in the ATLAS experiment. Journal of Instrumentation, 11(04):P04008–P04008, apr 2016.

[10] ATLAS simulation of boson plus jets processes in Run 2. Technical Report ATL-PHYS-PUB-2017-006, CERN, Geneva, May 2017.

[11] Electron and photon reconstruction and performance in ATLAS using a dynamical, topological cell clustering-based approach. Technical Report ATL-PHYS-PUB-2017-022, CERN, Geneva, Dec 2017.

[12] Jet reclustering and close-by effects in ATLAS run II. Technical Report ATLAS-CONF-2017-062, CERN, Geneva, Jul 2017.

[13] Multi-Boson Simulation for 13 TeV ATLAS Analyses. Technical report, CERN, Geneva, May 2017. All figures including auxiliary figures are available at https://atlas.web.cern.ch/Atlas/GROUPS/PHYSICS/PUBNOTES/ATL-PHYS-PUB-2017-005.

[14] Calibration of the b-tagging efficiency on charm jets using a sample of $W+c$ events with $\sqrt{s}$ = 13 TeV ATLAS data. Technical Report ATLAS-CONF-2018-055, CERN, Geneva, Dec 2018.

[15] $E_{\mathrm{T}}^{\mathrm{miss}}$ performance in the ATLAS detector using 2015-2016 LHC p-p collisions. Technical Report ATLAS-CONF-2018-023, CERN, Geneva, Jun 2018.

[16] Improvements in $t\bar{t}$ modelling using NLO+PS Monte Carlo generators for Run2. Technical Report ATL-PHYS-PUB-2018-009, CERN, Geneva, Jul 2018.

[17] M. Aaboud et al. Luminosity determination in pp collisions at $\sqrt{s}$= 8 TeV using the ATLAS detector at the LHC. Eur. Phys. J., C76(12):653, 2016.

[18] M. Aaboud et al. Jet energy scale measurements and their systematic uncertainties in proton-proton collisions at $\sqrt{s} = 13$ TeV with the ATLAS detector. Phys. Rev., D96(7):072002, 2017.

[19] M. Aaboud et al. Electron and photon energy calibration with the ATLAS detector using 2015-2016 LHC proton-proton collision data. Submitted to: JINST, 2018.

[20] M. Aaboud et al. Measurement of the Higgs boson mass in the $H \to ZZ^* \to 4\ell$ and $H \to \gamma\gamma$ channels with $\sqrt{s} = 13$ TeV pp collisions using the ATLAS detector. Phys. Lett., B784:345–366, 2018.

[21] M. Aaboud et al. Measurements of b-jet tagging efficiency with the ATLAS detector using $t\bar{t}$ events at $\sqrt{s} = 13$ TeV. JHEP, 08:089, 2018.

[22] M. Aaboud et al. Performance of missing transverse momentum reconstruction with the ATLAS detector using proton-proton collisions at $\sqrt{s}$ = 13 TeV. 2018.

[23] G. Aad et al. Atlas pixel detector electronics and sensors. Journal of Instrumentation, 3(07):P07007, 2008.

[24] G. Aad et al. The ATLAS Experiment at the CERN Large Hadron Collider. JINST, 3:S08003, 2008.

[25] G. Aad et al. Readiness of the ATLAS Tile Calorimeter for LHC collisions. Eur. Phys. J., C70:1193–1236, 2010.

[26] G. Aad et al. The ATLAS Simulation Infrastructure. Eur. Phys. J., C70:823–874, 2010.

[27] G. Aad et al. Observation of a new particle in the search for the Standard Model Higgs boson with the ATLAS detector at the LHC. Phys. Lett., B716:1–29, 2012.

[28] G. Aad et al. Muon reconstruction performance of the ATLAS detector in proton–proton collision data at $\sqrt{s}$ =13 TeV. Eur. Phys. J., C76(5):292, 2016.

[29] G. Aad et al. Search for the production of single vector-like and excited quarks in the Wt final state in pp collisions at $\sqrt{s} = 8$ TeV with the ATLAS detector. JHEP, 02:110, 2016.

[30] G. Aad et al. Topological cell clustering in the ATLAS calorimeters and its performance in LHC Run 1. Eur. Phys. J., C77:490, 2017.

[31] A. Abdesselam et al. The atlas semiconductor tracker end-cap module. Nuclear Instruments and Methods in Physics Research Section A: Accelerators, Spectrometers, Detectors and Associated Equipment, 575(3):353 – 389, 2007.

[32] S. Agostinelli, J. Allison, K. Amako, J. Apostolakis, H. Araujo, P. Arce, M. Asai, D. Axen, S. Banerjee, G. Barrand, F. Behner, L. Bellagamba, J. Boudreau, L. Broglia, A. Brunengo, H. Burkhardt, S. Chauvie, J. Chuma, R. Chytracek, G. Cooperman, G. Cosmo, P. Degtyarenko, A. Dell'Acqua, G. Depaola, D. Dietrich, R. Enami, A. Feliciello, C. Ferguson, H. Fesefeldt, G. Folger, F. Foppiano, A. Forti, S. Garelli, S. Giani, R. Giannitrapani, D. Gibin, J. G. Cadenas, I. González, G. G. Abril, G. Greeniaus, W. Greiner, V. Grichine, A. Grossheim, S. Guatelli, P. Gumplinger, R. Hamatsu, K. Hashimoto, H. Hasui, A. Heikkinen, A. Howard, V. Ivanchenko, A. Johnson, F. Jones, J. Kallenbach, N. Kanaya, M. Kawabata, Y. Kawabata, M. Kawaguti, S. Kelner, P. Kent, A. Kimura, T. Kodama, R. Kokoulin, M. Kossov, H. Kurashige, E. Lamanna, T. Lampén, V. Lara, V. Lefebure, F. Lei, M. Liendl,

W. Lockman, F. Longo, S. Magni, M. Maire, E. Medernach, K. Minamimoto, P. M. de Freitas, Y. Morita, K. Murakami, M. Nagamatu, R. Nartallo, P. Nieminen, T. Nishimura, K. Ohtsubo, M. Okamura, S. O'Neale, Y. Oohata, K. Paech, J. Perl, A. Pfeiffer, M. Pia, F. Ranjard, A. Rybin, S. Sadilov, E. D. Salvo, G. Santin, T. Sasaki, N. Savvas, Y. Sawada, S. Scherer, S. Sei, V. Sirotenko, D. Smith, N. Starkov, H. Stoecker, J. Sulkimo, M. Takahata, S. Tanaka, E. Tcherniaev, E. S. Tehrani, M. Tropeano, P. Truscott, H. Uno, L. Urban, P. Urban, M. Verderi, A. Walkden, W. Wander, H. Weber, J. Wellisch, T. Wenaus, D. Williams, D. Wright, T. Yamada, H. Yoshida, and D. Zschiesche. Geant4—a simulation toolkit. Nuclear Instruments and Methods in Physics Research Section A: Accelerators, Spectrometers, Detectors and Associated Equipment, 506(3):250 – 303, 2003.

[33] S. Alioli, P. Nason, C. Oleari, and E. Re. A general framework for implementing NLO calculations in shower Monte Carlo programs: the POWHEG BOX. JHEP, 06:043, 2010.

[34] J. Allison, K. Amako, J. Apostolakis, H. Araujo, P. A. Dubois, M. Asai, G. Barrand, R. Capra, S. Chauvie, R. Chytracek, G. A. P. Cirrone, G. Cooperman, G. Cosmo, G. Cuttone, G. G. Daquino, M. Donszelmann, M. Dressel, G. Folger, F. Foppiano, J. Generowicz, V. Grichine, S. Guatelli, P. Gumplinger, A. Heikkinen, I. Hrivnacova, A. Howard, S. Incerti, V. Ivanchenko, T. Johnson, F. Jones, T. Koi, R. Kokoulin, M. Kossov, H. Kurashige, V. Lara, S. Larsson, F. Lei, O. Link, F. Longo, M. Maire, A. Mantero, B. Mascialino, I. McLaren, P. M. Lorenzo, K. Minamimoto, K. Murakami, P. Nieminen, L. Pandola, S. Parlati, L. Peralta, J. Perl, A. Pfeiffer, M. G. Pia, A. Ribon, P. Rodrigues, G. Russo, S. Sadilov, G. Santin, T. Sasaki, D. Smith, N. Starkov, S. Tanaka, E. Tcherniaev, B. Tome, A. Trindade, P. Truscott, L. Urban, M. Verderi, A. Walkden, J. P. Wellisch, D. C. Williams, D. Wright, and H. Yoshida. Geant4 developments and applications. IEEE Transactions on Nuclear Science, 53(1):270–278, Feb 2006.

[35] J. Allison, K. Amako, J. Apostolakis, P. Arce, M. Asai, T. Aso, E. Bagli, A. Bagulya, S. Banerjee, G. Barrand, B. Beck, A. Bogdanov, D. Brandt, J. Brown, H. Burkhardt, P. Canal, D. Cano-Ott, S. Chauvie, K. Cho, G. Cirrone, G. Cooperman, M. Cortés-Giraldo, G. Cosmo, G. Cuttone, G. Depaola, L. Desorgher, X. Dong, A. Dotti, V. Elvira, G. Folger, Z. Francis, A. Galoyan, L. Garnier, M. Gayer, K. Genser, V. Grichine, S. Guatelli, P. Guèye, P. Gumplinger, A. Howard, I. Hřivnáčová, S. Hwang, S. Incerti, A. Ivanchenko, V. Ivanchenko, F. Jones, S. Jun, P. Kaitaniemi, N. Karakatsanis, M. Karamitros, M. Kelsey, A. Kimura,

T. Koi, H. Kurashige, A. Lechner, S. Lee, F. Longo, M. Maire, D. Mancusi, A. Mantero, E. Mendoza, B. Morgan, K. Murakami, T. Nikitina, L. Pandola, P. Paprocki, J. Perl, I. Petrović, M. Pia, W. Pokorski, J. Quesada, M. Raine, M. Reis, A. Ribon, A. R. Fira, F. Romano, G. Russo, G. Santin, T. Sasaki, D. Sawkey, J. Shin, I. Strakovsky, A. Taborda, S. Tanaka, B. Tomé, T. Toshito, H. Tran, P. Truscott, L. Urban, V. Uzhinsky, J. Verbeke, M. Verderi, B. Wendt, H. Wenzel, D. Wright, D. Wright, T. Yamashita, J. Yarba, and H. Yoshida. Recent developments in geant4. Nuclear Instruments and Methods in Physics Research Section A: Accelerators, Spectrometers, Detectors and Associated Equipment, 835:186 – 225, 2016.

[36] J. Alwall, R. Frederix, S. Frixione, V. Hirschi, F. Maltoni, O. Mattelaer, H.-S. Shao, T. Stelzer, P. Torrielli, and M. Zaro. The automated computation of tree-level and next-to-leading order differential cross sections, and their matching to parton shower simulations. Journal of High Energy Physics, 2014(7):79, Jul 2014.

[37] M. Andrieux, B. Belhorma, A. Belymam, D. Benchekroun, R. Cherkaoui, C. Clément, J. Collot, P. de Saintignon, C. Driouichi, D. Dzahini, Y. E. Mouahhidi, H. Erridi, A. Ferrari, H. Ghazlane, J. Hostachy, A. Hoummada, A. Idrissi, G. Laborie, B. Lund-Jensen, P. Martin, J. Muraz, and J. Söderqvist. Construction and test of the first two sectors of the atlas barrel liquid argon presampler. Nuclear Instruments and Methods in Physics Research Section A: Accelerators, Spectrometers, Detectors and Associated Equipment, 479(2):316 – 333, 2002.

[38] A. Artamonov, D. Bailey, G. Belanger, M. Cadabeschi, T. Y. Chen, V. Epshteyn, P. Gorbounov, K. K. Joo, M. Khakzad, V. Khovanskiy, P. Krieger, P. Loch, J. Mayer, E. Neuheimer, F. G. Oakham, M. O'Neill, R. S. Orr, M. Qi, J. Rutherfoord, A. Savine, M. Schram, P. Shatalov, L. Shaver, M. Shupe, G. Stairs, V. Strickland, D. Tompkins, I. Tsukerman, and K. Vincent. The atlas forward calorimeter. Journal of Instrumentation, 3(02):P02010, 2008.

[39] C. ATLAS, M. Beckingham, M. Duehrssen, E. Schmidt, M. Shapiro, M. Venturi, J. Virzi, I. Vivarelli, M. Werner, S. Yamamoto, and T. Yamanaka. The simulation principle and performance of the ATLAS fast calorimeter simulation FastCaloSim. Technical Report ATL-PHYS-PUB-2010-013, CERN, Geneva, Oct 2010.

[40] ATLAS Collaboration. Technical Design Report for the ATLAS Inner Tracker Strip Detector. Technical Report CERN-LHCC-2017-005. ATLAS-TDR-025, CERN, Geneva, Apr 2017.

[41] ATLAS Collaboration. Electron reconstruction and identification in the ATLAS experiment using the 2015 and 2016 LHC proton–proton collision data at $\sqrt{s}$ =13TeV. Technical Report ATL-COM-PHYS-2018-436, CERN, Geneva, Apr 2018.

[42] G. Avoni et al. The new lucid-2 detector for luminosity measurement and monitoring in atlas. JINST, 13(07):P07017, 2018.

[43] M. Bahr et al. Herwig++ Physics and Manual. Eur. Phys. J., C58:639–707, 2008.

[44] E. Barberio, J. Boudreau, B. Butler, S. L. Cheung, A. Dell'Acqua, A. D. Simone, E. Ehrenfeld, M. V. Gallas, A. Glazov, Z. Marshall, J. Mueller, R. Plačakyte, A. Rimoldi, P. Savard, V. Tsulaia, A. Waugh, and C. C. Young. Fast simulation of electromagnetic showers in the atlas calorimeter: Frozen showers. Journal of Physics: Conference Series, 160(1):012082, 2009.

[45] E. Barberio, J. Boudreau, B. Butler, S. L. Cheung, A. Dell'Acqua, A. D. Simone, W. Ehrenfeld, M. V. Gallas, A. Glazov, Z. Marshall, J. Mueller, R. Plačakytė, A. Rimoldi, P. Savard, V. Tsulaia, A. Waugh, and C. C. Young. Fast shower simulation in the atlas calorimeter. Journal of Physics: Conference Series, 119(3):032008, 2008.

[46] C. Barth et al. Enabling Technologies for Silicon Microstrip Tracking Detectors at the HL-LHC. 2016.

[47] F. Bauer et al. Construction and Test of the Precision Drift Chambers for the ATLAS Muon Spectrometer. IEEE Trans. Nucl. Sci., 48:302–307, 2001.

[48] U. BAUR, I. HINCHLIFFE, and D. ZEPPENFELD. Excited quark production at hadron colliders. International Journal of Modern Physics A, 02(04):1285–1297, 1987.

[49] J. Bellm et al. Herwig 7.0/Herwig++ 3.0 release note. Eur. Phys. J., C76(4):196, 2016.

[50] V. Benítez et al. Sensors for the End-cap prototype of the Inner Tracker in the ATLAS Detector Upgrade. Nucl. Instrum. Meth., A833:226–232, 2016.

[51] A. J. Blue et al. Test beam evaluation of silicon strip modules for ATLAS phase-II strip tracker upgrade. Nucl. Instrum. Meth., A924:108–111, 2019.

[52] A. Buckley, J. Ferrando, S. Lloyd, K. Nordström, B. Page, M. Rüfenacht, M. Schönherr, and G. Watt. Lhapdf6: parton density access in the lhc precision era. The European Physical Journal C, 75(3):132, Mar 2015.

[53] J. Butterworth et al. PDF4LHC recommendations for LHC Run II. J. Phys., G43:023001, 2016.

[54] M. Cacciari, G. P. Salam, and G. Soyez. The anti- k t jet clustering algorithm. Journal of High Energy Physics, 2008(04):063, 2008.

[55] S. Chatrchyan et al. Observation of a New Boson at a Mass of 125 GeV with the CMS Experiment at the LHC. Phys. Lett., B716:30–61, 2012.

[56] X. Cid Vidal et al. Beyond the Standard Model Physics at the HL-LHC and HE-LHC. Technical Report arXiv:1812.07831, CERN, Geneva, 2018. * Temporary entry *.

[57] F. Derue. Estimation of fake lepton background for top analyses using the Matrix Method with the 2015 dataset at $\sqrt{s}$=13 TeV with AnalysisTop-2.3.41. Technical Report ATL-COM-PHYS-2016-198, CERN, Geneva, Feb 2016.

[58] L. Evans and P. Bryant. LHC Machine. JINST, 3:S08001, 2008.

[59] S. Frixione, P. Nason, and C. Oleari. Matching NLO QCD computations with Parton Shower simulations: the POWHEG method. JHEP, 11:070, 2007.

[60] C. García Argos et al. Assembly and electrical tests of the first full-size forward module for the ATLAS ITk Strip detector. Nucl. Instrum. Meth., A924:112–115, 2019.

[61] D. M. Gingrich. Construction, assembly and testing of the atlas hadronic end-cap calorimeter. Journal of Instrumentation, 2(05):P05005, 2007.

[62] T. Gleisberg, S. Hoeche, F. Krauss, M. Schonherr, S. Schumann, F. Siegert, and J. Winter. Event generation with SHERPA 1.1. JHEP, 02:007, 2009.

[63] T. Golling, H. S. Hayward, P. U. E. Onyisi, H. J. Stelzer, and P. Waller. The ATLAS Data Quality Defect Database System. Eur. Phys. J., C72:1960, 2012.

[64] A. E. L. A. E. C. Group.

[65] V. Khachatryan et al. Search for the production of an excited bottom quark decaying to tW in proton-proton collisions at $\sqrt{s} = 8$ TeV. JHEP, 01:166, 2016.

[66] N. Kidonakis. Two-loop soft anomalous dimensions for single top quark associated production with a W- or H-. Phys. Rev., D82:054018, 2010.

[67] D. Krohn, J. Thaler, and L.-T. Wang. Jet trimming. Journal of High Energy Physics, 2010(2):84, Feb 2010.

[68] S. Kuehn et al. Prototyping of hybrids and modules for the forward silicon strip tracking detector for the ATLAS Phase-II upgrade. JINST, 12(05):P05015, 2017.

[69] S. Kuehn et al. Prototyping of petalets for the Phase-II Upgrade of the silicon strip tracking detector of the ATLAS Experiment. JINST, 13(03):T03004, 2018.

[70] H.-L. Lai, M. Guzzi, J. Huston, Z. Li, P. M. Nadolsky, J. Pumplin, and C. P. Yuan. New parton distributions for collider physics. Phys. Rev., D82:074024, 2010.

[71] B. Mindur. ATLAS Transition Radiation Tracker (TRT): Straw tubes for tracking and particle identification at the Large Hadron Collider. Technical Report ATL-INDET-PROC-2016-001, CERN, Geneva, Mar 2016.

[72] MissMJ, Dhatfield, Jackaranga, Dhatfield, L. Profil, Jcer80, ZooFari, AnonMoos, Duschi, Fatka, Sjlegg, Woz2, InverseHypercube, Dsperlich, Cush, and Nasfarley88. Standard model of elementary particles.svg, 2018.

[73] E. Mobs. The CERN accelerator complex. Complexe des accélérateurs du CERN. Jul 2016. General Photo.

[74] P. Nason. A New method for combining NLO QCD with shower Monte Carlo algorithms. JHEP, 11:040, 2004.

[75] J. E. G. Navarro and M. Kado. Atlasproductiongroupmc15a, 2016.

[76] J. W. Nutter, R. Schwienhorst, D. G. E. Walker, and J.-H. Yu. Single top production as a probe of $B^{'}$ quarks. Phys. Rev. D, 86:094006, Nov 2012.

[77] L. Poley et al. Alternative glues for the production of ATLAS silicon strip modules for the Phase-II upgrade of the ATLAS Inner Detector. JINST, 11(05):P05017, 2016.

[78] L. Poley et al. Characterisation of strip silicon detectors for the ATLAS Phase-II Upgrade with a micro-focused X-ray beam. JINST, 11(07):P07023, 2016.

[79] L. Poley et al. Investigations into the impact of locally modified sensor architectures on the detection efficiency of silicon micro-strip sensors. JINST, 12(07):P07006, 2017.

[80] L. Poley et al. Mapping the depleted area of silicon diodes using a micro-focused X-ray beam. JINST, 14(03):P03024, 2019.

[81] K. Potamianos. The upgraded Pixel detector and the commissioning of the Inner Detector tracking of the ATLAS experiment for Run-2 at the Large Hadron Collider. PoS, EPS-HEP2015:261, 2015.

[82] A. L. Read. Modified frequentist analysis of search results (the CL_s method). Technical Report CERN-OPEN-2000-205, 2000.

[83] J. Schaarschmidt. The new ATLAS Fast Calorimeter Simulation. Technical Report ATL-SOFT-PROC-2017-005. 4, CERN, Geneva, Jan 2017.

[84] T. Sjöstrand, S. Ask, J. R. Christiansen, R. Corke, N. Desai, P. Ilten, S. Mrenna, S. Prestel, C. O. Rasmussen, and P. Z. Skands. An Introduction to PYTHIA 8.2. Comput. Phys. Commun., 191:159–177, 2015.

[85] D. Sperlich. Strip detector for the ATLAS detector upgrade for the high - luminosity LHC. In Proceedings, 2016 IEEE Nuclear Science Symposium and Medical Imaging Conference: NSS/MIC 2016: Strasbourg, France, page 8069684, 2016.

[86] D. Sperlich, L. Poley, I. Bloch, A. J. Blue, C. Buttar, V. Fadeyev, C. Gray, H. Lacker, L. Rehnisch, and M. Stegler. Signals from fluorescent materials on the surface of silicon micro-strip sensors. Nucl. Instrum. Meth., A924:125–127, 2019.

[87] M. Tanabashi et al. Review of particle physics. Phys. Rev. D, 98:030001, Aug 2018.

[88] S. Tanaka, H. Ohshita, K. Ishii, H. Iwasaki, Y. Arataki, T. Bando, Y. Homma, M. Ishino, T. Kondo, T. Kobayashi, H. Kurashige, G. Mikenberg, Y. Miyazaki, Y. Nakagawa, H. Nanjo, M. Ikeno, M. Nozaki, A. Ochi, O. Sasaki, and C. Yokoyama. Techniques developed for the atlas thin gap chambers mass production in japan. Nuclear Science, IEEE Transactions on, 51:934 – 938, 07 2004.

[89] The ATLAS collaboration. Operation and performance of the atlas semiconductor tracker. Journal of Instrumentation, 9(08):P08009, 2014.

[90] The ATLAS TRT collaboration . The ATLAS TRT Barrel Detector. Journal of Instrumentation, 3(02):P02014, 2008.

[91] The ATLAS TRT collaboration. The atlas transition radiation tracker (trt) proportional drift tube: design and performance. Journal of Instrumentation, 3(02):P02013, 2008.

[92] The ATLAS TRT collaboration. The ATLAS TRT end-cap detectors. Journal of Instrumentation, 3(10):P10003, 2008.

[93] The NNPDF collaboration, R. D. Ball, V. Bertone, S. Carrazza, C. S. Deans, L. Del Debbio, S. Forte, A. Guffanti, N. P. Hartland, J. I. Latorre, J. Rojo, and M. Ubiali. Parton distributions for the lhc run ii. Journal of High Energy Physics, 2015(4):40, Apr 2015.

[94] G. Unal and L. Fiorini. Atlas experiment – public results – luminosity-publicresults, 2013.

[95] M. Veltman. Diagrammatica - The path to Feynman Diagrams. Cambridge University Press, 1 edition, 1994.

[96] H. Wilkens and the ATLAS LArg Collaboration. The atlas liquid argon calorimeter: An overview. Journal of Physics: Conference Series, 160(1):012043, 2009.

[97] J. Wotschack. ATLAS Muon Chamber Construction Parameters for CSC, MDT, and RPC chambers. Technical Report ATL-MUON-PUB-2008-006. ATL-COM-MUON-2008-008, CERN, Geneva, Apr 2008. Back-up document for the ATLAS Detector Paper.

Appendix A

Standard Model background samples

Process	Sample name	cross section [pb]	k-factor	filter eff.
$t\bar{t}$ pair	PowhegPythia8EvtGen_A14_ttbar_hdamp258p75_nonallhad			
W + radiation	Sherpa_221_NNPDF30NNLO_Wmunu_MAXHTPTV0_70_BFilter	19135.0	0.9702	0.044118
	Sherpa_221_NNPDF30NNLO_Wmunu_MAXHTPTV70_140_BFilter	944.63	0.9702	0.075648
	Sherpa_221_NNPDF30NNLO_Wmunu_MAXHTPTV140_280_BFilter	339.54	0.9702	0.10872
	Sherpa_221_NNPDF30NNLO_Wmunu_MAXHTPTV280_500_BFilter	72.045	0.9702	0.13337
	Sherpa_221_NNPDF30NNLO_Wmunu_MAXHTPTV1000_E_CMS	1.2344	0.9702	1.0
	Sherpa_221_NNPDF30NNLO_Wenu_MAXHTPTV70_140_BFilter	945.15	0.9702	0.10341
	Sherpa_221_NNPDF30NNLO_Wenu_MAXHTPTV280_500_BFilter	72.113	0.9702	0.13391
	Sherpa_221_NNPDF30NNLO_Wenu_MAXHTPTV1000_E_CMS	1.2334	0.9702	1.0
	Sherpa_221_NNPDF30NNLO_Wtaunu_MAXHTPTV0_70_BFilter	19163.0	0.9702	0.044594
	Sherpa_221_NNPDF30NNLO_Wtaunu_MAXHTPTV70_140_BFilter	943.30	0.9702	0.10396
	Sherpa_221_NNPDF30NNLO_Wtaunu_MAXHTPTV140_280_BFilter	339.54	0.9702	0.11799
	Sherpa_221_NNPDF30NNLO_Wtaunu_MAXHTPTV280_500_BFilter	72.026	0.9702	0.13426
	Sherpa_221_NNPDF30NNLO_Wtaunu_MAXHTPTV1000_E_CMS	1.2339	0.9702	1.0
	Sherpa_221_NNPDF30NNLO_Wmunu_MAXHTPTV0_70_CFilterBVeto	19121.0	0.9702	0.1304
	Sherpa_221_NNPDF30NNLO_Wmunu_MAXHTPTV140_280_CFilterBVeto	340.06	0.9702	0.28947
	Sherpa_221_NNPDF30NNLO_Wmunu_MAXHTPTV280_500_CFilterBVeto	72.198	0.9702	0.31743
	Sherpa_221_NNPDF30NNLO_Wenu_MAXHTPTV0_70_CFilterBVeto	19130.0	0.9702	0.1303
	Sherpa_221_NNPDF30NNLO_Wenu_MAXHTPTV70_140_CFilterBVeto	945.67	0.9702	0.22787
	Sherpa_221_NNPDF30NNLO_Wenu_MAXHTPTV140_280_CFilterBVeto	339.87	0.9702	0.28965
	Sherpa_221_NNPDF30NNLO_Wenu_MAXHTPTV280_500_CFilterBVeto	72.128	0.9702	0.31675
	Sherpa_221_NNPDF30NNLO_Wtaunu_MAXHTPTV0_70_CFilterBVeto	19153.0	0.9702	0.12934
	Sherpa_221_NNPDF30NNLO_Wtaunu_MAXHTPTV70_140_CFilterBVeto	946.73	0.9702	0.22222
	Sherpa_221_NNPDF30NNLO_Wtaunu_MAXHTPTV140_280_CFilterBVeto	339.63	0.9702	0.29025
	Sherpa_221_NNPDF30NNLO_Wtaunu_MAXHTPTV280_500_CFilterBVeto	71.976	0.9702	0.31648

	Sherpa_221_NNPDF30NNLO_Wmunu_MAXHTPTV0_70_CVetoBVeto	19143.0	0.9702	0.8238
	Sherpa_221_NNPDF30NNLO_Wmunu_MAXHTPTV70_140_CVetoBVeto	944.85	0.9702	0.67463
	Sherpa_221_NNPDF30NNLO_Wmunu_MAXHTPTV140_280_CVetoBVeto	339.54	0.9702	0.62601
	Sherpa_221_NNPDF30NNLO_Wmunu_MAXHTPTV280_500_CVetoBVeto	72.067	0.9702	0.54647
	Sherpa_221_NNPDF30NNLO_Wenu_MAXHTPTV0_70_CVetoBVeto	19127.0	0.9702	0.82447
	Sherpa_221_NNPDF30NNLO_Wenu_MAXHTPTV70_140_CVetoBVeto	942.58	0.9702	0.66872
	Sherpa_221_NNPDF30NNLO_Wenu_MAXHTPTV140_280_CVetoBVeto	339.81	0.9702	0.59691
	Sherpa_221_NNPDF30NNLO_Wenu_MAXHTPTV280_500_CVetoBVeto	72.084	0.9702	0.54441
	Sherpa_221_NNPDF30NNLO_Wtaunu_MAXHTPTV0_70_CVetoBVeto	19152.0	0.9702	0.82495
	Sherpa_221_NNPDF30NNLO_Wtaunu_MAXHTPTV70_140_CVetoBVeto	947.65	0.9702	0.67382
	Sherpa_221_NNPDF30NNLO_Wtaunu_MAXHTPTV140_280_CVetoBVeto	339.36	0.9702	0.59622
	Sherpa_221_NNPDF30NNLO_Wtaunu_MAXHTPTV280_500_CVetoBVeto	72.065	0.9202	0.54569
	Sherpa_221_NNPDF30NNLO_Wenu_MAXHTPTV0_70_BFilter	19135.0	0.9702	0.044141
	Sherpa_221_NNPDF30NNLO_Wmunu_MAXHTPTV70_140_CFilterBVeto	937.78	0.9702	0.23456
	Sherpa_221_NNPDF30NNLO_Wmunu_MAXHTPTV500_1000	15.01	0.9702	1.0
	Sherpa_221_NNPDF30NNLO_Wenu_MAXHTPTV140_280_BFilter	339.48	0.9702	0.10898
	Sherpa_221_NNPDF30NNLO_Wenu_MAXHTPTV500_1000	15.224	0.9702	1.0
	Sherpa_221_NNPDF30NNLO_Wtaunu_MAXHTPTV500_1000	15.046	0.9702	1.0
single t quark	PowhegPythiaEvtGen_P2012_singletop_tchan_lept_top	43.739	1.0094	1.0
	PowhegPythiaEvtGen_P2012_singletop_tchan_lept_antitop	25.778	1.0193	1.0
	PowhegPythiaEvtGen_P2012_Wt_inclusive_top	34.009	1.054	1.0
	PowhegPythiaEvtGen_P2012_Wt_inclusive_antitop	33.989	1.054	1.0
	PowhegPythiaEvtGen_P2012_SingleTopSchan_noAllHad_top	2.0517	1.0046	1.0
	PowhegPythiaEvtGen_P2012_SingleTopSchan_noAllHad_antitop	1.2615	1.0215	1.0
Z boson	Sherpa_221_NNPDF30NNLO_Zmumu_MAXHTPTV0_70_BFilter	1982.2	0.9751	0.064161
	Sherpa_221_NNPDF30NNLO_Zmumu_MAXHTPTV70_140_BFilter	108.91	0.9751	0.11375
	Sherpa_221_NNPDF30NNLO_Zmumu_MAXHTPTV140_280_BFilter	39.901	0.9751	0.14772

Sherpa_221_NNPDF30NNLO_Zmumu_MAXHTPTV280_500_BFilter	8.4932	0.9751	0.17559
Sherpa_221_NNPDF30NNLO_Zmumu_MAXHTPTV500_1000	1.7881	0.9751	1.0
Sherpa_221_NNPDF30NNLO_Zmumu_MAXHTPTV1000_E_CMS	0.14769	0.9751	
Sherpa_221_NNPDF30NNLO_Zee_MAXHTPTV0_70_BFilter	1981.7	0.9751	0.063809
Sherpa_221_NNPDF30NNLO_Zee_MAXHTPTV70_140_BFilter	110.31	0.9751	0.11443
Sherpa_221_NNPDF30NNLO_Zee_MAXHTPTV140_280_BFilter	40.643	0.9751	0.14966
Sherpa_221_NNPDF30NNLO_Zee_MAXHTPTV280_500_BFilter	8.6766	0.9751	0.17223
Sherpa_221_NNPDF30NNLO_Zee_MAXHTPTV500_1000	1.8081	0.9751	1.0
Sherpa_221_NNPDF30NNLO_Zee_MAXHTPTV1000_E_CMS	0.14857	0.9751	1.0
Sherpa_221_NNPDF30NNLO_Ztautau_MAXHTPTV0_70_BFilter	1981.8	0.9751	0.064453
Sherpa_221_NNPDF30NNLO_Ztautau_MAXHTPTV70_140_BFilter	110.87	0.9751	0.110886
Sherpa_221_NNPDF30NNLO_Ztautau_MAXHTPTV140_280_BFilter	40.761	0.9751	0.13442
Sherpa_221_NNPDF30NNLO_Ztautau_MAXHTPTV280_500_BFilter	8.6804	0.9751	0.17313
Sherpa_221_NNPDF30NNLO_Ztautau_MAXHTPTV500_1000	1.8096	0.9751	1.0
Sherpa_221_NNPDF30NNLO_Ztautau_MAXHTPTV1000_E_CMS	0.14834	0.9751	1.0
Sherpa_221_NNPDF30NNLO_Zmumu_MAXHTPTV0_70_CFilterBVeto	1978.4	0.9751	0.11308
Sherpa_221_NNPDF30NNLO_Zmumu_MAXHTPTV70_140_CFilterBVeto	109.42	0.9751	0.18596
Sherpa_221_NNPDF30NNLO_Zmumu_MAXHTPTV140_280_CFilterBVeto	39.795	0.9751	0.23308
Sherpa_221_NNPDF30NNLO_Zmumu_MAXHTPTV280_500_CFilterBVeto	8.5403	0.9751	0.26528
Sherpa_221_NNPDF30NNLO_Zee_MAXHTPTV0_70_CFilterBVeto	1980.8	0.9751	0.11295
Sherpa_221_NNPDF30NNLO_Zee_MAXHTPTV70_140_CFilterBVeto	110.63	0.9751	0.18382
Sherpa_221_NNPDF30NNLO_Zee_MAXHTPTV140_280_CFilterBVeto	40.67	0.9751	0.23044
Sherpa_221_NNPDF30NNLO_Zee_MAXHTPTV280_500_CFilterBVeto	8.6711	0.9751	0.26294
Sherpa_221_NNPDF30NNLO_Ztautau_MAXHTPTV0_70_CFilterBVeto	1978.8	0.9751	0.11314
Sherpa_221_NNPDF30NNLO_Ztautau_MAXHTPTV70_140_CFilterBVeto	110.51	0.9751	0.1829
Sherpa_221_NNPDF30NNLO_Ztautau_MAXHTPTV140_280_CFilterBVeto	40.74	0.9751	0.22897
Sherpa_221_NNPDF30NNLO_Ztautau_MAXHTPTV280_500_CFilterBVeto	8.6707	0.9751	0.26245

	Sherpa_221_NNPDF30NNLO_Zmumu_MAXHTPTV0_70_CVetoBVeto	1983.0	0.9751	0.8221
	Sherpa_221_NNPDF30NNLO_Zmumu_MAXHTPTV70_140_CVetoBVeto	108.92	0.9751	0.68873
	Sherpa_221_NNPDF30NNLO_Zmumu_MAXHTPTV140_280_CVetoBVeto	39.878	0.9751	0.60899
	Sherpa_221_NNPDF30NNLO_Zmumu_MAXHTPTV280_500_CVetoBVeto	8.5375	0.9751	0.55906
	Sherpa_221_NNPDF30NNLO_Zee_MAXHTPTV0_70_CVetoBVeto	1981.8	0.9751	0.82106
	Sherpa_221_NNPDF30NNLO_Zee_MAXHTPTV70_140_CVetoBVeto	110.5	0.9751	0.69043
	Sherpa_221_NNPDF30NNLO_Zee_MAXHTPTV140_280_CVetoBVeto	40.731	0.9751	0.61452
	Sherpa_221_NNPDF30NNLO_Zee_MAXHTPTV280_500_CVetoBVeto	8.6743	0.9751	0.56134
	Sherpa_221_NNPDF30NNLO_Ztautau_MAXHTPTV0_70_CVetoBVeto	1981.6	0.9751	0.82142
	Sherpa_221_NNPDF30NNLO_Ztautau_MAXHTPTV70_140_CVetoBVeto	110.37	0.9751	0.68883
	Sherpa_221_NNPDF30NNLO_Ztautau_MAXHTPTV140_280_CVetoBVeto	40.781	0.9751	0.60821
	Sherpa_221_NNPDF30NNLO_Ztautau_MAXHTPTV280_500_CVetoBVeto	8.5502	0.9751	0.56036
Multiboson	Sherpa_CT10_llll	12.583	0.91	1.0
	Sherpa_CT10_lllvSFMinus	1.8446	0.91	1.0
	Sherpa_CT10_lllvOFMinus	3.6235	0.91	1.0
	Sherpa_CT10_lllvSFPlus	2.5656	0.91	1.0
	Sherpa_CT10_lllvOFPlus	5.0169	0.91	1.0
	Sherpa_CT10_llvv	14.022	0.91	1.0
	Sherpa_CT10_llvvjj_ss_EW6	0.043375	0.91	1.0
	Sherpa_CT10_lllvjj_EW6	0.042017	0.91	1.0
	Sherpa_CT10_llljj_EW6	0.1279	0.91	1.0
	Sherpa_CT10_WplvWmqq	25.995	0.91	1.0
	Sherpa_CT10_WpqqWmlv	25.974	0.91	1.0
	Sherpa_CT10_WlvZqq	12.543	0.91	1.0
	Sherpa_CT10_WqqZll	3.7583	0.91	1.0
	Sherpa_CT10_WqqZvv	7.4151	0.91	1.0
	Sherpa_CT10_ZqqZll	16.59	0.91	0.14253

Appendix B

Notable systematics

B.1 Additional control plots of the fits

B.1.1 Background only fit in control regions

The main part only shows the pulls of the systematic uncertainties with at least 1% of influence on the result. This comes from a pruning step, where all other systematics are pruned away. As the plot showing the pruning is quite big, it is recommended to refer to the digital copy of this thesis to be able to zoom into the figure B.1.

B.2 Selected systematics in all regions

Some systematics were pulled and or constrained in the nuisance parameters obtained by the signal + background fit in the control region before unblinding. To make sure this is not caused by random fluctuations, all pulled or constrained systmatics are shown in this appendix chapter. The conclusions of each plot are given in the associated caption.

The systematics on the fake muon and electron uncertainty are flat 100% uncertainties and due to the non ideal fit of fakes to data, a pull in these systematics was expected. Also the constraint is perfectly expected as the 100% uncertainty was a maximally conservative guess.

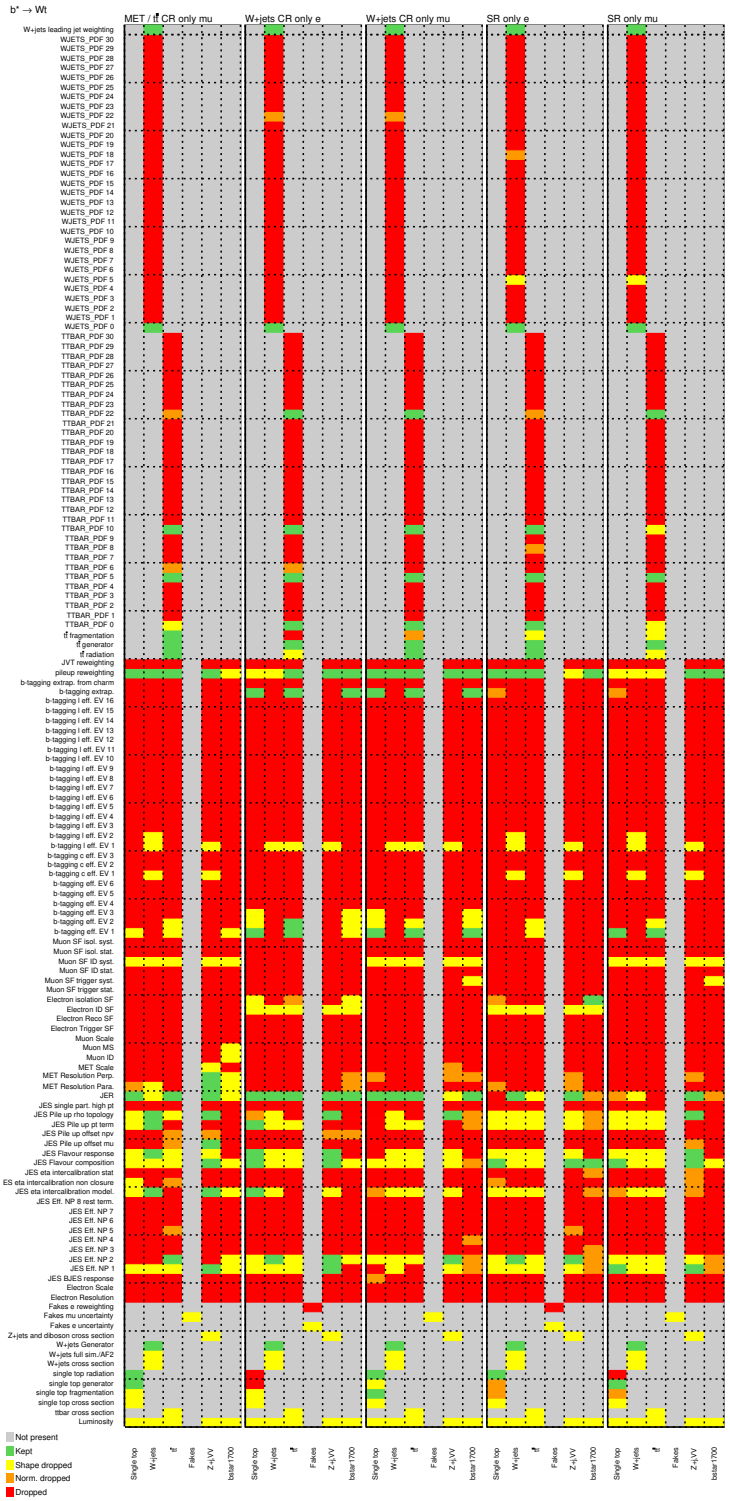

Figure B.1: Pruning of the nuisance parameters from a fit of only background samples in the control regions.

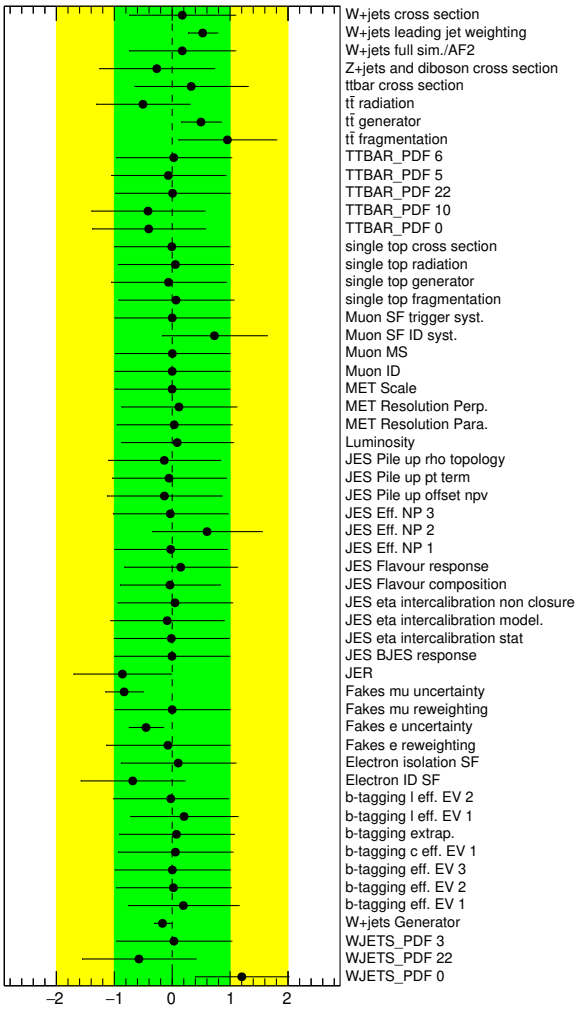

Figure B.2: Nuisance parameter plot showing the systematic pulls and constraints after a fit with data in the control regions and blinded signal region.

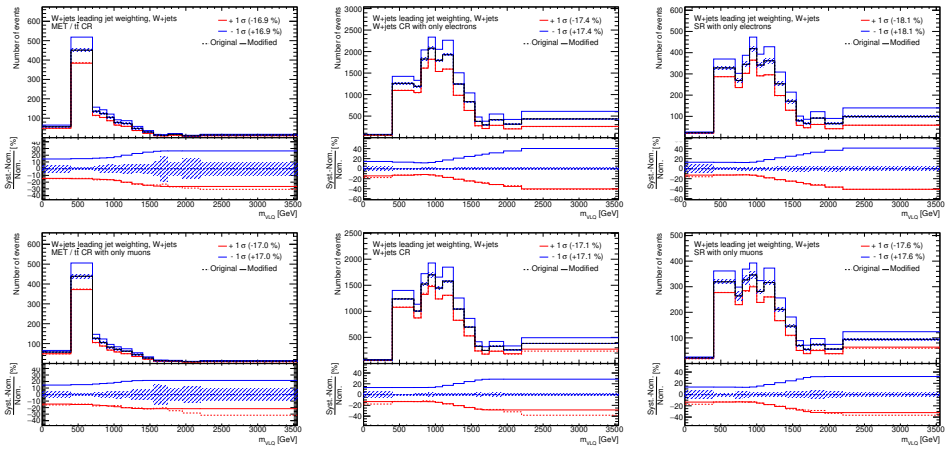

Figure B.3: W+jets leading jet reweighting systematics. These systematics are quite large and it is expected that these are pulled, because these systematics were introduced specifically to deal with a modeling problem in the W+jet samples for high p_T jets as described in section 6.1.2.

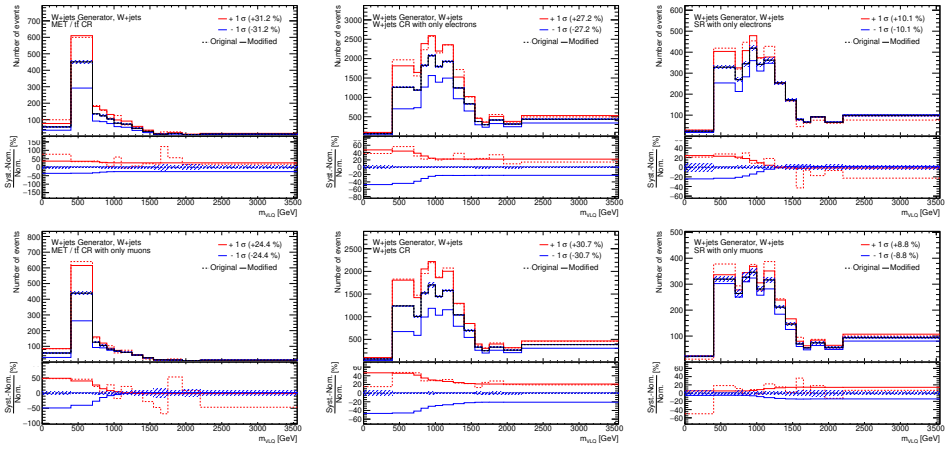

Figure B.4: W+jets generator systematics. These systematics are quite large and are obtained by comparing the nominal MC generators Sherpa 2.2.1 with the alternative generator Madgraph + Pythia 8. Therefore, the uncertainty is, by construction, not a $1\,\sigma$ variation and thus a strong constraint is expected. This is especially true, as we have a relatively pure W+jets control region.

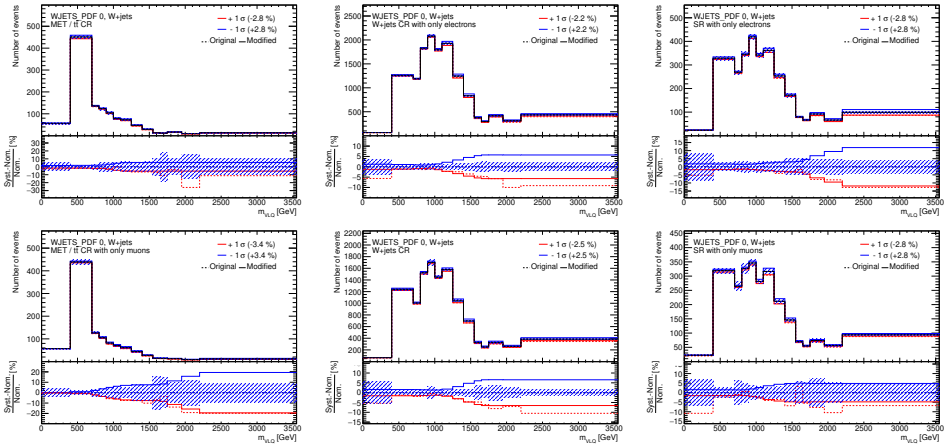

Figure B.5: W+jets PDF systematics, variation 0. This PDF systematic is not actually a PDF systematic but rather a second generator systematic. Therefore, it is expected to behave similar to the actual W+jets generator systematic. Also this uncertainty is again not a $1\,\sigma$ variation and a constraint is expected.

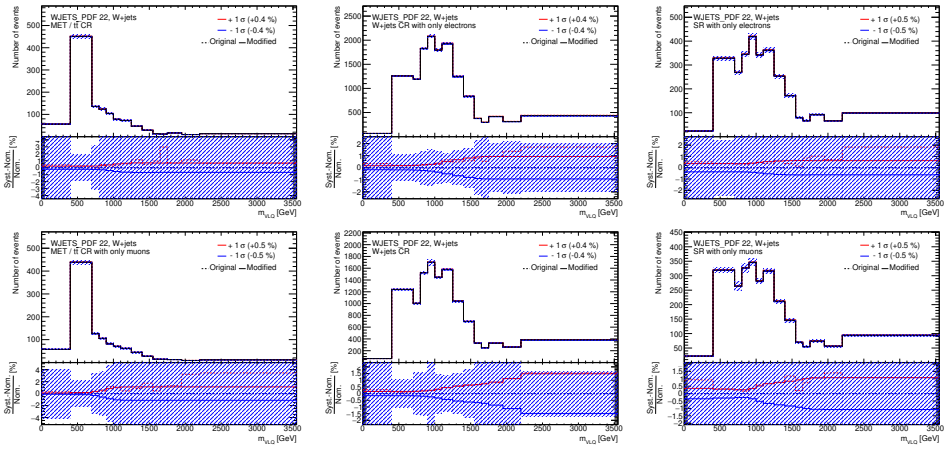

Figure B.6: W+jets PDF systematics, variation 2. This PDF systematic one of 30 different variations of a PDF as distributed by the authors of the PDF. This systematic is quite small, the smoothed up and down systematic is actually smooth and looks compatible with the unsmoothed systematic.

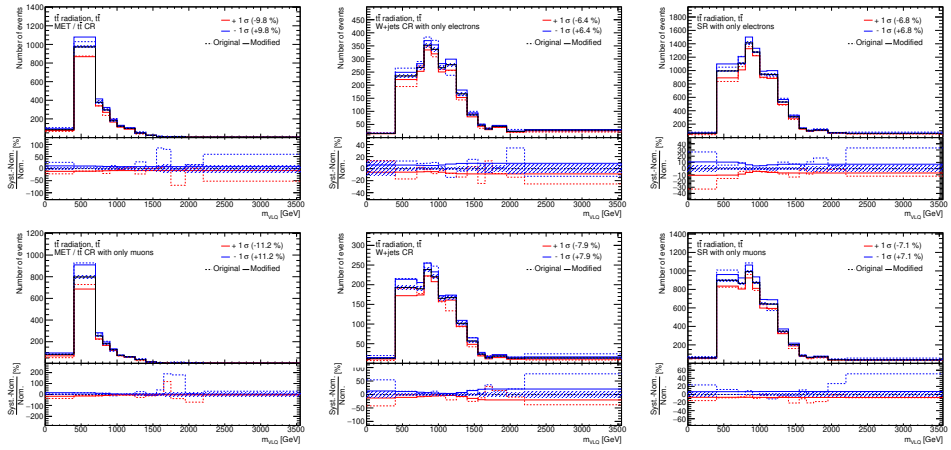

Figure B.7: $t\bar{t}$ radiation systematic. Even though they are not very small, the smoothed up and down systematic is actually smooth and looks compatible with the unsmoothed systematic.

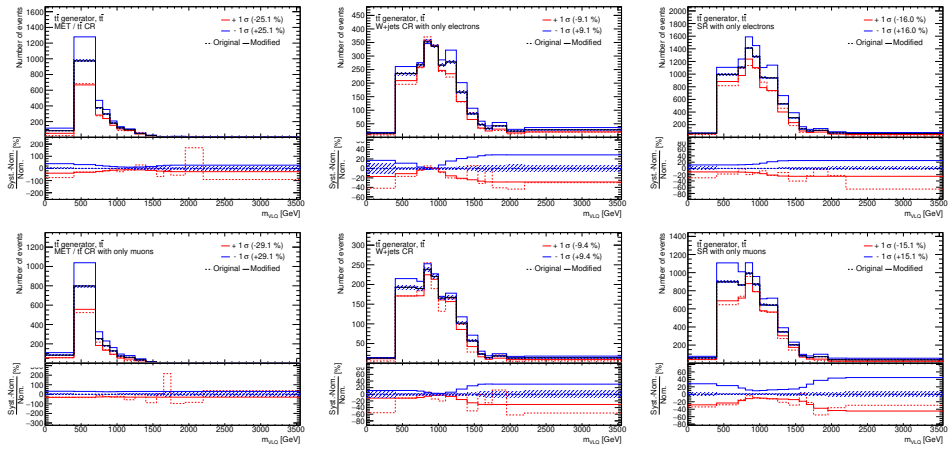

Figure B.8: $t\bar{t}$ generator systematic. Even though they are not very small, the smoothed up and down systematic is actually smooth and looks compatible with the unsmoothed systematic.

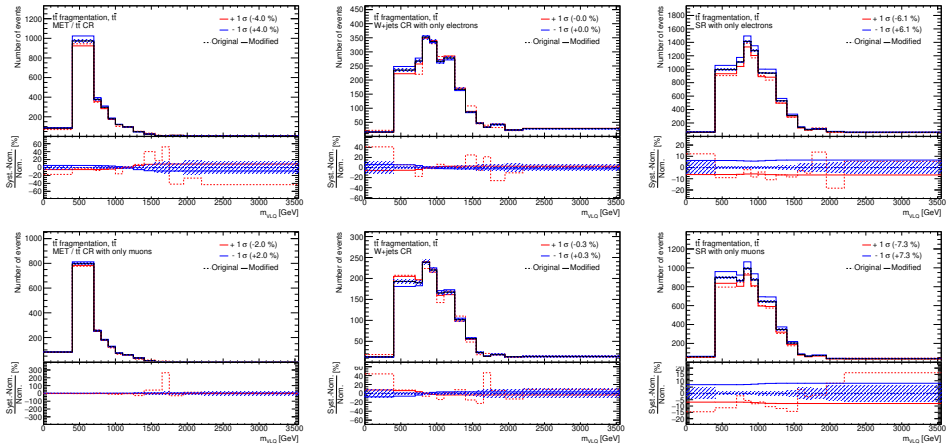

Figure B.9: $t\bar{t}$ fragmentation systematic. These systematics are smaller than the other $t\bar{t}$ systemtics and the smoothed up and down systematic is actually smooth and looks compatible with the unsmoothed systematic.

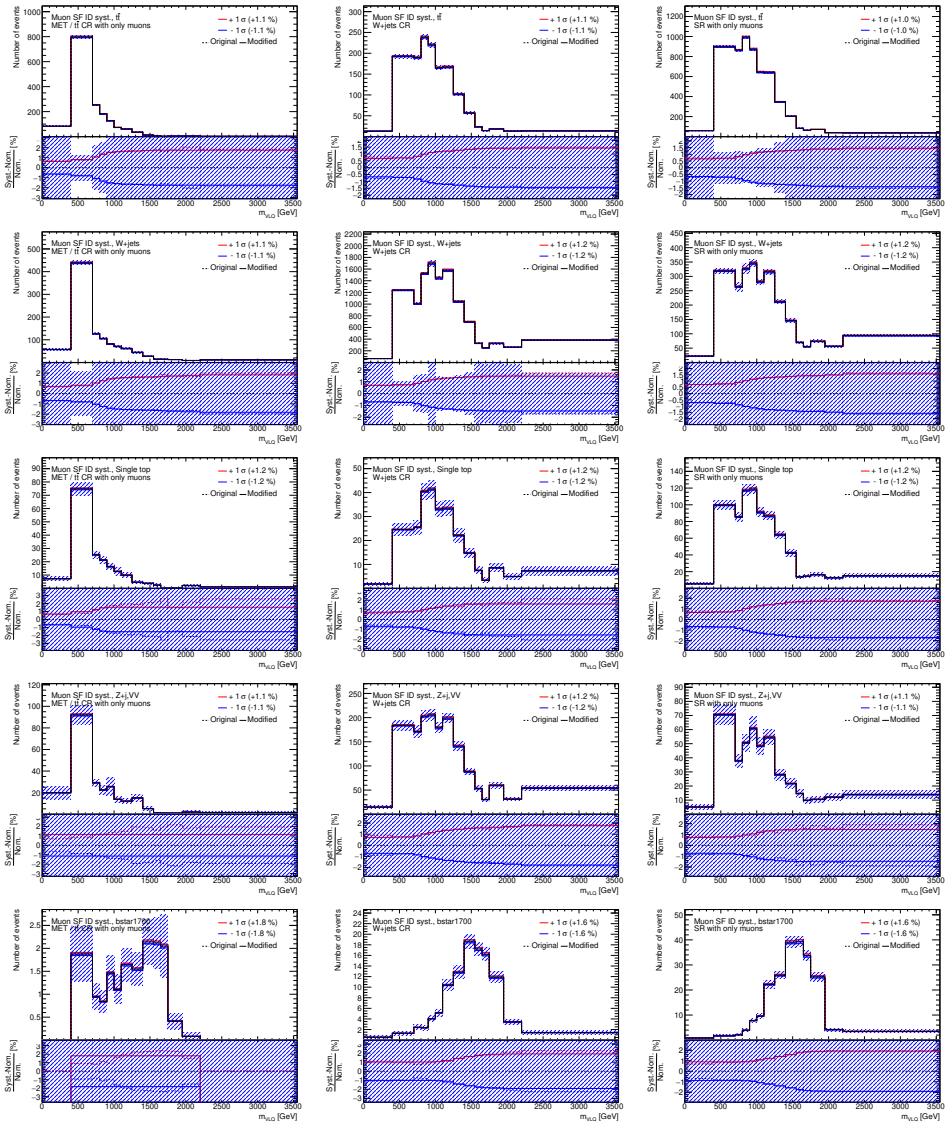

Figure B.10: Muon scalefactor identification systematic. The systematic is relativly small and the smoothed up and down systematic is actually smooth and looks perfectly compatible with the unsmoothed systematic.

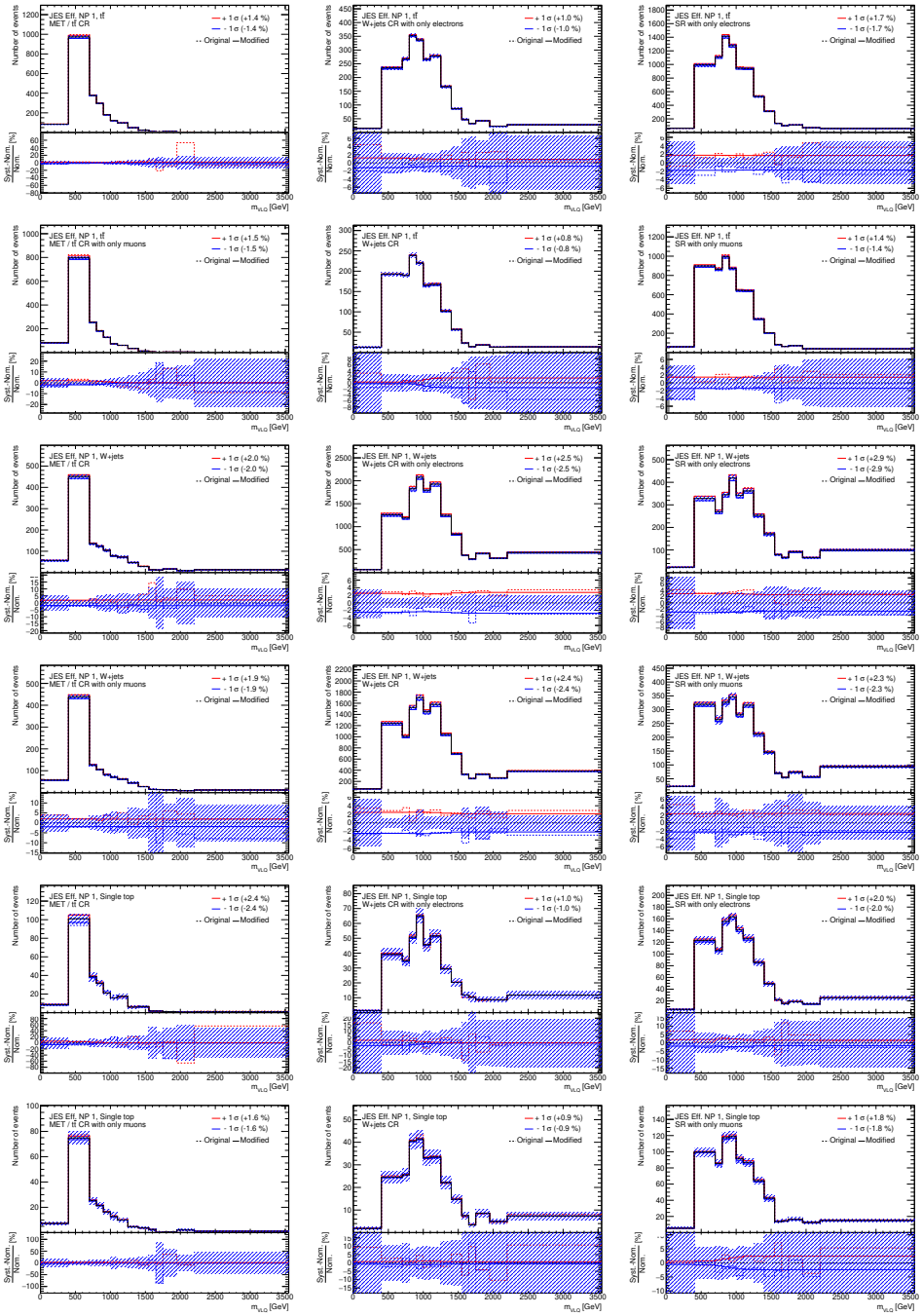
JES Eff, NP 1, tf
MET / tf CR
+ 1 σ (+1.4 %)
- 1 σ (-1.4 %)
Original
Modified
Number of events
Syst.-Nom. [%]
Nom.
$m_{\ell\ell\ell}$ [GeV]
JES Eff, NP 1, tf
W+jets CR with only electrons
+ 1 σ (+1.0 %)
- 1 σ (-1.0 %)
JES Eff, NP 1, tf
SR with only electrons
+ 1 σ (+1.7 %)
- 1 σ (-1.7 %)
JES Eff, NP 1, tf
MET / tf CR with only muons
+ 1 σ (+1.5 %)
- 1 σ (-1.5 %)
JES Eff, NP 1, tf
W+jets CR
+ 1 σ (+0.8 %)
- 1 σ (-0.8 %)
JES Eff, NP 1, tf
SR with only muons
+ 1 σ (+1.4 %)
- 1 σ (-1.4 %)
JES Eff, NP 1, W+jets
MET / tf CR
+ 1 σ (+2.0 %)
- 1 σ (-2.0 %)
JES Eff, NP 1, W+jets
W+jets CR with only electrons
+ 1 σ (+2.5 %)
- 1 σ (-2.5 %)
JES Eff, NP 1, W+jets
SR with only electrons
+ 1 σ (+2.9 %)
- 1 σ (-2.9 %)
JES Eff, NP 1, W+jets
MET / tf CR with only muons
+ 1 σ (+1.9 %)
- 1 σ (-1.9 %)
JES Eff, NP 1, W+jets
W+jets CR
+ 1 σ (+2.4 %)
- 1 σ (-2.4 %)
JES Eff, NP 1, W+jets
SR with only muons
+ 1 σ (+2.3 %)
- 1 σ (-2.3 %)
JES Eff, NP 1, Single top
MET / tf CR
+ 1 σ (+2.4 %)
- 1 σ (-2.4 %)
JES Eff, NP 1, Single top
W+jets CR with only electrons
+ 1 σ (+1.0 %)
- 1 σ (-1.0 %)
JES Eff, NP 1, Single top
SR with only electrons
+ 1 σ (+2.0 %)
- 1 σ (-2.0 %)
JES Eff, NP 1, Single top
MET / tf CR with only muons
+ 1 σ (+1.6 %)
- 1 σ (-1.6 %)
JES Eff, NP 1, Single top
W+jets CR
+ 1 σ (+0.9 %)
- 1 σ (-0.9 %)
JES Eff, NP 1, Single top
SR with only muons
+ 1 σ (+1.8 %)
- 1 σ (-1.8 %)

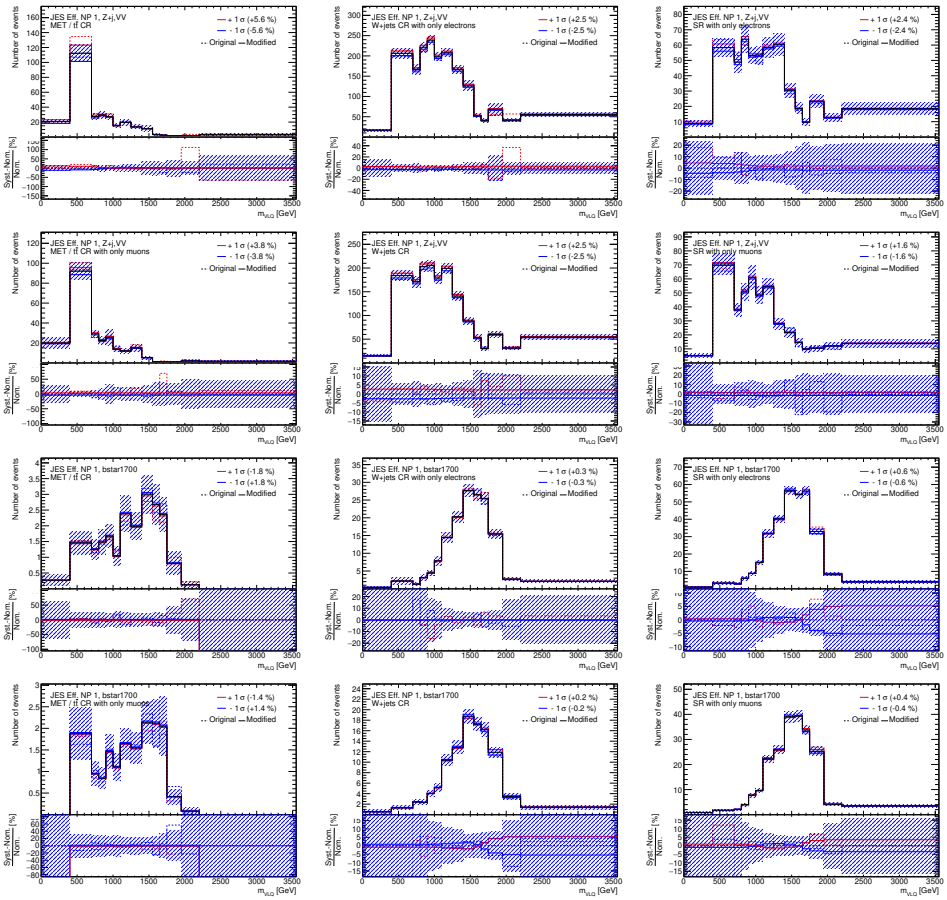

Figure B.11: Nuisance paramter 1 of jet energy scale (JES) systematic. This systematic is neither pulled nor constrained much, but one would expect it to be more likely pulled or constrained than the NP2 of the JES systematic. But the smoothed up and down systematic is actually smooth and looks compatible with the unsmoothed systematic.

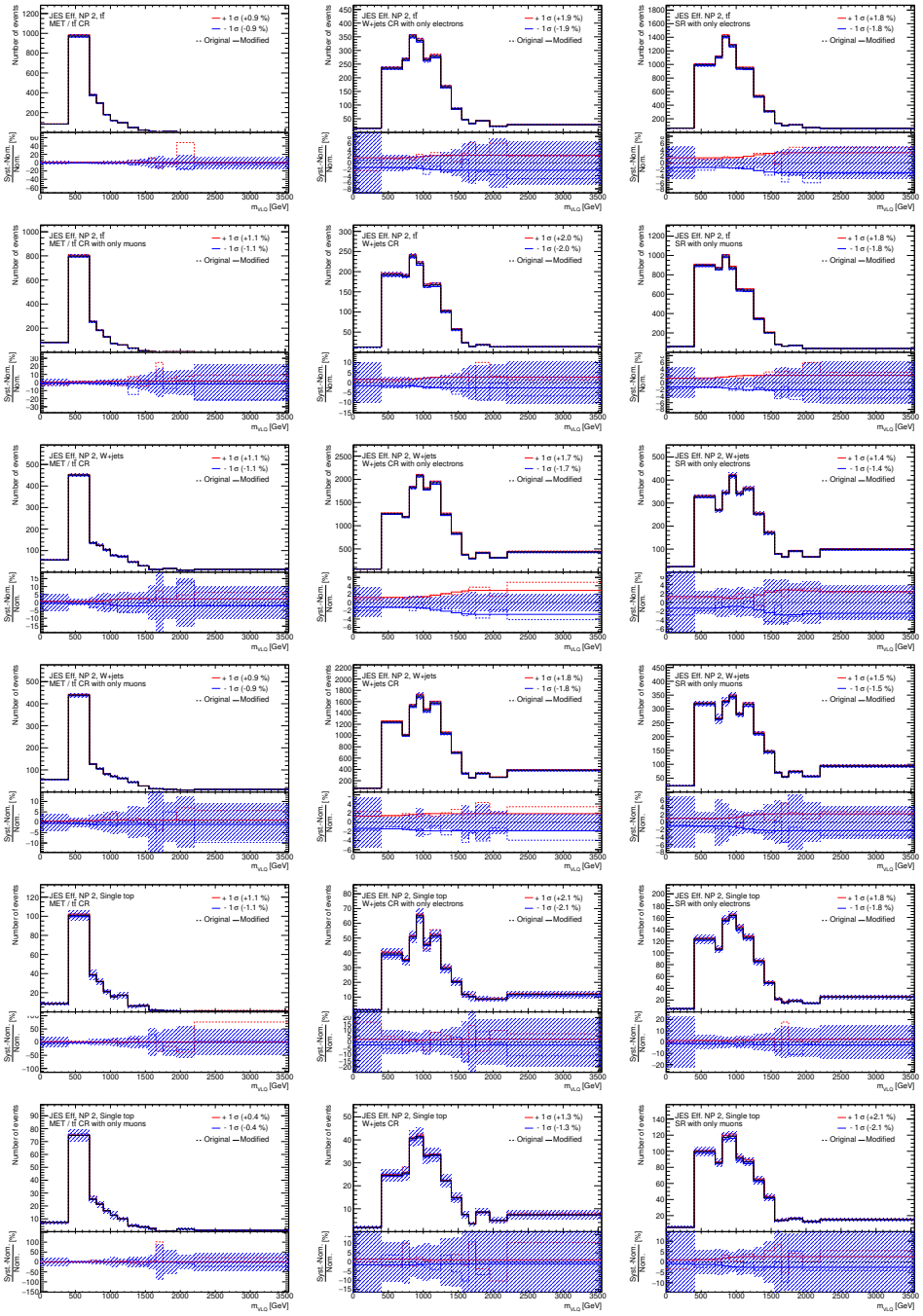
JES Eff, NP 2, tf
MET / tf CR
+ 1 σ (+0.9 %)
- 1 σ (-0.9 %)
Original
Modified
Number of events
Syst.-Nom. [%]
Nom.
m_{VLQ} [GeV]
JES Eff, NP 2, tf
W+jets CR with only electrons
+ 1 σ (+1.9 %)
- 1 σ (-1.9 %)
JES Eff, NP 2, tf
SR with only electrons
+ 1 σ (+1.8 %)
- 1 σ (-1.8 %)
JES Eff, NP 2, tf
MET / tf CR with only muons
+ 1 σ (+1.1 %)
- 1 σ (-1.1 %)
JES Eff, NP 2, tf
W+jets CR
+ 1 σ (+2.0 %)
- 1 σ (-2.0 %)
JES Eff, NP 2, tf
SR with only muons
+ 1 σ (+1.8 %)
- 1 σ (-1.8 %)
JES Eff, NP 2, W+jets
MET / tf CR
+ 1 σ (+1.1 %)
- 1 σ (-1.1 %)
JES Eff, NP 2, W+jets
W+jets CR with only electrons
+ 1 σ (+1.7 %)
- 1 σ (-1.7 %)
JES Eff, NP 2, W+jets
SR with only electrons
+ 1 σ (+1.4 %)
- 1 σ (-1.4 %)
JES Eff, NP 2, W+jets
MET / tf CR with only muons
+ 1 σ (+0.9 %)
- 1 σ (-0.9 %)
JES Eff, NP 2, W+jets
W+jets CR
+ 1 σ (+1.8 %)
- 1 σ (-1.8 %)
JES Eff, NP 2, W+jets
SR with only muons
+ 1 σ (+1.5 %)
- 1 σ (-1.5 %)
JES Eff, NP 2, Single top
MET / tf CR
+ 1 σ (+1.1 %)
- 1 σ (-1.1 %)
JES Eff, NP 2, Single top
W+jets CR with only electrons
+ 1 σ (+2.1 %)
- 1 σ (-2.1 %)
JES Eff, NP 2, Single top
SR with only electrons
+ 1 σ (+1.8 %)
- 1 σ (-1.8 %)
JES Eff, NP 2, Single top
MET / tf CR with only muons
+ 1 σ (+0.4 %)
- 1 σ (-0.4 %)
JES Eff, NP 2, Single top
W+jets CR
+ 1 σ (+1.3 %)
- 1 σ (-1.3 %)
JES Eff, NP 2, Single top
SR with only muons
+ 1 σ (+2.1 %)
- 1 σ (-2.1 %)

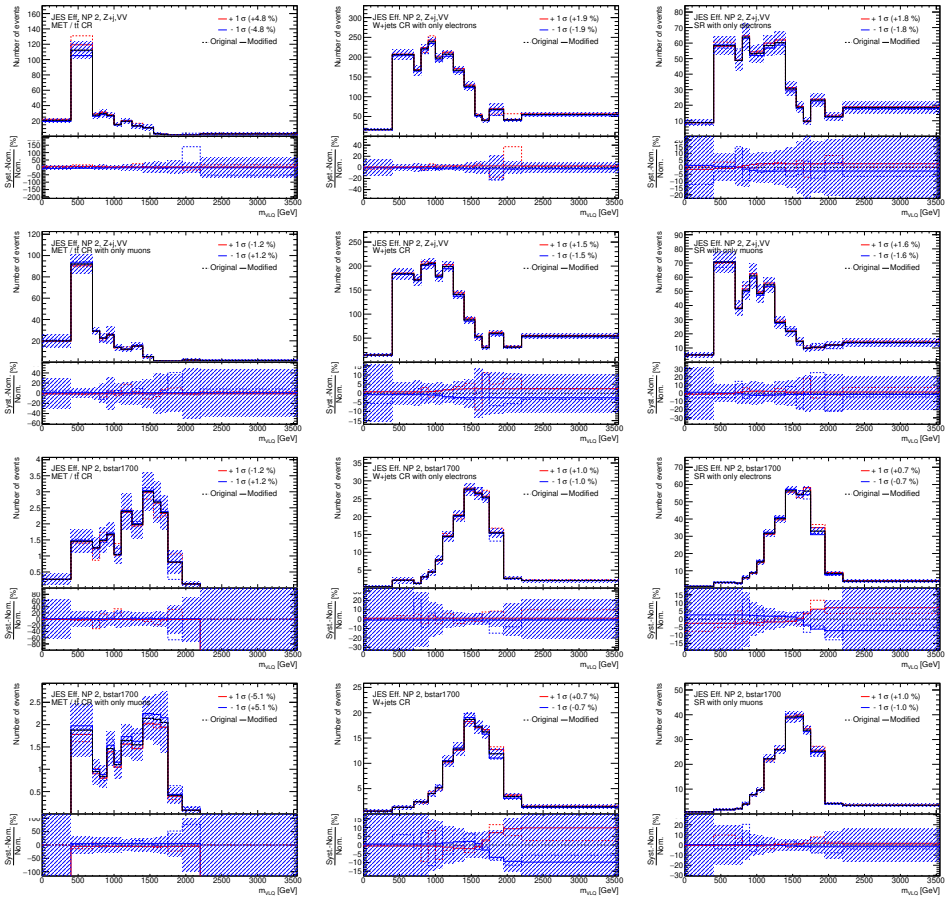

Figure B.12: Nuisance paramter 2 of jet energy scale (JES) systematic. Even though unexpected, this systematic is sligthly bigger than the NP1 of the JES systematic. But the smoothed up and down systematic is actually smooth and looks compatible with the unsmoothed systematic.

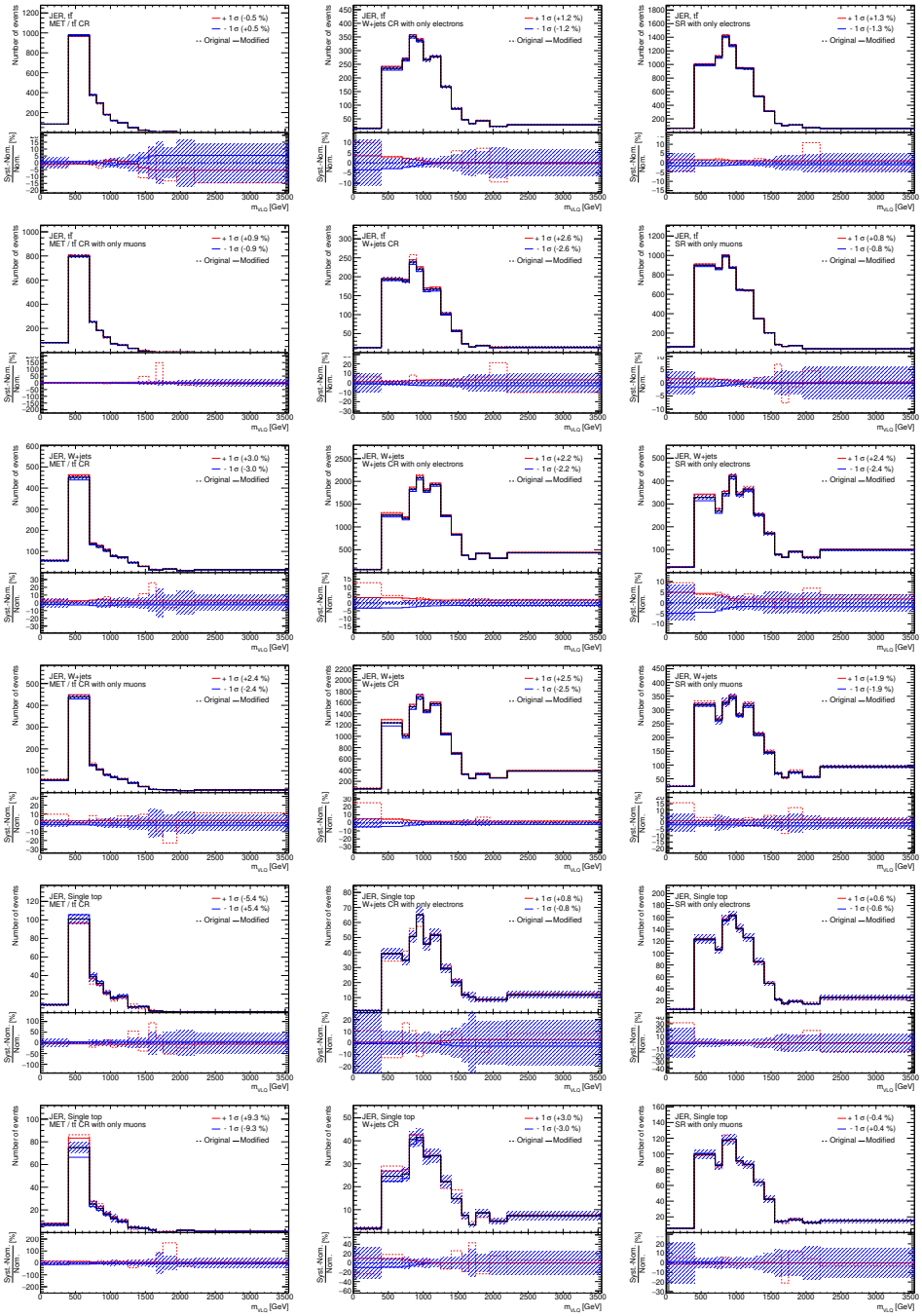
JER, tt
MET / tt CR
+ 1 σ (-0.5 %)
- 1 σ (+0.5 %)
Original
Modified
JER, tt
W+jets CR with only electrons
+ 1 σ (+1.2 %)
- 1 σ (-1.2 %)
JER, tt
SR with only electrons
+ 1 σ (+1.3 %)
- 1 σ (-1.3 %)
JER, tt
MET / tt CR with only muons
+ 1 σ (+0.9 %)
- 1 σ (-0.9 %)
JER, tt
W+jets CR
+ 1 σ (+2.6 %)
- 1 σ (-2.6 %)
JER, tt
SR with only muons
+ 1 σ (+0.8 %)
- 1 σ (-0.8 %)
JER, W+jets
MET / tt CR
+ 1 σ (+3.0 %)
- 1 σ (-3.0 %)
JER, W+jets
W+jets CR with only electrons
+ 1 σ (+2.2 %)
- 1 σ (-2.2 %)
JER, W+jets
SR with only electrons
+ 1 σ (+2.4 %)
- 1 σ (-2.4 %)
JER, W+jets
MET / tt CR with only muons
+ 1 σ (+2.4 %)
- 1 σ (-2.4 %)
JER, W+jets
W+jets CR
+ 1 σ (+2.5 %)
- 1 σ (-2.5 %)
JER, W+jets
SR with only muons
+ 1 σ (+1.9 %)
- 1 σ (-1.9 %)
JER, Single top
MET / tt CR
+ 1 σ (-5.4 %)
- 1 σ (+5.4 %)
JER, Single top
W+jets CR with only electrons
+ 1 σ (+0.8 %)
- 1 σ (-0.8 %)
JER, Single top
SR with only electrons
+ 1 σ (+0.6 %)
- 1 σ (-0.6 %)
JER, Single top
MET / tt CR with only muons
+ 1 σ (+9.3 %)
- 1 σ (-9.3 %)
JER, Single top
W+jets CR
+ 1 σ (+3.0 %)
- 1 σ (-3.0 %)
JER, Single top
SR with only muons
+ 1 σ (-0.4 %)
- 1 σ (+0.4 %)
Number of events
Syst.-Nom. / Nom. [%]
$m_{\ell\ell j j}$ [GeV]

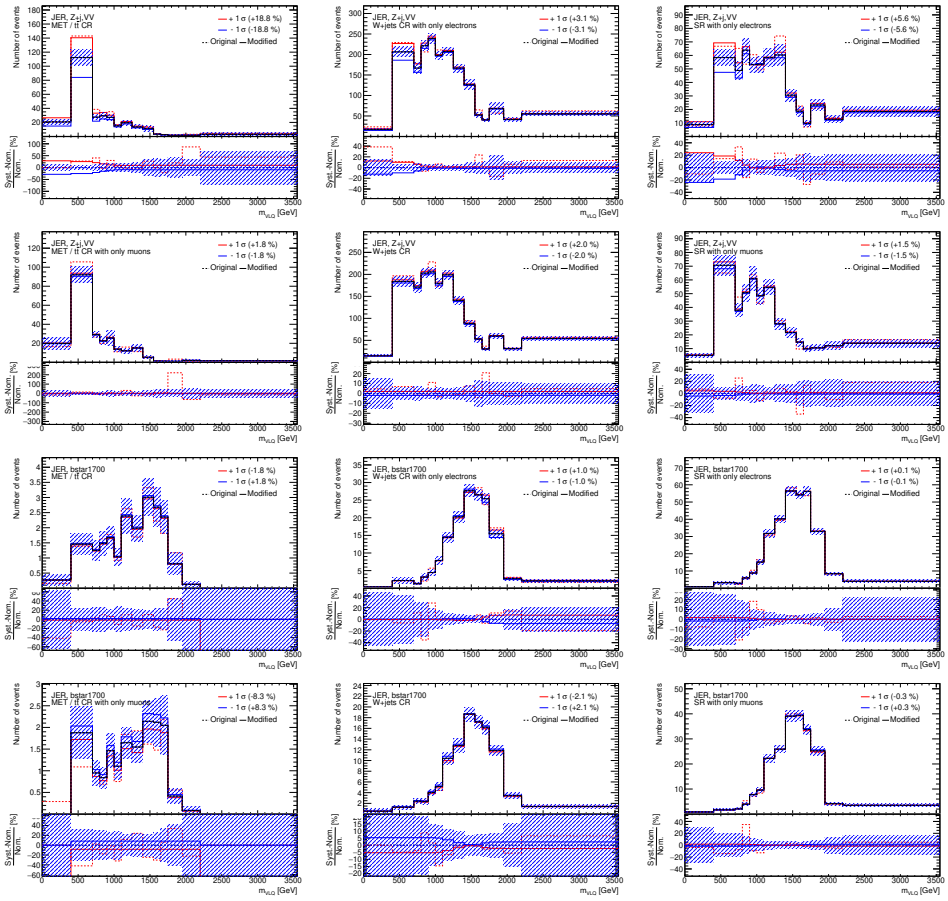

Figure B.13: Jet energy resolution systematic. This systematic is known to be pulled in several other analyses. The main effect of this systematic is in the low mass bins, which is understandable as the shape in these bins is affected by the reclustered jet p_T cut and thus small movements in jet energy might move events in and out of the selection. The smoothed up and down systematic is actually smooth and looks compatible with the unsmoothed systematic in this analysis as well.

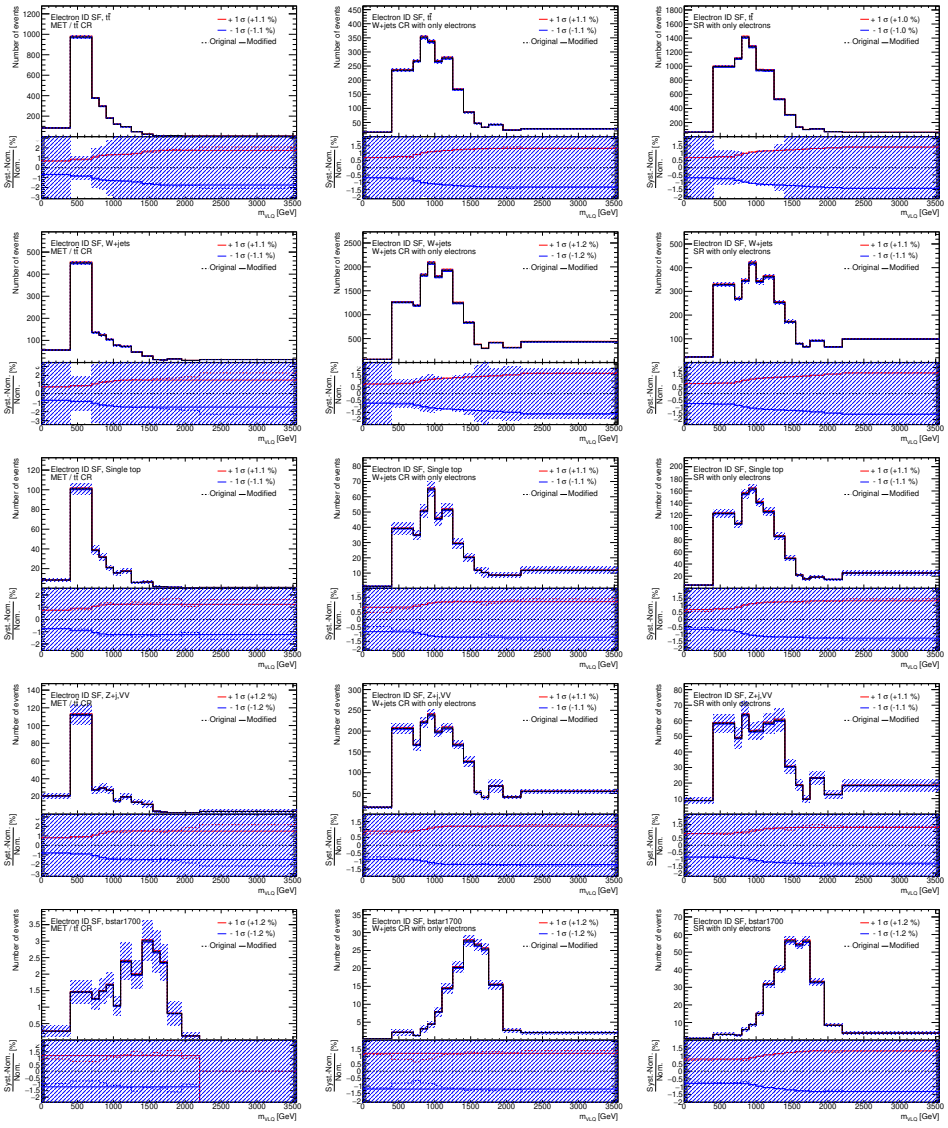

Figure B.14: Electron scalefactor on the identification systematic. The smoothed up and down systematic is actually smooth and looks perfectly compatible with the unsmoothed systematic.

Selbstständigkeitserklärung

Hiermit erkläre ich, die Dissertation selbstständig und nur unter Verwendung der angegebenen Hilfen und Hilfsmittel angefertigt zu haben. Ich habe mich nicht anderwärts um einen Doktorgrad in dem Promotionsfach beworben und besitze keinen entsprechenden Doktorgrad. Die Promotionsordnung der Mathematisch-Naturwissenschaftlichen Fakultät, veröffentlicht im Amtlichen Mitteilungsblatt der Humboldt-Universität zu Berlin Nr. 42 am 11. Juli 2018, habe ich zur Kenntnis genommen.

Berlin, den 30. September 2019

Dennis Sperlich